Metallogeny of a Pan-African oceanic arc: VHMS and gold deposits in the Ariab-Arbaat belt, Haya terrane, Red Sea Hills (Sudan)

M. Abu-Fatima, C. Marignac, Michel Cathelineau, M.-C. Boiron

Metallogeny of a Pan-African oceanic arc: VHMS and gold deposits in the Ariab-Arbaat belt, Haya terrane, Red Sea Hills (Sudan).

Abu-Fatima M. [1, 2], Marignac C. [1], Cathelineau M. [1], Boiron M.C.[1]

[1]Université de Lorraine, CNRS, CREGU, 54000, Nancy, France

michel.cathelineau@univ-lorraine.fr

marie-christine.boiron@univ-lorraine.fr

christian.marignac@univ-lorraine.fr

[2] Geological Research Authority of Sudan, The Republic of Sudan Ministry of Minerals

gras@sudanmail.net

Abstract

In the Neoproterozoic Arabo-Nubian Shield, the Ariab gold deposits in the Red Sea Hills (Sudan) are associated with volcanogenic massive sulphide (VMS) deposits, formed in the context of a Tonian ensimatic arc of the Haiya terrane. The mined gold is in gossans, re-concentrating primary gold. All the primary gold occurrences of the Ariab belt, whatever their style (VHMS-, quartz lode- or shear-zone-hosted), appear to have been syn-to late-kinematic, i.e., formed in the context of the final Pan-African collision leading to the Arabian-Nubian Shield (D3 event). Gold concentration occurs as native gold or electrum deposited in late (syn-to post-metamorphic) tectonic features, usually in sets of (micro)cracks, mostly within earlier pyrite or arsenopyrite. It is associated with either galena or bismuth tellurides. Gold deposition

occurred in relation with an intense fluid circulation of metamorphic CO_2-H_2O rich fluids which underwent significant strong decompression from lithostatic to hydrostatic pressures. Decompression, together with temperature decrease and dilution, are probably at the origin of gold deposition, although no clear evidence of unmixing of the volatile was observed.

The late-D3 gold event in the Ariab belt has all the makings of an orogenic gold system, notably similar to the Late Carboniferous gold event in the West European Variscan belt. Thus, it is possible to propose that, at the end of the collision events, fluids released from the newly formed terrane root were channelled towards the upper crust through the major D3 shear zones (the Oko shear zone for the Ariab belt). The fluids outpouring from these major drains were then conveyed through fault plays and damaged zones, up to specific chemical traps like massive sulphide ore bodies or quartz veins systems. Thus, the Ariab gold district could be classified as a representative of the shear-zone related orogenic gold deposits.

Keywords: VMS, ANS, gold, gossan, aqueous-carbonic fluids

1 INTRODUCTION

The Arabian-Nubian Shield (ANS), which is the largest tract of juvenile continental crust of Neoproterozoic age (Patchett and Chase 2002), is known for its gold endowment since the Pharaonic times (5,500 yr before present): the Egyptian part of the shield hosts more than 250 gold production sites (Fig. 1), and extensive gold production exists in the Sudanese part (with, in particular, the Hassai gold mine), Sudan being the second-ranking gold producer in Africa (Johnson et al. 2017, Tamer et al. 2018). The shield (and particularly the Arabian segment) is currently considered favourable for further gold exploration. Gold in the ANS is mainly present as (i) “stratabound”, in tight association with massive sulphide deposits in the Neoproterozoic

arc (Bakheit and Matheis 1993; Abu Fatima 2006; Barrie et al. 2016; Johnson et al. 2017; Volesky et al. 2017), Hassai, Jb Sayid and Bisha being the main occurrences (Fig. 1), and (ii) vein-type "orogenic" gold, closely related to the shear zones, and in particular, to the Najd system (Zoheir et al. 2019a), with notably the large Sukari and Madd adh Dhabab world-class deposits (Fig. 1). A few occurrences associated with BIF in arcs have long been considered synsedimentary (e.g. Botros 2004). Recently, however, Zoheir and Akawy (2010) have demonstrated that they belong to the family of "orogenic" gold deposits (Zoheir and Akawy 2010). A large gold-porphyry deposit (Jb Ohier, Fig. 1) has recently been described (Bierlein et al. 2016). Other occurrences were claimed to be also of the porphyry type (e.g., Sasmaz 2020), but are likely to be variant of the orogenic class of deposits.

The ANS is also the host for various rare metal deposits, including U, Nb-Ta, Sn and W (Lehmann et al. 2017), most of them in relation with the highly fractionated post-tectonic granites (Sami et al. 2017a,b, 2020). Thus, about 17 known Neoproterozoic (620-530 Ma) rare-metal granitic bodies occur in the Sinai, Eastern Desert-Medyan and Hijaz terranes, including the world-class Ta deposit of Abu Dabbab and Ghurayyah. Besides, a few pegmatites are known, with the world-class Ta-pegmatite at Kenticha in Ethiopia (Küster et al. 2009). Very locally, emerald was formed in the Negrus shear zone separating the Central and Southern Eastern Desert terranes, in series including leucogranites, biotite schists, and serpentinites (Abdalla and Mohamed 1999).

The ANS is equally the host for other raw materials, although as a minor component. There are podiform chromitite occurrences in several of the ophiolitic sutures (Bonavia et al. 1993; Ali et al. 2020), and Algoma-type BIF (possibly related with "snowball earth" episodes: Stern et al. 2006) are present in some arc terranes (Abd El-Rhaman et al. 2012; Khalil and El-Shazly 2012; El-Shazly and Khalil 2014).

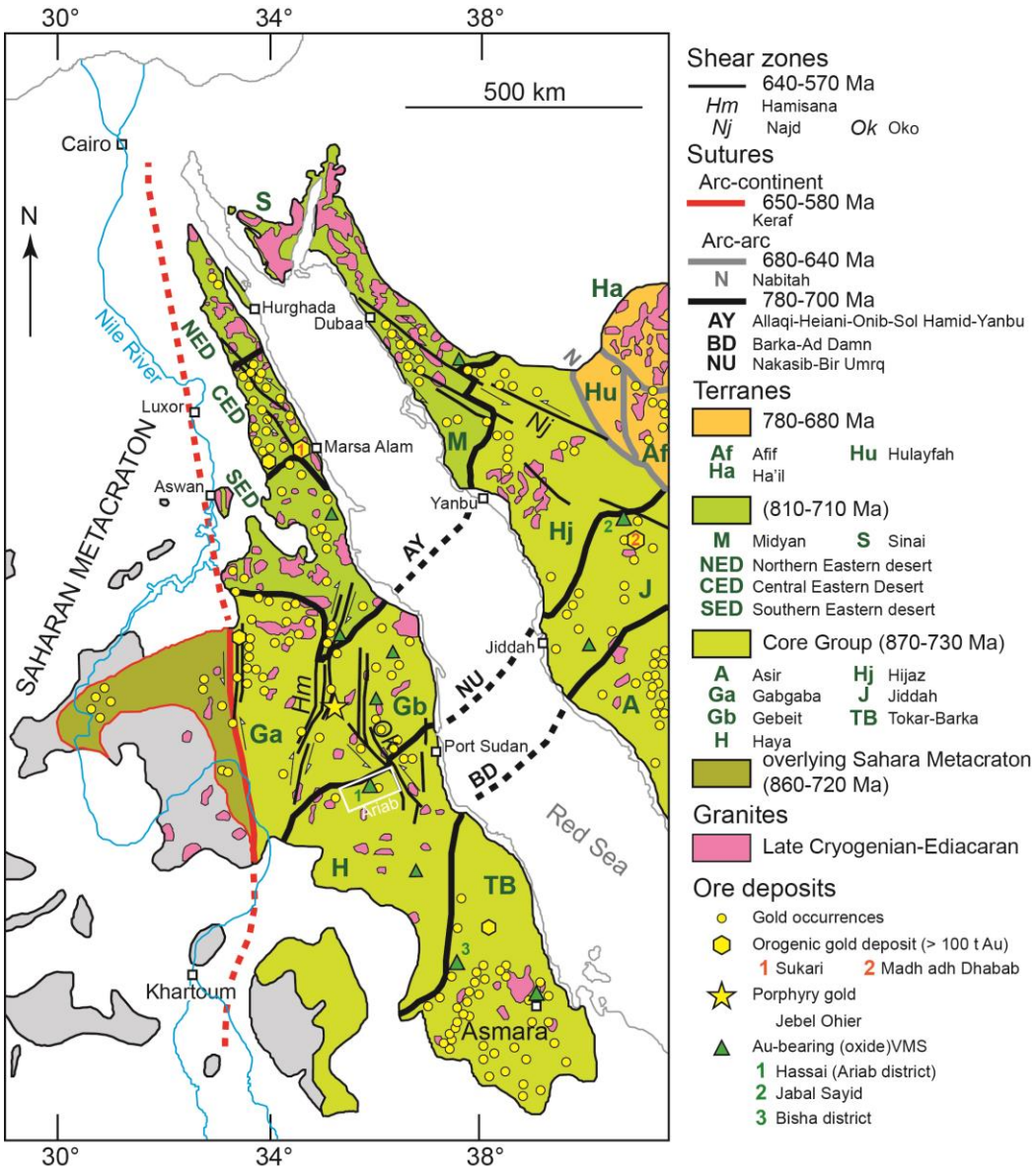

Figure 1. Schematic tectonic map of the Arabian-Nubian Shield, with the location of the Ariab belt (redrawn and adapted from Johnson et al., 2011, with complementary data from Barrie et al. 2016, Bierlein et al., 2016), and Zoheir et al., 2019)

The Hassai gold mine in the SW part of the central Red Sea Hills province, 250 km west of Port Sudan (Fig. 1), is the only mined deposit in Sudan. It was discovered as the result of an extensive exploration program in the Red Sea Hills, conducted in the '80s by a French-Sudanese

cooperation team, involving the French BRGM (Bureau de Recherches Géologiques et Minières) and the Sudanese GRAS (Geological Research Authority of Sudan).

A total of about 20 gold and base metal deposits were finally discovered in the low-grade metamorphic Ariab-Arbaat belt of the Haya terrane (Fig. 1). The Hassai mine was operated since 1993 by the Ariab Mining Company, a GRAS-COMINOR (Areva) joint venture until 2015. After this date, the Sudanese Government has wholly controlled it. The main gold mineralization at Hassai, hosted by a silica-barite rock in the close vicinity of a massive sulphide body, was at first hand interpreted as a lateral hydrothermal exhalative of a VHMS deposit (Cottard et al. 1986a). Recoché (1989) demonstrated the existence of supergene enrichment in the oxidised part of the upper part of the massive sulphide, and it is indeed these "gossan" deposits that are presently mined. The mine, which comprises three deposits (Hassai S, Hadal Adawatib E, and Hadayamet), has produced ~ 85 t of gold until now.

In their review of the "Au-rich VMS" class of deposits, Dubé et al. (2007) erroneously ranked Hassai as one of the giant representatives, quoting a 76 t gold content at a mean grade of 9.74 $g.t^{-1}$. They had indeed confused the Hassai reserves with the total bulk reserves of the gossan ores in the whole Ariab camp. Nevertheless, it has since been recognized that the primary sulphide deposits below the gossans are effectively members of the "Au-rich class", with estimated ~ 59 t of gold for Hassai S and ~ 75 t for Hadal Awatib E, at far lower Au contents, however (1.47 and 1.1 $g.t^{-1}$ respectively).

There is no consensus on the origin of gold concentration in Au-rich VMS deposits. Gold is thought to have been introduced in the massive sulphides either early (syngenetically) with more or less pronounced tectonic-metamorphic remobilisation (e.g., Dubé et al. 2007, and references therein) or later, as the result of fluid circulation in brittle fractures in association with retrograde alterations (e.g., Taube 1986, Marquis et al. 1990a, Yeats and Groves 1998, Gibson and Galley 2007). Besides, Dubé et al. (2007) list a series of characters specific to Au-

rich VMS deposits, including the nature of the felsic host, the existence or not of syn-volcanic intrusives, the presence of advanced argillic alterations. On this basis, he suggested that this class of deposits could be a submarine equivalent of the high sulphidation epithermal deposits on land. The true VMS nature of some deposits included in the Au-rich VMS class by Dubé et al. (2007) could, however, be debated (e.g., Boliden: Bergmann-Weihed et al. 1996; Mount Morgan: Arnold and Sillitoe 1989).

On the other hand, fossil polymetallic VHMS deposits appear as relatively gold-poor in average when compared with their modern equivalents (Glasby et al., 2000, Barrie and Hannington, 1999, Mercier-Langevin et al., 2010). Such low gold grades may indicate gold exportation out from the re-crystallising massive sulphides during the metamorphic events. The observed gold concentrations frequently occur in late brittle structures within the same VHMS bodies and notably in their quartz-rich feeder stockworks prone to late faulting and fluid circulation. They could, therefore, be considered as a particular occurrence of the orogenic class of gold deposits. i.e., as the result of gold re-introduction by late orogenic fluids and trapping on the pre-existing sulphides. Indeed, Marignac et al. (2003) reached this conclusion in their study of the gold setting in the Carboniferous Iberian Pyrite Belt.

The present study of the Ariab field allows testing this hypothesis further. The extensive exploration work done at the beginning of the 2000s in the Ariab field to evaluate the gold potential of the unaltered roots of the deposits known by their gossans provided data that allowed a full characterisation of this significant goldfield. Through the unravelling of the tectonic setting of the massive sulphides, their relationships with felsic volcanic activity, and the timing of gold introduction, the present work addresses the gold metallogeny in this key area. We examined the possible roles of exhalative hydrothermal, granite-related, and orogenic processes in the generation of primary gold concentrations before the supergene events in the Red Sea Hills. Besides, the Ariab Au-field was compared with similar fields in the ANS.

2. GEOLOGICAL SETTING

2.1. The Arabian-Nubian Shield

Around 25 Ma ago, the Red Sea opening separated the present-day Nubian and Arabian parts of an initially continuous Neoproterozoic juvenile crust belt, the Arabo-Nubian Shield (ANS). The ANS is the northern part an East African Orogen, extending southward to Madagascar. It formed in relation with the closing of a Tonian Mozambique ocean and the formation of the Gondwana supercontinent by the "ultimate collision of Neoproterozoic India with the Congo-Tanzania-Bangweulu Block (in the south) and the Sahara (meta)craton (in the north)" (Johnson et al., 2011).

Syntheses by Johnson et al. (2011) and Fritz et al. (2013) provided a robust framework for the ANS structure and evolution, which has not been fundamentally altered since, although clarified in several studies. The following presentation is mainly based on these authors.

According to Johnson et al. (2011), and Fritz et al. (2013), the ANS architecture (Fig. 1) may be broadly described as the result of two successive major sequences of events. First, an accretion stage, consisting in a series of arc/arc collisions, and ending with the amalgamation of a proto-Arabian-Nubian Shield (p-ANS), encompassed the ca. 900-650/640 Ma interval (Tonian-Cryogenian). It was followed by arc/continent collisions related to the squeezing of the p-ANS between the Sahara (meta)craton and the Neoproterozoic India craton, during their final convergence (East African Orogeny of Fritz et al. 2013, EAO) between ca. 635 and ca. 550 Ma (Late Cryogenian-Ediacaran).

The accretion stage may be further divided. Its initiation is the formation of a Core Group of Tonian accreted terranes (Tabar-Barka-Arif, Haya-Jiddah, Gagbaba-Gebeit-Hijraz terranes, ca. 900-830 Ma) (Fig. 1), separated by ophiolitic sutures (Barka-Ad Damn, Nakasib-Biir Umq, Fig. 1) formed between 780 and 750 Ma. Then, occurred the Late Tonian-Early Cryogenian collision

of the Core Group with the northern ANS terranes (East Desert-Medyan terrane, ca. 750-715 Ma: Kosdroj et al., 2017, Hami et al. 2019; and Sinai terrane, ca. 820-740 Ma: Elisha et al., 2019) along with the 710-690 Ma (Eyal et al. 2019) Allaqi-Heiani-Onib-Sol Hamid-Yanbu suture (Fig. 1). The final amalgamation of the p-ANS resulted from the ca?. 650-640 Ma collision of the Afif terrane with the already assembled terranes. These events were associated with the first major metamorphic event (M1) in the ANS.

The possible presence of Kibaran (c. 1.4-1.0 Ga: Fernandez-Alonso et al. 2012) nuclei, principally in some arcs of the northern terranes (East Desert-Medyan, Sinai), is documented by direct evidence (the 1.12-0.95 Ga Wadi Sa'al volcano-sedimentary complex in the Sinai terrane: Ali-Bik et al. 2017) or suggested by the sporadic occurrence of older than c.0.9 Ga zircons as either xenocrysts or cores in the magmatic arc rocks (Ali et al. 2016 and references therein), or detrital zircons in arc siliciclastic sediments (Li et al. 2018). Yet, it remains that the p-ANS, and in particular, the Core Group, are characterised by the pervasive emplacement of ensimatic island arc (Ali et al. 2020) and synorogenic granitoids at c. 845-c.700 Ma (Robinson et al. 2015) explaining a mostly juvenile lead isotope signature (Johnson et al. 2011 and references therein).

The second (EAO) sequence was marked by the late accreting events in both western and eastern parts of the orogen. To the west, the collision of the p-ANS with the Saharan (meta)-craton resulted in the Keraf and Atmar-Dalgado sutures (Fig. 1) at c. 620-600 Ma (Megerssa et al., 2020). To the east, the accretion of the Al Amar arc (690 Ma ophiolite) along the Nabitah suture (Fig. 1) occurred at 620-610 Ma (El-Bialy et al. 2020). Resulting from India's arrival, it was coeval with significant metamorphism (M2) and deformation in the Sinai terrane (Elisha et al. 2017, 2019). These events were accompanied/followed by the development of large intra-continental shear zones dilacerating the p-ANS, with NW-SE ductile sinistral shear zones and their conjugate N-S and NNE-SSW dextral structures (Fig. 1). The most important of these

structures is the 2000 km-long crustal-scale NW-SE Najd system (Abdelsalam and Stern 1996), with its numerous second and third-order splays in the East Desert terranes (Fig. 1). In NE Sudan, the N140°E Oko sinistral shear zone (Abdelsalam 1984) is part of the Najd system. In contrast, the dextral N-S Hamisana shear zone (Saeed et al. 2020) represents the conjugate set. The activity of these shear zones extended from c. 630 to c. 580 Ma (Hassan et al. 2016 a, b) or even 560-550 Ma (Hamisana, Oko, Keraf: Johnson et al. 2011). In the northern terranes, it was associated with the exhumation of high-grade rocks of the arc roots, forming metamorphic core complexes (Meyer et al. 2014). Unconformable "molassic" basins developed at the same time (starting at c. 630 Ma, Bezenjani et al. 2014), as well as volcanism (Dokhan ignimbrite 610-590 Ma: Hamimi et al. 2019). Several magmatic pulses yield at that time to the syn-to late- and post-kinematic granite intrusions (Lundmark et al. 2012). The basins history is interrupted at c. 610 Ma, with low-grade metamorphism (M2) and deformation of the earliest sediments. The development of an unconformity below the upper series (Bezenjani et al. 2014) during the "first post-collisional cycle" defined by Eyal et al. (2019), recorded the final collision with the Saharan metacraton. The succession of two types of granites is observed, with some overlap. First came high-K calc-alkaline granites (635-590 Ma), followed by hypersolvus alkali feldspar granites and peralkaline granites (608-580 Ma) (Be'eri-Shlevin et al. 2009). The granite plutons are by far more frequent in the northern terranes (Fig. 1). Minor, but systematic mafic magmatism (small intrusions and dykes) encompassed the late granite activity (Khalil et al. 2015). It continued until 545 Ma (Abbo et al. 2020), documenting extension in the ANS from 590 to 545 Ma (Fritz et al. 2013).

By the end of the Ediacaran, the entire ANS had been subjected to erosion and peneplanation, forming a low-relief surface on which the Lower Cambrian sandstones were deposited (Avigad et al. 2005).

2.2 The Ariab-Arbaat belt in the Haya terrane

The Ariab belt is located at the Haya terrane boundary with the Nakasib-Biir Umq ophiolitic complex, separated from the complex by a major NW-verging thrust (Schandelmeyer et al. 1994) (Fig. 2). Therefore, the Ariab belt history is intimately linked to the Core Group's formation and its evolution.

The time of formation of the northern Haya terrane, of which the Ariab belt is but the northernmost unit, is bracketed between 887 ± 20 and 854 ± 9 Ma (Reischman et al. 1992). The history of the deformation of the Ariab arc related to the Haya/Gabgaba-Gebeit collision can be broken down into two events, D1 and D2 (Fig. 3). From D1 to D2, the shortening direction rotated from NE-SW to E-W, and the deformation evolved from compressive to transpressive, with dextral reactivation of the suture. According to Wipfler (1996), D1 thrusts and tight to isoclinal N60°-70°E F1 folds, coeval with the development of the main regional S1 schistosity, generally close to S0 in the Ariab belt, were steepened and refolded during D2. Folds F2 are of limited amplitude, a few metres to some ten metres, with axial plane S2 schistosity and strike N0°- 30°E upright. D1 and D2 occurred under the same low-grade (greenschist facies) metamorphic conditions.

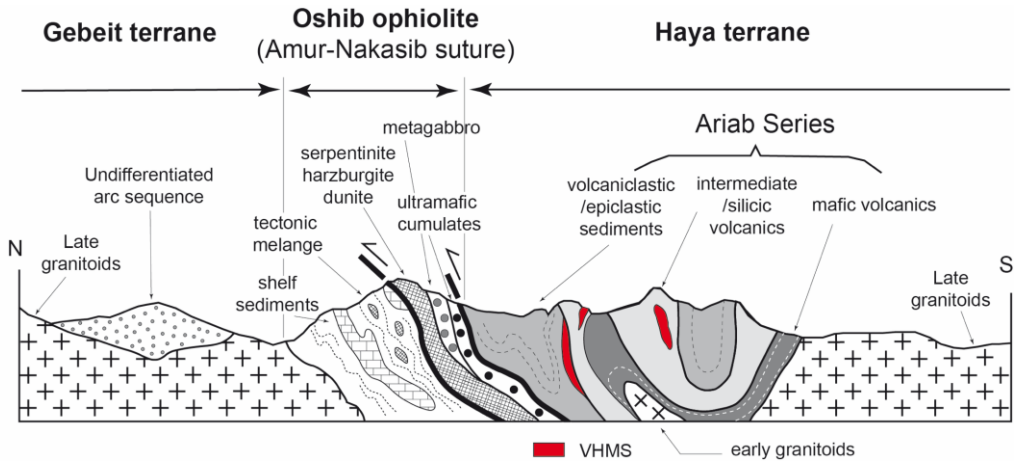

Figure 2. Diagrammatic cross-section through the Gebeit-Oshib-Haya terranes, showing the Amur-Nakasib ophiolitic suture and the Ariab Series (redrawn from Abu Fatima, 2006, after Abdel Rahman, 1993 and Wipfler, 1996).

After uplift and erosion, magmatic activity resumed in the amalgamated terranes, with the deposition in the Ariab area of the Arbaat volcano-sedimentary rocks, and the intrusion of the G2 granite suite. The ~790 Ma old Arbaat Group consists of tholeiitic, rift-related mafic volcanic rocks with subordinate felsic volcanic rocks and siliciclastic sedimentary rocks (Abdelsalam 2010). The intrusion age of the G2 suite is poorly constrained, between 750-740 Ma and 710 Ma (Stern and Abdelsalam 1998). Final accretion of the proto-ANS onto the Saharan (meta)craton was associated with a renewal of tectonic activity in the Haya terrane (D3 event, Fig. 3). The D3 event was mainly transpressive, with an E-W shortening direction, at the origin of the F3 folds and S3 schistosity in the Ariab area. Small scale thrusts are also observable (see § III-5). D3 was coeval with the development of conjugated NW-SE to NNW-SSE sinistral and NNE-SSW dextral strike-slip faults under ductile, and then dominantly brittle, conditions at the shield scale (Fig. 1). Sinistral kinematics on the Oko shear zone occurred between ca. 640 and ca. 560 Ma (Abdelsalam 1994).

Cycle	Global event	Tectono-metamorphic event	Objects	Age
Pan-African	Juvenile arc in oceanic environment	Hydrothermal sub-sea floor metamorphism	Basalt to rhyolite submarine to subaerian volcanism (Ariab Series) and coeval plutonism (G1 suite) VHMS and barite deposits	ca. 900 Ma G1 granitoids at 888±3.7 Ma
	Arc accretion and thickening	D1 Obduction and oblique arc collision Low-grade metamorphism	Regional S1 schistosity Recumbent to upright regional N60-70°E F1 folds Transpressive SZ	ca. 770 Ma
	unconformity	D2 Late shortening Low-grade metamorphism	Upright local N0-30°E F2 folds Regional S2 schistosity Dextral reactivation of D1 SZ	
	Evolved mature arc	Contact metamorphism	Awat-Aseriba calk-alkaline series Coeval to late plutonism (G2 suite)	730-720 Ma 720-680 Ma
	Final collision	D3 Transpression	Conjugated sinistral NW-SE to NNW-ESE and dextral NNE-SSW ductile to brittle SZ Faint local S3 schistosity	620-580 Ma
Gondwana break-up			Anorogenic plutonism	150 ± 4 Ma
Red Sea rift	Red Sea early opening	D4 Fracturation	NE-SW faults	Miocene

Fig. 3. Main events affecting the Haya terrane (see text for explanation and references).

After that, the Haya Terrane remained stable, as the whole Nubian Shield in the Red Sea Hills. The only recorded anorogenic magmatism associated with Gondwana break-up (Höhndorf et al. 1995), is the 150±4 Ma Jabal Tame complex in the Haya terrane (Kuster et al. 1993). The region then experienced NE-SW faulting related to the Red Sea's early opening (D4 event: Fig. 3).

2.3 Lithostratigraphy of the Ariab belt

2.3.1. The Ariab series

The Ariab series make the lowermost suite of the northern Haya terrane. The BRGM teams have subdivided the series into five litho-type units, labelled A to E, based on their main components, as a whole succeeding one to the other from bottom to top when seen in their pre-tectonic setting (Cottard et al., 1986b). However, there are complications, and it was necessary to introduce further subdivisions within the B and C units to reconstruct a "true" lithostratigraphic pile (Fig. 4).

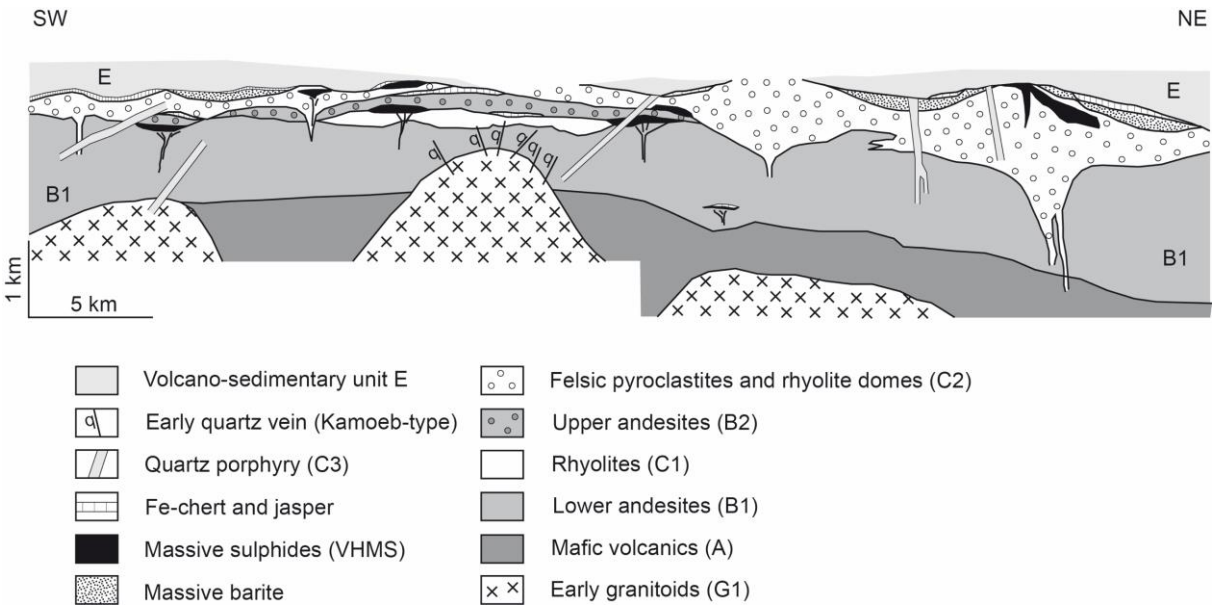

Figure 4. Reconstruction of the Ariab series lithologic pile before the D1 deformation event (redrawn from Abu Fatima, 2006).

Unit A: Tholeiitic series: Basalt flows with minor andesitic basalt and microgabbro (the latter as sills and dykes) constitute a series of more than 1000 m thickness. Locally well-preserved pillow and vesicular textures testify for a submarine emplacement.

Unit B: Intermediate volcanic unit B at the outcrop is a thick volcanic unit with a thickness of about 1000 m, subdivided into two sub-units (B1 and B2, the latter varying from 10 to 200 m

in thickness) due to the local intercalation of a thin lenticular felsic sub-unit (C1, see below and Fig. 4). The B2 sub-unit is the D unit of Cottard et al. (1986b). Both B1 and B2 sub-units are mainly basaltic andesite to andesite in composition (Fig. 5). Most of the rocks are hyaloclastites, judging from the abundance of small vesicular angular fragments set in the chlorite schists that constitute the B unit's main rock-type. Yet, locally preserved pillow- and vesicular-lavas are evidence for subaquatic flows, and some massive fine-grained homogeneous facies may represent former lava flows and sills.

	Unit A		Unit B1			Unit B2		Unit C1		Unit C2			Unit C3		G1 Suite						G2 Suite			
	NTALGST-173	*Lat-02*	*TAL04*	KAM-03	DIM-01	*GANGT-17*	*HAE-CD08*	*ODE-01*	TIDTUAND-11	ADS03	A3	*TAL-46*	*ADAM01*	*GAN01*	RUK4-02	*ODE-03*	SWKAM137	BAD-25	BIRAJM8	EKITL-2	*UMHASH-7*	*TOMB-01*	HADND77-99	KAMLG-131	*ADAMG-12*	*LGRAN*
SiO_2	51.69	47.87	44.71	54.74	66.51	57.63	56.32	55.58	68.18	77.51	73.14	74.99	75.82	88.18	71.69	65.88	50.82	59.21	71.65	76.46	75.79	72.32	49.57	75.34	59.37	67.37
TiO_2	0.76	0.52	0.33	0.17	0.21	1.39	0.37	0.40	0.34	0.12	0.30	0.36	0.16	0.07	0.20	0.65	0.16	0.48	0.16	0.08	0.12	0.19	0.94	0.16	0.52	0.53
Al_2O_3	13.67	14.84	12.63	14.00	11.48	11.78	15.25	15.47	11.05	9.32	10.80	11.00	10.73	6.98	11.83	12.38	14.11	16.12	13.10	12.02	12.00	11.67	13.47	11.40	16.25	15.65
Fe_2O_3	11.29	9.72	13.98	11.01	6.29	18.20	9.54	10.78	6.42	4.45	5.10	5.03	3.68	1.43	4.97	9.27	9.65	6.87	4.23	1.88	3.51	3.19	12.52	3.33	6.86	4.29
MnO	0.17	0.11	0.42	0.19	0.10	0.17	0.30	0.17	0.17	0.04	0.11	0.06	0.05	<DL	0.08	0.19	0.18	0.12	0.06	0.04	0.06	0.16	0.20	0.08	0.14	0.09
MgO	7.29	8.79	11.24	6.43	4.19	5.29	2.93	7.39	1.47	0.30	0.86	1.29	3.11	<DL	0.90	2.17	9.45	2.86	1.03	0.57	1.88	1.13	4.24	0.61	3.08	1.39
CaO	9.69	7.56	3.95	8.20	4.78	0.48	5.61	1.43	5.58	0.37	2.33	0.69	<DL	<DL	2.14	1.19	12.30	.88	3.35	0.82	0.75	3.97	7.65	2.74	6.52	3.12
Na_2O	3.60	2.57	<DL	2.69	5.20	<DL	3.60	4.71	0.77	4.37	3.25	5.06	0.31	0.34	4.02	5.54	0.82	3.29	4.13	4.54	3.69	2.76	3.27	3.49	3.10	4.60
K_2O	0.06	<DL	0.16	0.66	<DL	0.18	0.144	<DL	1.34	0.30	0.51	<DL	1.87	1.48	0.70	0.11	<DL	1.03	0.37	2.04	0.51	1.38	0.59	0.81	1.06	1.76
P_2O_5	0.08	0.07	0.05	0.05	0.07	0.31	0.11	0.08	0.13	<DL	0.10	0.09	<DL	<DL	0.06	0.12	0.5	0.12	0.06	0.04	<DL	0.05	0.19	0.07	0.12	0.23
LOI	2.05	8.84	11.21	2.23	1.98	5.36	4.65	4.27	4.92	3.49	3.51	1.53	3.46	1.54	2.36	1.98	3.20	2.45	1.37	1.30	1.69	2.82	7.66	1.50	2.05	0.75
Total	100.35	100.91	98.68	100.37	100.82	100.79	98.83	100.26	100.38	100.29	100.00	100.07	99.19	100.03	99.94	99.47	100.74	99.41	99.52	99.79	99.99	99.63	100.31	99.53	99.43	99.76
Ba	86	101	267	409	130	108	527	105	2539	263	179	850	13 560	1 042	220	98	92	348	234	1 132	269	415	371	396	410	579
Rb	0.7	<DL	2.0	13	<DL	1.6	2.5	<DL	25	5.1	9.3	0.6	21	24	11	1.8	0.5	18	4.3	28	6.4	23	11	18	14	41
Sr	121	68	29	123	130	12	146	43	145	45	87	32	136	44	45	28	84	537	191	43	67	94	151	116	437	348
Cu	25	<DL	155	89	23	30	858	255	37	217	27	29	27	42	272	384	76	70	11	13	5	8	114	125	50	5
Pb	1	2	12	6	7	5	8	3	20	70	9	16	9	339	7	4	5	8	5	8	4	12	7	4	6	7
Zn	62	47	367	98	50	124	1172	408	134	149	87	78	138	21	93	798	99	67	23	29	21	39	129	129	82	66
As	1.9	5.8	4.9	1.5	6.2	1.1	6.4	2.1	2.7	15	2.0	3.7	1.6	37	2.5	<DL	6.8	6.4	1.3	<DL	<DL	1.4	4.2	2.2	1.6	<DL
Cr	273	322	348	254	351	29	79	131	60	100	107	95	75	97	134	12	516	78	91	116	89	62	12	244	78	97
Ni	75	94	48	52	40	14	21	69	6	14	8	9	9	6	7	19	64	18	8	19	7	10	12	14	18	9
Co	40	40	42	46	22	36	41	33	6	6	4	6	5	0.4	8	18	55	18	9	4	5	5	41	137	18	7
V	231	232	229	270	132	197	183	262	14	19	21	21	8	24	43	134	190	169	44	15	17	25	383	16	150	39
Nb	0.43	0.33	0.34	0.46	1.11	2.51	0.42	0.74	0.96	0.95	0.97	1.10	1.22	0.43	1.20	1.01	0.19	1.09	1.71	3.53	2.59	1.73	0.56	1.75	1.09	2.92
Ta	0.10	0.03	0.02	0.03	0.08	0.21	0.03	0.06	0.07	0.07	0.06	0.08	0.08	0.02	0.08	0.08	0.07	0.09	0.12	0.28	0.17	0.14	0.11	0.76	0.09	0.16
Zr	33	22	9	10	42	198	14	30	34	47	32	45	64	5	36	48	8	68	36	129	100	62	24	60	59	188
Hf	1.0	1.9	0.2	0.3	1.3	5.6	0.5	0.9	1.1	1.5	1.0	1.4	2.0	0.2	1.1	1.6	0.2	2.3	1.2	4.7	3.3	1.9	0.8	1.5	2.0	5.0
Th	0.13	0.09	0.16	0.29	0.93	0.37	0.25	0.57	0.76	0.86	0.80	0.73	1.11	0.09	0.96	0.69	0.14	4.07	1.02	3.63	1.94	1.54	0.33	1.65	1.40	4.60
U	0.09	0.04	0.22	0.33	0.31	0.23	0.22	0.16	0.28	0.67	0.29	0.32	0.53	0.27	0.37	0.24	0.07	1.65	0.74	1.20	0.67	0.63	4.01	0.54	0.71	2.65
Y	20	17	6	7	17	73	13	16	21	24	19	18	18	2	18	27	5	15	16	76	52	19	15	25	19	12
La	1.43	0.11	1.62	1.92	4.89	3.57	1.77	3.03	4.07	3.62	3.85	3.21	3.64	0.32	4.34	4.63	0.72	11.8	4.59	14.3	11.2	6.92	2.61	6.81	8.86	25.0
Ce	4.30	2.79	2.91	4.38	10.8	11.0	4.04	6.02	9.05	7.97	8.73	7.50	11.1	0.74	9.38	9.79	1.78	25.2	9.68	32.2	25.6	14.9	6.36	15.0	20.3	51.2
Pr	0.74	0.52	0.39	0.54	1.40	2.27	0.62	0.93	1.28	1.19	1.22	1.11	1.26	0.12	1.28	1.49	0.24	3.22	1.26	4.34	3.60	1.98	0.99	1.95	2.85	6.02
Nd	4.22	3.00	1.87	2.36	6.20	12.9	3.23	4.33	6.04	6.11	5.76	5.53	6.01	0.58	5.85	7.50	1.19	13.6	5.49	20.0	17.1	8.47	5.21	8.72	12.6	22.4
Sm	1.72	1.17	0.59	0.69	1.76	5.24	1.16	1.33	1.92	2.28	1.77	1.78	1.87	0.22	1.78	2.50	0.40	2.92	1.58	6.24	5.26	2.30	1.68	2.53	3.01	4.08
Eu	0.72	1.79	0.27	0.24	0.46	1.04	0.45	0.48	0.69	0.63	0.53	0.53	0.22	0.05	0.51	0.83	0.16	0.78	0.47	0.35	1.35	0.62	0.56	0.56	0.81	1.10
Gd	2.62	14.0	0.81	0.84	2.09	7.89	1.60	1.75	2.48	3.12	2.26	2.30	2.22	0.25	2.17	3.37	0.55	2.58	1.92	8.18	6.53	2.56	2.28	3.21	2.96	3.17
Tb	0.49	0.37	0.14	0.16	0.37	1.58	0.28	0.32	0.45	0.59	0.41	0.42	0.41	0.04	0.39	0.60	0.10	0.41	0.34	1.56	1.17	0.44	0.38	0.58	0.49	0.43
Dy	3.36	209	0.95	1.12	2.54	11.0	1.96	2.23	3.22	4.03	2.88	2.85	2.95	0.33	2.78	4.15	0.73	2.51	2.43	11.1	7.94	2.99	2.54	3.91	3.07	2.35
Ho	0.73	0.72	0.21	0.26	0.57	2.45	0.43	0.50	0.72	0.86	0.65	0.63	0.68	0.08	0.62	0.92	0.16	0.53	0.54	2.51	1.76	0.65	0.55	0.88	0.65	0.43
Er	2.20	2.64	0.63	0.82	1.73	7.48	1.31	1.49	2.23	2.56	2.02	1.92	2.19	0.25	1.93	2.78	0.51	1.56	1.71	8.02	5.37	2.01	1.60	2.76	1.94	1.16
Tm	0.34	0.28	0.10	0.13	0.28	1.14	0.20	0.23	0.36	0.39	0.33	0.30	0.37	0.04	0.31	0.44	0.08	0.24	0.28	1.34	0.84	0.32	0.25	0.45	0.31	0.17
Yb	2.27	1.87	0.68	1.00	1.94	7.74	1.43	1.58	2.49	2.66	2.31	2.15	2.87	0.35	2.19	3.04	0.58	1.69	2.04	9.76	5.88	2.26	1.67	3.21	2.19	1.13
Lu	0.36	1.08	0.11	0.17	0.32	1.23	0.23	0.26	0.41	0.40	0.39	0.36	0.49	0.06	0.36	0.48	0.10	0.28	0.35	1.61	0.97	0.38	0.27	0.52	0.36	0.19
ΣREE	40.21	239.34	11.28	14.63	35.35	76.83	18.71	24.48	35.41	36.41	33.11	30.59	36.28	3.43	33.89	42.52	7.30	67.32	32.68	121.51	94.57	46.80	26.95	51.09	60.40	118.83

Table 1. Representative analyses of the main rocks types from the Ariab Series and G1 and G2 suites. Italics designate the altered samples.

Unit C: Felsic volcanic unit, rhyodacitic to rhyolitic in composition (Fig. 5), is subdivided into three sub-units:

- C1 sub-unit is intercalated within the B unit (see above and Fig. 4) and consists of small lava domes and flows.

- C2 sub-unit, the main host for the massive sulphide and barite deposits, consists of extrusive lavas and pyroclastics. The former exhibit homogeneous textures, with locally preserved flow structures or autoclastic breccias. The rhyolitic facies contain quartz and K-feldspar phenocrysts set in a fine-grained felsic matrix. Rhyodacitic facies are more porphyritic, with quartz, plagioclase and hornblende phenocrysts. The latter display well-defined primary bedding with alternating fine-grained (ashes? Pumice tuffs?) and coarse-grained (clastics) horizons, in which fragments are so much transformed through hydrothermal alteration, deformation, and metamorphism that their original features are usually obliterated.

Significant thickness variations (from a few metres up to several 100 m), correlated with petrographic changes, suggest that the C2 sub-unit (and C1 sub-unit) is made of irregularly distributed extrusive lava domes surrounded by pyroclastic aprons. Laterally, the C2 sub-unit extends at the B sub-unit expense from the SW to the NE, with the total disappearance of the B2 subunit (Fig. 4), suggesting some degree of interfingering between andesitic and more felsic magmatism in the Ariab-Arbaat belt.

- C3 sub-unit is a set of rhyodacite dykes that crosscut all the Ariab series facies, including C2 and the associated massive sulphide and barite deposits, to the notable exclusion of the E unit. The dykes are quartz-porphyries, with abundant quartz and feldspar phenocrysts set in a fine-grained matrix with quartz, feldspars, and biotite. These dykes may be coeval with the early granitoids (G1) (see below). Alternatively, the dykes could have been the feeders for the explosive volcanism at the origin of the E unit.

Unit E: Volcano-sedimentary unit E is a thick (several 1000 m) sequence of volcano-sedimentary rocks, with a regional trend from dominantly volcano-clastic in the SW to more silico-clastic in the NE. A thin and continuous layer of black siliceous metapelites with cherts and jaspers marks the unit's base and grade to layered tuffs, greywackes, and schists, interbedded with fine-to coarse-grained epiclastic horizons, intermediate to silicic in composition. The unit comprises greywackes and reworked ash-falls, alternating with marbles, quartzites, and minor C-rich cherts and breccia-conglomerates of volcanic derivation. Greywackes are usually medium- to coarse-grained, with lithoclasts of various origin and rhyolitic quartz and feldspars as components.

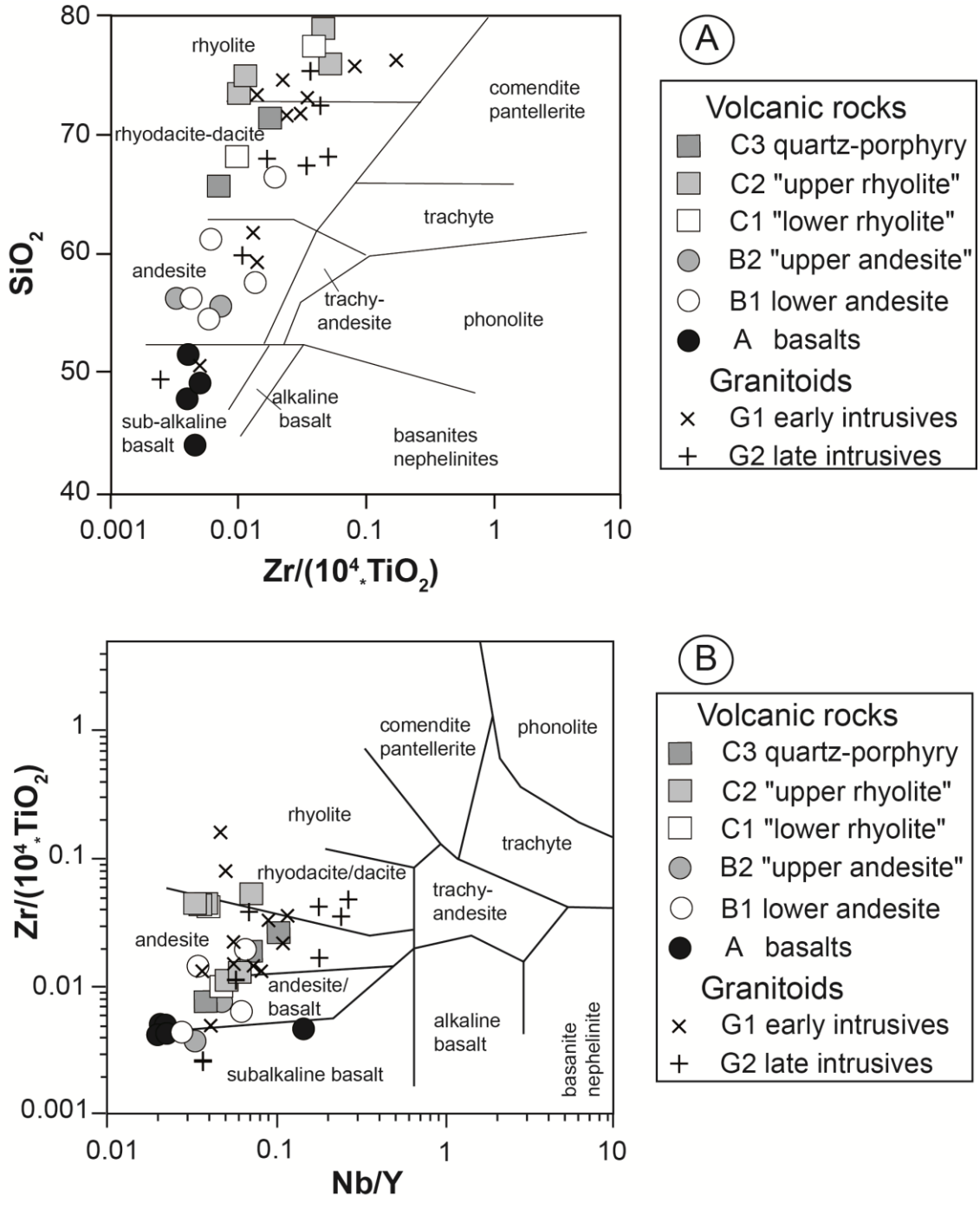

Figure 5. Classification of the Ariab belt magmatic rocks in the SiO_2 *vs* Zr/TiO_2 (A) and Nb/Y vs Zr/TiO_2 (B) diagrams (Winchester and Floyd, 1977). The use of the "immobile" elements Zr and Ti partly alleviates the bias introduced by the intense hydrothermal alteration affecting most volcanic and many plutonic rocks (see text).

2.3.2 Regional hydrothermal metamorphism of the Ariab Series

A propylitic assemblage (chlorite-albite-actinolite-epidote-pyrite) reveals a penetrative hydrothermal alteration in the basalts and andesites of the A and B units. It is also found as porphyroclasts in the S1 schistosity. In the andesites, relictual chlorite-epidote-calcite amygdales may also be recognised.

The felsic rocks from the C unit occur as quartz-albite-sericite-pyrite ± chlorite ± tourmaline schists. The latter result from the metamorphism and deformation of pre-kinematically altered rocks (silicification, quartz-sericite-pyrite acid leaching), and exhibit in particular pyrite porphyroclasts rimmed by quartz pressure-shadows, and schistosed silicified fiammes. A chlorite ± quartz± pyrite ± epidote pre-kinematic assemblage replaces former phenocrysts. At Hadayamet, hydrothermal leaching produced per-aluminous facies converted into dalmatianite during the subsequent tectonic and thermal events.

These alterations were likely related to the massive sulphide deposition. They are most pronounced in the units hosting the VHMS deposits (B2, C1, C2) and attain their maximal development in the vicinity of the deposits themselves. Deformed pyrite-chlorite networks are thus found in B2 unit, and chlorite-quartz-sericite microfracture networks in C2, both features being likely paleo-stockworks.

On the other hand, silica alteration is linked to the massive sulphide bodies, usually in the hanging-walls, and expressed as a pervasive replacement of other minerals by quartz.

2.3.3 Early granitoids (G1 suite)

Early granitoids make up to 40% of the Ariab-Arbaat belt's outcrops, generally occurring in the antiform cores. Along their margins, G1 intrusions display a penetrative foliation concordant with the regional S1 schistosity (see below). Remnants of the contact metamorphic aureolas occur as pre-kinematic assemblages of large actinolite-epidote-magnetite porphyroblastic assemblages (now, porphyroclasts) in the mafic to intermediate rocks, and of cordierite and

andalusite in the felsic lavas of the Ariab Series close to the G1 margins. The G1 suite was therefore clearly emplaced pre-kinematically within the Ariab Series.

The G1 suite is a typical I-suite consisting of biotite-hornblende granites to granodiorites, tonalite-trondjhemites, and minor quartz-diorites (Fig. 5). Fine-, medium- and coarse-grained varieties (the latter, more abundant) coexist in the intrusions. The fine-grained facies predominates and consists of a porphyritic biotite granodiorite, with showing plagioclase (oscillatory zoning around An35 compositions), corroded quartz and rare K-feldspar phenocrysts. Only large rounded quartz phenocrysts are found in the coarse-grained variety.

2.3.4 Late (post-kinematic) granitoids (G2 suite)

Large plutons of undeformed equant granodiorite and granite (with minor tonalite) intrude, with sharp contacts and chilled margins, all the Ariab series members, including the E-unit. They produced contact metamorphism marked by post-kinematic biotite-chlorite assemblages. The dominant facies in the G2 suite is a biotite porphyritic granodiorite, with mainly K-feldspar and usually zoned An30-40 plagioclase phenocrysts (Fig. 5).

To the NE of the studied area, the G2 granitoids are known to be both intrusive and reworked in the Awat-Asoteriba series, meaning that they are partly coeval with this series, in agreement with the 723 ± 4 Rb-Sr age of the Awat-Asoteriba series and the 720-680 Ma ages of the G2 suite.

A faint deuteric alteration is present in the granitoids (K-feldspar sericitisation, biotite chloritisation) and could have been coeval with the widespread propylitisation observed within the Awat-Asoteriba series.

2.4. Geochemistry and geodynamic setting of the Ariab belt

Table 1 provides representative analyses of the main rock-types of the Ariab series and the two granitoid suites.

2.4.1. Volcanic rocks of the Ariab series

Alteration effects: As could be expected from the petrographical data, many analyzed samples display evidence of alteration effects, as, for example, high LOI values (up to 11%, Table 1). The A-B multi-cationic diagram of Debon & Le Fort (1988) was used to discriminate the effects of the alteration on the bulk rock compositions. In this diagram, the alumina excess (as A = Al-Na-K-2Ca, in milli-cations) is plotted vs the mafic charge (as B = Fe+Mg+Ti, in milli-cations). It is sensitive to the effects of either propylitisation or phyllic alteration. In this diagram, most volcanic rocks from the units A, B2 and C units display evidence of a significant alteration involving an increase of the peraluminous index and a rise in the mafic index (Fig. 6-A). From Fig. 6-A, a separation may be made between "unaltered" and "altered" rocks from the sample array (although consideration of the LOI does suggest that even "unaltered" rocks may have suffered limited alteration). Another alteration process, well seen in the field, is the silicification process, well displayed in the Q-P diagram of de La Roche (1990) in Fig. 6-C: with Q= Si-(K+Na+2Ca) (quartz excess, as milli-cations) and P= K-(Na+Ca) (feldspar balance, as milli-cations) this diagram (a combination of the classical Q-Ab-Or diagram with a Q-An-Or diagram), is well fitted for alterations involving quartz.

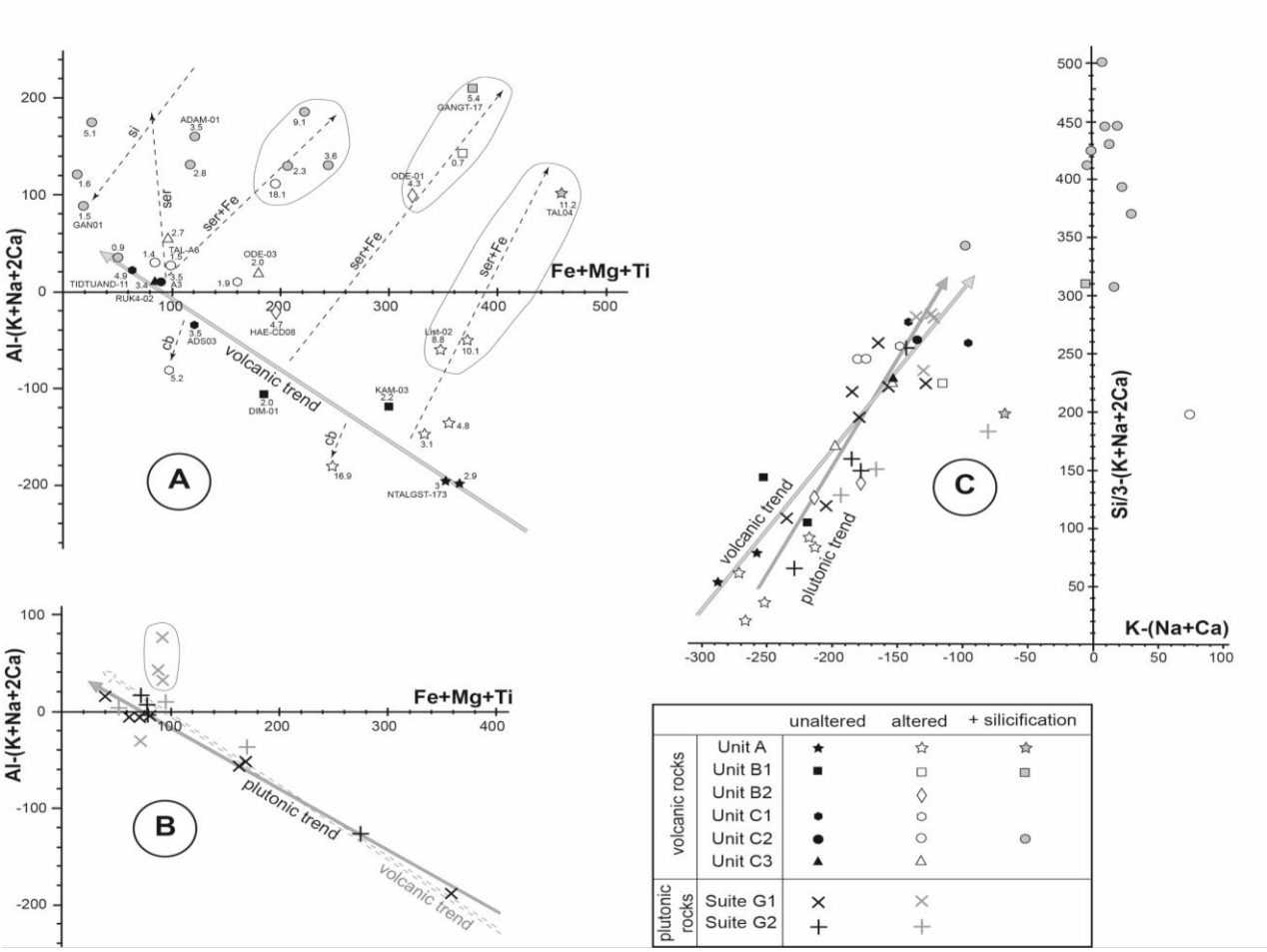

Figure 6. Projection of the Ariab belt magmatic rocks in adapted mineral-chemical diagrams. A. The A-B diagram of Debon and Le Fort (1988) for volcanic rocks of the Ariab Series. Numbers associated with rock symbols are the LOI. B. The A-B diagram of Debon and Le Fort (1988) for the Ariab-Arbaat belt plutonic G1 and G2 suites. C. The Q-P diagram of La Roche (198x) for all magmatic rocks of the Ariab-Arbaat belt. Although most of the volcanic and many plutonic rocks are affected by an intense alteration (involving an increase of the peraluminous index A), a differentiation trend, common to all the volcanic series and, at least, the G1 plutonic rocks, remains discernable in all diagrams (see text).

A quantitative assessment of these alteration effects would require a set of samples with identical initial compositions. This constraint was not satisfied with the sample array in this study. Nevertheless, a limited attempt was made, and isocons (Grant 1986) were drawn for

couples of samples from the A, B1, and C2 units, respectively, selected based on their relationships in the A-B diagram (Fig. 6-A). Assuming constant Al, practically all the elements are more or less mobile, except possibly Si (Fig. 7). A problem arises from the Zr behaviour: always well correlated with Hf, Zr is apparently either depleted or added in significant quantities (in Fig. 7, the "zircon line" is often very far from the isocon line as defined by Al). These apparent depletions or enrichments are anti-correlated with apparent enrichment or depletion in Cr. They could reflect primary differences between each couple's samples related to different partial melting ratios in the source. Thus, Cr is known to be enriched, whereas HFSE and HREE are depleted when partial melting increases in the source. Also, Y and the HREE usually plot on, or close to, the "zircon line" in Fig. 7.

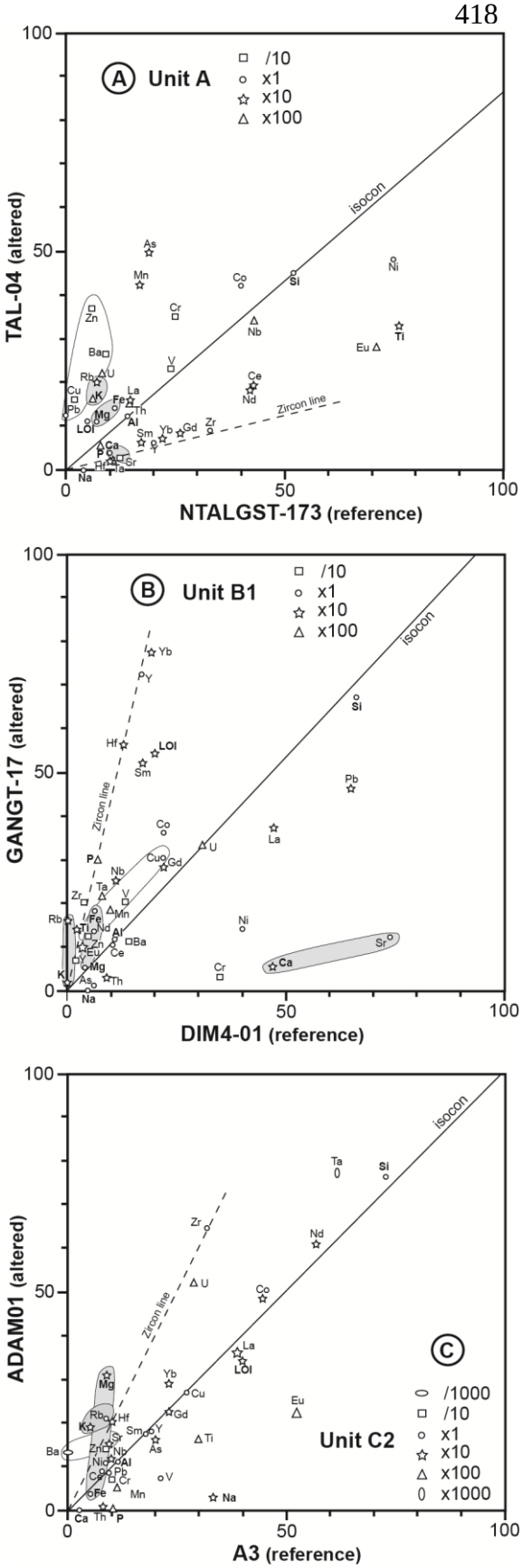

Figure 7. Isocon plots (Grant 1986) for selected couple of "unaltered"-altered rocks from (A): Unit A basalts; (B): Unit B1 andesites; and (C): Unit C2 rhyolites.

As a consequence, the apparent elemental mobility displayed in the isocon plots could be, at least partly, due to primary differences between the compared rocks. Two different behaviours are distinguished: i) some elements are either enriched/depleted in correlation with the apparent enrichment/depletion in Zr-Hf or Cr and can be considered as rather "immobile" elements, and ii) others behave independently and are considered as "mobile" elements.

Among the "mobile" elements, there are those that behave very consistently in all the units: Fe and Mg are gained, as K and Rb, whereas Ca and Na are systematically depleted. Sr follows Ca excepted in the samples with a strong introduction of Ba, where Sr correlates to the latter (Fig. 7-A, B, and C). Destructive alteration of plagioclase explains the Ca, Na, (Sr) depletions, whereas chloritisation is responsible for increasing the mafic elements. Mg input testifying for seawater involvement and thus confirming the field evidence for submarine volcanism) and sericitisation explains the behaviour of K and Rb. When present, Fe input is often higher than Mg input, in correlation with very high LOI, consistent with pyritisation. In the same way, Ba is often enriched through the alteration process, notably in the C unit, reflecting there the presence of primary deposits of massive barite (see below, § III-2). Other "mobile" elements behave more erratically: the base metals (Cu, Pb, Zn), U (mostly added, however), P and Ti. Certain elements, as Ce, are often immobile, anyway. Eu represents a particular. Thus, Eu is "mobile", being often depleted, except in the basalts, where it is added. It could reflect fractional crystallization in the andesite-rhyolites series or cumulative processes in basalts. However, considering the REE profiles in Fig. 8, the intensity of the negative Eu anomaly is correlated to the intensity of alteration, particularly in the felsic metavolcanics, leading to consider Eu as a "mobile" element, and leached together with Ca and Sr during plagioclase destructive alteration. Nevertheless, as pointed by Lesher and Campbell (1987), it is likely that alteration did not create the Eu anomaly (when present) and was only responsible for its enhancement. These findings are consistent with the current knowledge on the mobility during alteration of

elements such as Sb, Cs, Pb, Rb, Ba, K, U and P (Utsunomiya et al. 2006, and references therein), and, indeed, with the somewhat erratic behaviour of most LILE in the spidergrams in Fig. 8 to 11.

Among the “immobile “ elements, a distinction arises between those that correlate positively with Cr (i.e., increasing with partial melting in the source): La, Th, As; and those that correlate negatively with Cr (i.e., following zircon): Y, Yb, Sm, Gd, Nb, Ta.

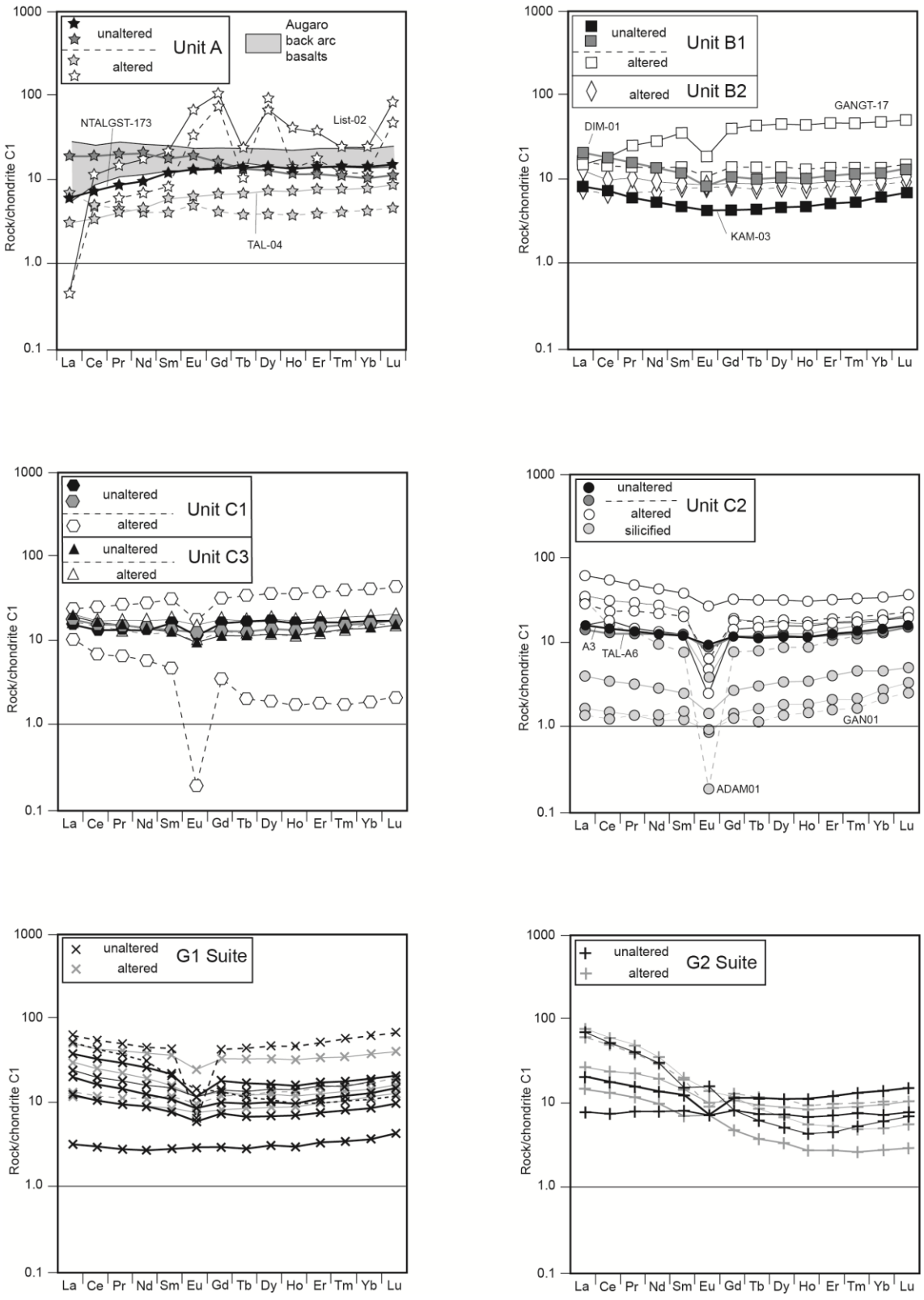

Figure 8. Chondrite-normalized REE plots for the Ariab belt magmatic rocks (C1 chondrite normalizing values from Anders and Grevesse 1989). Data from the Augaro back-arc basalts in Eritrea (Teklay et al. 2003) have been added to the Unit A plot for comparison (see text).

Most of the REE and HFSE, currently used for constraining magmatic rocks' origin and geological setting, may be taken as practically immobile through the alteration (e.g., Lesher et al. 1986; Lesher and Campbell 1987). The element ratios are also not significantly affected by alteration (e.g., Condie, 2005). This contention may be extended to the Ariab series, as indeed may be seen in Fig. 8, 9, 10 (and 11), in which alteration has no significant impact on the HREE and HFSE profiles.

Geochemical characterisation: The less altered rocks of the Ariab Series are metaluminous to weakly peraluminous, low in K_2O (from less than 0.1% in the Unit A basalts to up to 1.34% in the Unit C rhyolites) and rather iron-rich (Fe# [FeO*/FeO*+MgO] from 0.5-0.6 in the basalts to 0.8-0.9 in the rhyolites). They display in the A-B and Q-P diagrams a typical calk-alkaline trend (Fig. 6-A and C).

All lithologies from these three units display similar characteristics:

- The chondrite-normalised REE profiles (Fig. 8) are flat, with very low $[La/Yb]_N$ (from 0.4 to 1.4, with a slight increase in the C Unit felsic lavas) and $[Gd/Yb]_N$ (from 0.7 to 1.5) ratios. The Eu negative anomalies in the less altered rocks are either absent (or even positive), as in Unit A basalts and andesitic basalts (Eu/Eu* between 1 and 1.19), or moderate as in Unit B basaltic andesites and andesites (Eu/Eu* between 1 and 0.73) and Unit C rhyodacites and rhyolites (Eu/Eu* between 0.72 and 0.96). More pronounced negative anomalies are present, mainly in the felsic rocks, but this is due to the alteration effects discussed in the previous section. Either significant plagioclase fractionation (e.g., Lesher et al. 1986) or a plagioclase restitic phase in the source (e.g., Hart et al., 2004) may explain the negative Eu anomalies in similar metafelsic rocks. In the case of the Ariab series, we must conclude that these processes were of far lesser importance in their genesis. Silicification effects are particularly evident in

the REE profiles, acting as a diluting effect (obviously superimposed upon the plagioclase-destructive alteration responsible for most of the Eu anomalies) (Fig. 8).

- The MORB-normalized spider diagrams (Fig. 9) show LILE enrichment and HFSE depletion.

Except for the Unit A basalts, there is consistently a positive anomaly in K-Rb-Ba, with a clear Ba spike contrasting with a constant Sr depletion, accentuated in the altered rocks. The Ba enrichment is amplified with alteration, particularly in the C Unit felsic rocks. It may be suspected that K-Rb depletion in the basalts is due to an early “spilitisation” on the seafloor with K to Na exchange and Mg enrichment (e.g., Lentz 1998). Such alteration ("keratophyrisation" in felsic rocks) could have been present in all Ariab lithologies and then masked by subsequent K-Rb hydrothermal enrichment associated with sericitisation. Yet, it seems complicated to assign the low-K nature of the Ariab series to alteration processes only: it seems likely that whatever alteration processes were in operation, they only accentuated the initial geochemical signature. Thorium, always relatively enriched compared to niobium, is either depleted (Unit A) or enriched (Units B and C).

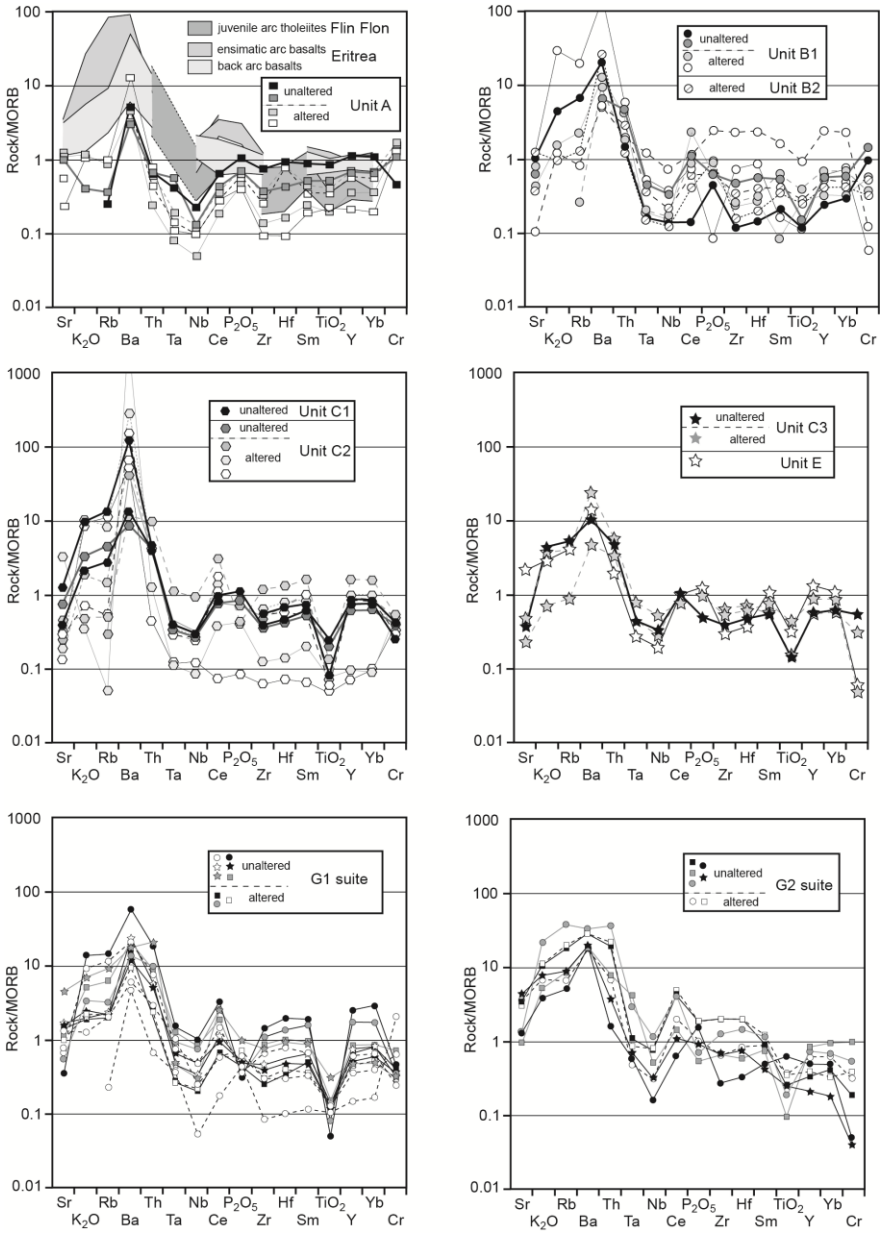

Figure 9. MORB-normalized plots for the Ariab-Arbaat belt magmatic rocks, using the normalization and ordering scheme of Pearce (1983) (in Rollinson 1993), with LILE on the left and HFSE on the right, and incompatibility growing outward from Ba-Th (save the Cr addition on the right). Data for comparison with Ariab basalts: Flin Flon arc tholeiites, redrawn from Syme et al. (1998); Eritrea arc and back-arc basalts, redrawn from Teklay et al. (2003) (see text).

Among the HFSE, Ti and Ta-Nb display a strong negative anomaly, whereas Ce-P and Hf are always slightly enriched relatively to Zr. The Ti/V ratios are still ≤ 20 in the basalts and andesites (Units A and B), contrasting with elevated values (generally > 100) in the felsic rocks, due to a dramatic lowering in the V contents (see Table 1).

Chromium is usually depleted, with the only exception of the B1 Unit andesites. This depletion may be related to either higher partial melting ratios in the sources or fractional crystallisation processes in a magmatic chamber.

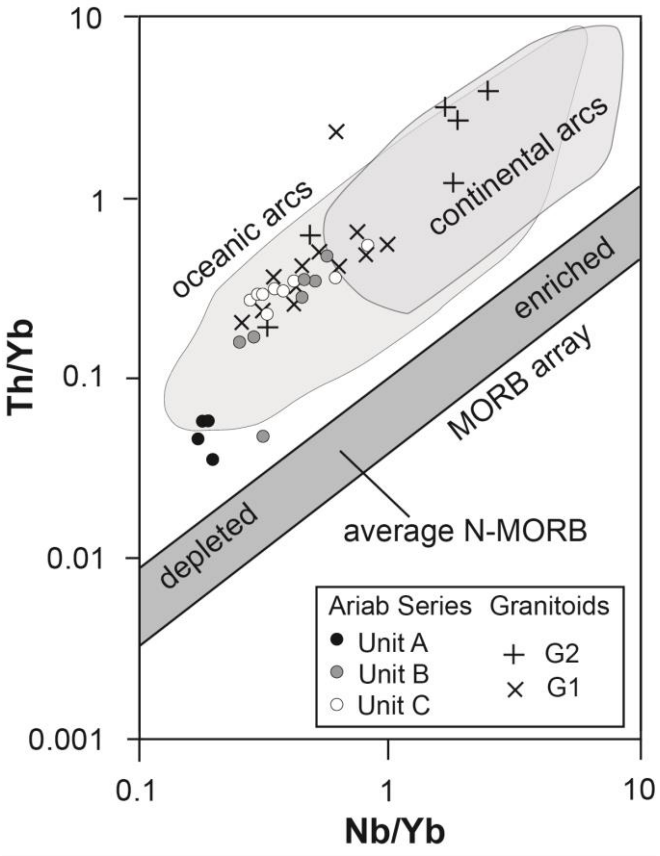

Figure 10 Projection of the Ariab-Arbaat belt volcanic rocks in the Th/Yb *vs* Nb/Yb diagram of Pearce and Peate (1995), showing clearly their oceanic island-arc affinity. G1 and G2 suites have also been projected for comparison.

All these features are consistent with a subduction-related setting (e.g., Rollinson 1993). Moreover, the B and B Units' basalts and andesites display characteristics that are most

suggestive of an ensimatic juvenile arc environment, the Unit A basalts, particularly with their low-K and very low $[La/Yb]_N$ signatures, being arc tholeiites. A back-arc environment for the mafic and intermediate lavas of the Ariab series may be excluded based on the low Ti/V ratios (back-arc basalts displaying Ti/V consistently>20, Rollinson 1993) and direct comparison with reference series. In Fig. 9, basalts from the A Unit are compared with juvenile arc tholeiites from the Paleoproterozoic Flin Flon Belt (Canada) and with both ensimatic arc and back-arc basalts from the nearby Neoproterozoic greenstones in Eritrea. It is apparent that the mafic rocks from the Ariab series display MORB-normalised profiles more similar to those of the arc basalts than to back-arc ones. The latter lacks the strong Nb anomaly and the Ce-P relative peak that typify the arc tholeiites, a feature seen on the Ariab series REE profiles (Fig. 8). Finally, the Th/Yb vs Nb/Yb relationships (Pearce and Peate, 1995) equally strongly point towards an oceanic island-arc setting for the mafic, intermediate, and felsic rocks (Fig. 10).

Unit C's felsic rocks (especially those of Unit C2) are discussed in more detail as they host most of the Ariab VMS and massive barite deposits. There is indeed a special relationship between felsic lava's characteristics and their capacity to host such deposits (Lesher et al. 1986; Lentz 1998; Hart et al., 2004). Hart et al. (2004) define four classes of felsic lavas, FI to FIV: (i) FI dacites and rhyodacites, displaying steep REE profiles ($[La/Yb]_N$ 6-34) high Sr and Zr/Y ratio (9-31), low HFSE contents, and negative to moderately positive Eu anomalies (Eu/Eu* 0.87-2.0), (ii) FII rhyodacites and rhyolites displaying gentle sloping REE profiles ($[La/Yb]_N$ 2-6), moderate Zr/Y ratio (6-11), intermediate Sr and HFSE contents and variable Eu anomalies (Eu/Eu* 0.35-1.4), (iii) FIII rhyolites displaying flat REE profiles ($[La/Yb]_N$ 1-4) and subdivided into FIIIa (low Zr/Y 4-7, intermediate HFSE, variable Eu anomaly: Eu/Eu* 0.37-0.94) and FIIIb (low Zr/Y 2-6, high HFSE, low Sr, pronounced negative Eu anomaly: Eu/Eu* 0.2-0.61) subtypes, and (iv) FIV rhyolites, similar to FIIIa subtype but displaying very flat to slightly LREE-depleted REE profiles, low REE and low HFSE contents. While FI felsic rocks

are always barren, some FII and many FIII (mainly Archean) and FIV groups are associated with VHMS districts. According to Hart et al. (2004), FIII-IV magmas are the products of repetitive partial melting of a single "hydrated basalt source" with an only minor contribution (if any) of a crystal fractionation process. The Unit C felsic rocks of the Ariab Series display all the FIIIa and FIV groups' characteristics, including a very low Zr/Y ratio, between 1.6 and 3.6. Fig. 11 compares felsic rocks from the C2 sub-unit with FI to FIII references (Lesher et al. 1986) and with two VHMS-hosting felsic rocks from FIV group (Lentz 1998): the Paleoproterozoic Flin Flon Belt, Canada (Syme et al. 1988; Whalen et al. 1998) and the Neoproterozoic Stirling lavas from Cape Breton Island, Nova Scotia (Dostal et al. 1992). Both are members of arc tholeiite suites in juvenile oceanic arcs, displaying a characteristic "bi-modal" arrangement with a few andesites intermediate between basalts and andesi-basalts, on the one hand, and rhyodacites and rhyolites, on the other hand. This bi-modality is a feature equally visible in the Ariab Belt.

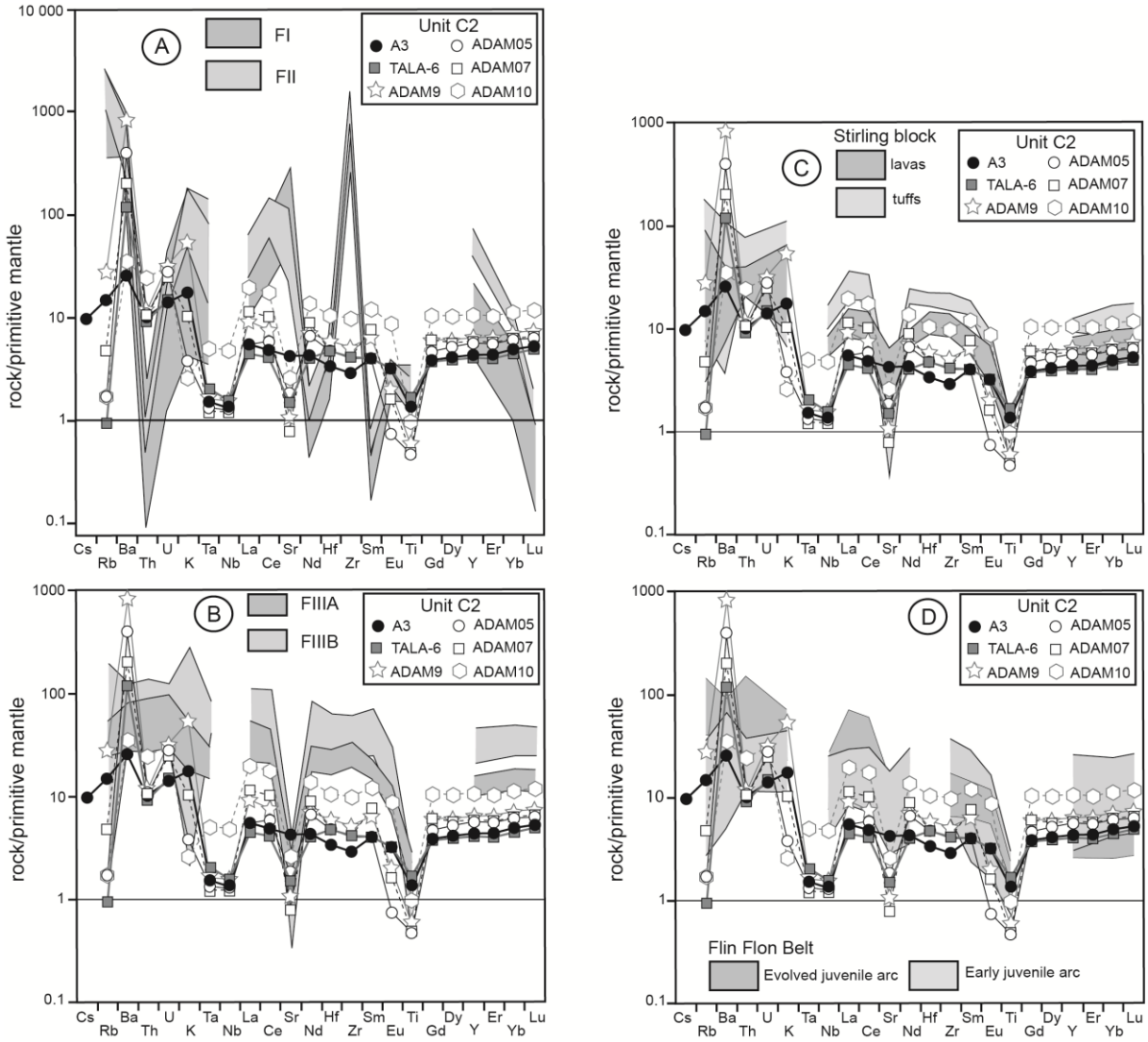

Figure 11. Comparison of C2 felsic lavas with reference series in primitive mantle-normalized LILE-HFSE plots (normalizing values from Ringwood 1991). A: Comparison with the FI and FII Archean felsic metavolcanic rocks (redrawn from Lesher et al. 1986). B: Comparison with the FIIIa and FIIIb Archean felsic metavolcanic rocks (redrawn from Lesher et al. 1986). C: Comparison with the Neoproterozoic Cape Breton Island felsic metavolcanic rocks from an ensimatic arc (redrawn from Dostal et al. 1972). D: Comparison with the Paleoproterozoic Flin Flon Belt felsic metavolcanic rocks from a primitive ensimatic arc (redrawn from Syme et al. 1998).

2.4.2. Early granitoids (G1 suite)

Although affected to some extent by hydrothermal alteration, the G1 granitoids display in the A-B and Q-P diagrams a typical calk-alkaline trend, identical to the volcanic trend (Fig. 6-B and C). They are metaluminous, K-poor ($K_2O \leq 2.04$), and rather Fe-rich (Fe # from 0.5 in the more mafic term to 0.8). They display flat REE profiles (Fig. 8), similar to those of the A unit for the more mafic facies and the C unit for the more felsic rocks. Compared to the C unit profiles, however, they are slightly more fractionated ($[La/Yb]_N$ 0.9-2.1), the HREE fractionation and the deepening of the negative Eu anomaly (Eu/Eu* 0.57-1.04) being correlated. The MORB-normalised plots again compare well with the C unit plots (Fig. 9), although there is only a Ce positive anomaly, P being relatively depleted. These features are consistent with an oceanic arc-setting (Fig. 11). As the G1 granitoids are very close in composition to the C unit's felsic volcanics, a genetic connection is possible. Thus, the G1 plutons could have been the feeders for all or a part of the C unit felsic extrusives (in particular, C3 sub-unit), or the reworked volcaniclastics of the E unit.

2.4.3. Late granitoids (G2 suite)

The G2 granitoids are calk-alkaline metaluminous rocks (Fig. 6-B), close in composition to granitoids of the G1 suite. They are K-poor ($K2O \leq 1.76$) and rather Fe-rich (Fe# from 0.7 to 0.8). Compared to the G1 suite, however, they display steeper REE profiles (except for the more mafic terms), with $[La/Yb]_N$ between 1.1 and 15.4, and the Eu anomalies are more variable (Eu/Eu* 0.58-1.44) (Fig. 8). Besides, in the MORB-normalised plots, the Ti negative anomaly is smoothed or absent (Fig. 9). These characteristics refer the G2 suite to the FII or even the FI groups of Hart et al. (2004), favouring an arc-setting, however more akin to a continental arc than the G1 suite (Fig. 10).

2.4.4. Summary: the geodynamic setting of the Ariab belt

In conclusion, the petrographic and geochemical evidence points to the lower suites of the Haya terrane representing the remains of a mature island-arc, with volcanic activity shifting from an early submarine mafic (immature) stage (A unit) to a final shallow marine to subaerial felsic (mature) stage (C and E units, G1 suite). By contrast, felsic intrusions of the G2 suite testify for a mature continental arc setting.

3. GOLD MINERALIZATIONS

Until recent times, gold from the Ariab area mainly came from Miocene supergene enrichments of earlier gold (pre)concentrations in massive sulphide deposits, as gossans – the so-called "silica barite rocks (SBR)" (Recoché 1989). However, it appears that primary gold is not restricted to massive sulphide deposits as three primary gold-bearing associations are now recognised: (i) gold in VHMS deposits, ii) related massive barite and exhalative hematite-magnetite schists, (iii) gold hosted by pre-orogenic quartz veins (Kamoeb), and (iv) gold within carbonate-pyrite-quartz alteration zones related to D3 SZ (Derbikwan), and v) supergene gold enrichments (mantos).

3.1. Gold-bearing massive sulphide (VHMS) deposits

3.1.1. General characteristics

More than 20 lenses (or lenses clusters) of massive sulphide (≥ 60 % pyrite) are known in the Ariab belt (Fig. 12). They are mostly hosted by the felsic members of the Ariab Series (C1 and C2 sub-units). They were generally strongly deformed during the D1 event, and many primary features may have been obliterated. Nevertheless, it is possible to reconstruct gross pre-kinematic features. The massive sulphide bodies appear to have been concordant layered lenses,

with a high aspect ratio (2-25 m x 1,500 m). The presence of a pipe-like stockwork cannot be demonstrated. The footwall sulphide disseminations and diffuse stringer stockworks (down to 30 m) within strongly altered volcanic rocks (quartz-sericite-chlorite-pyrite), seems to have been evenly distributed beneath the massive sulphides. Clear zoning is expressed, with a central chlorite-rich zone, grading outward in a quartz-sericite zone. Pyrite is ubiquitous, as early dissemination or stringers (Fig. 13-a). Chlorite is a ripidolite. It may be associated with a tourmaline (hydroxy-feruvite), for example, at Medadip. The sericite is usually a Ba-rich phengite, up to 4.18 BaO wt. % (Fe-rich when shielded in early pyrite), apparently responsible for the systematic Ba enrichment associated with alteration (see the previous section).

The primary mineral association was pyrite ± chalcopyrite ± sphalerite, with a noticeable lack in base metals (1.3 % Cu, 2 % Zn on average) and a very low Pb content, in good agreement with the oceanic setting of the Ariab arc. The gold grade varies from 0.6 to 1.2 $g.t^{-1}$ as an average. The Ariab massive sulphide deposits may be classified as polymetallic VHMS of the Zn-Cu type (Franklin 1993).

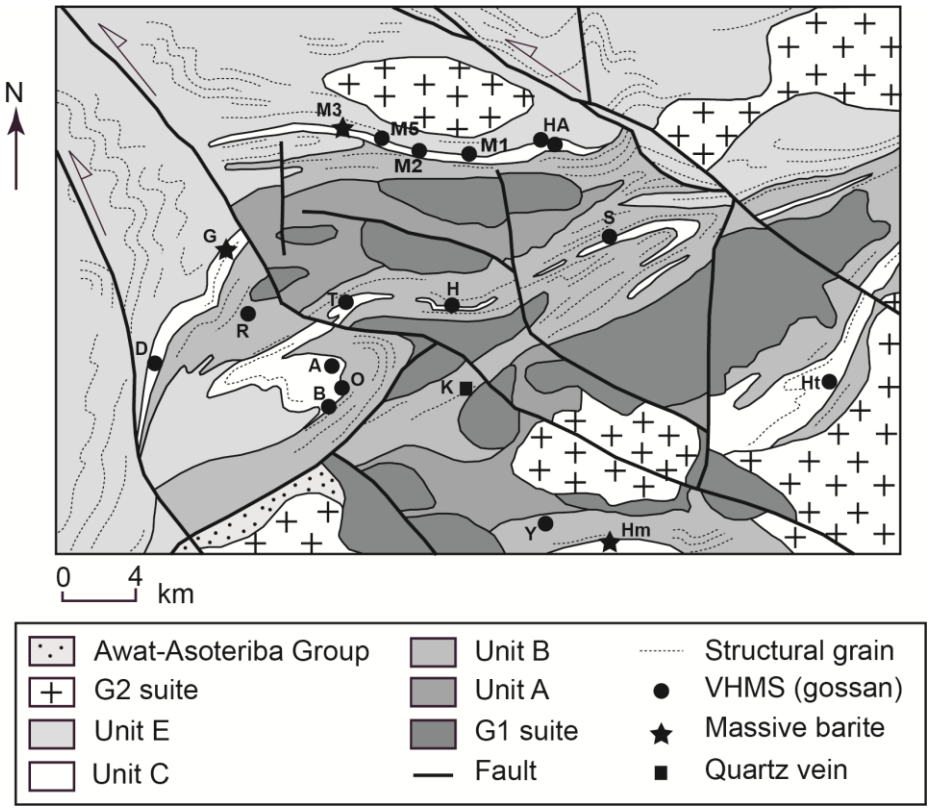

Figure 12. Geologic map of the central part of the Ariab area, with the main gold occurrences (redrawn from Abu Fatima 2006).

A Adasselakh B Baderuk D Dimdim G Ganaet H Hassai HA Hadal Aouatib Hm Hamim Ht Hadayamet K Kamoeb M1-M5 Medadip 1 to 5 O Oderuk R Rukab S Shidimam T Talaiderut Y Yonim

3.1.2. Post-depositional history and the timing of gold deposition

Based on a detailed study of the mineral/deformation relationships, Abu Fatima (2006) reconstructed the complicated history following the syngenetic deposit of primary sulphides and footwall alteration (Fig. 14).

(i) Syn-G1 recrystallisation: the transformation of pyrite into pre-kinematic magnetite 1 is currently observed in the massive sulphides, and seems spatially correlated with the relicts of syn-G1 contact metamorphism in the surrounding volcanic rocks.

(ii) Syn-metamorphic recrystallisation: chlorite and muscovite currently define the main S1 schistosity, with numerous porphyroclastic remnants of the pre-kinematic assemblages (Fig. 13-b). The massive sulphides may be strongly reworked, with superimposition of a syn-D1 metamorphic banding, as either layers with ductile elongation in S1 chalcopyrite (Fig. 13-c, d) or cataclastic bands of microcrystalline pyrite (py1) wrapping pyrite porphyroclasts or both (Fig. 13-e).

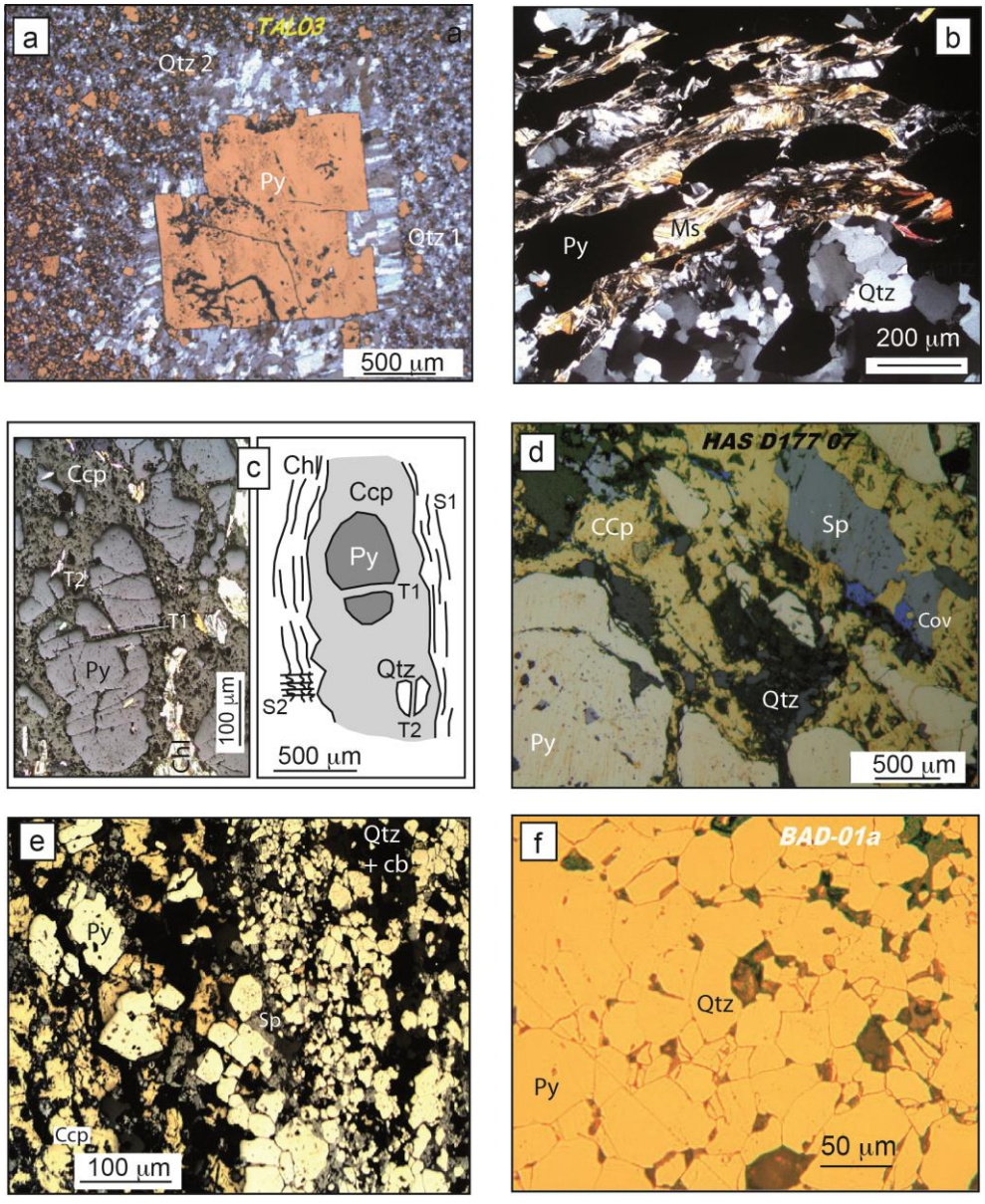

Figure 13 Post-depositional transformations in the VHMS deposits. **a**. Porphyroclastic pyrite (py) in a quartz-sericite matrix (diffuse stockwork, Talaiderut) Qz1 and 2: two generations of syn-kinematic fibrous quartz ("pressure-shadows"). **b**. Porphyroclastic muscovite (mus) and

pyrite (py) in a schistosed stockwork (Medadip 1) quartz: quartz amygdale. **c**. Differential behaviour of massive sulphides during deformation (Yonim): fractured pyrite (py) and ductile chalcopyrite (cp) (left); sketch of relationships in the same thin section (right) chl: chlorite; qtz: porphyroclastic quartz; S1, T1, and S2, T2: two generations of schistosity and related tension gashes. **d**. Differential behaviour of massive sulphides (Hassai): porphyroclastic pyrite (py) and sphalerite (sp) fractured and enclosed in ductile chalcopyrite (cp) elongated in S1; Qz: quartz; cv: supergene covellite. **e**. Two pyrite generations in the massive sulphides (Medadip 5): cataclastic pyrite (py1), quartz (qz), and chalcopyrite (cp) banding (S0+S1) and porphyroblastic euhedral pyrite (py2). **f**. Annealed pyrite (py) (Baderuk) Qz: quartz.

Sphalerite may be present as porphyroclasts, embedded into remobilized chalcopyrite, sometimes with chalcopyrite disease (Fig. 13-d) or be itself remobilized, being often associated with chalcopyrite in "pressure-shadows" around pyrite. Most often, massive pyrite aggregates are fractured, with fibrous quartz infillings, in two grossly orthogonal directions, reflecting the changing shortening directions from D1 to D2 (see above, section II-4).

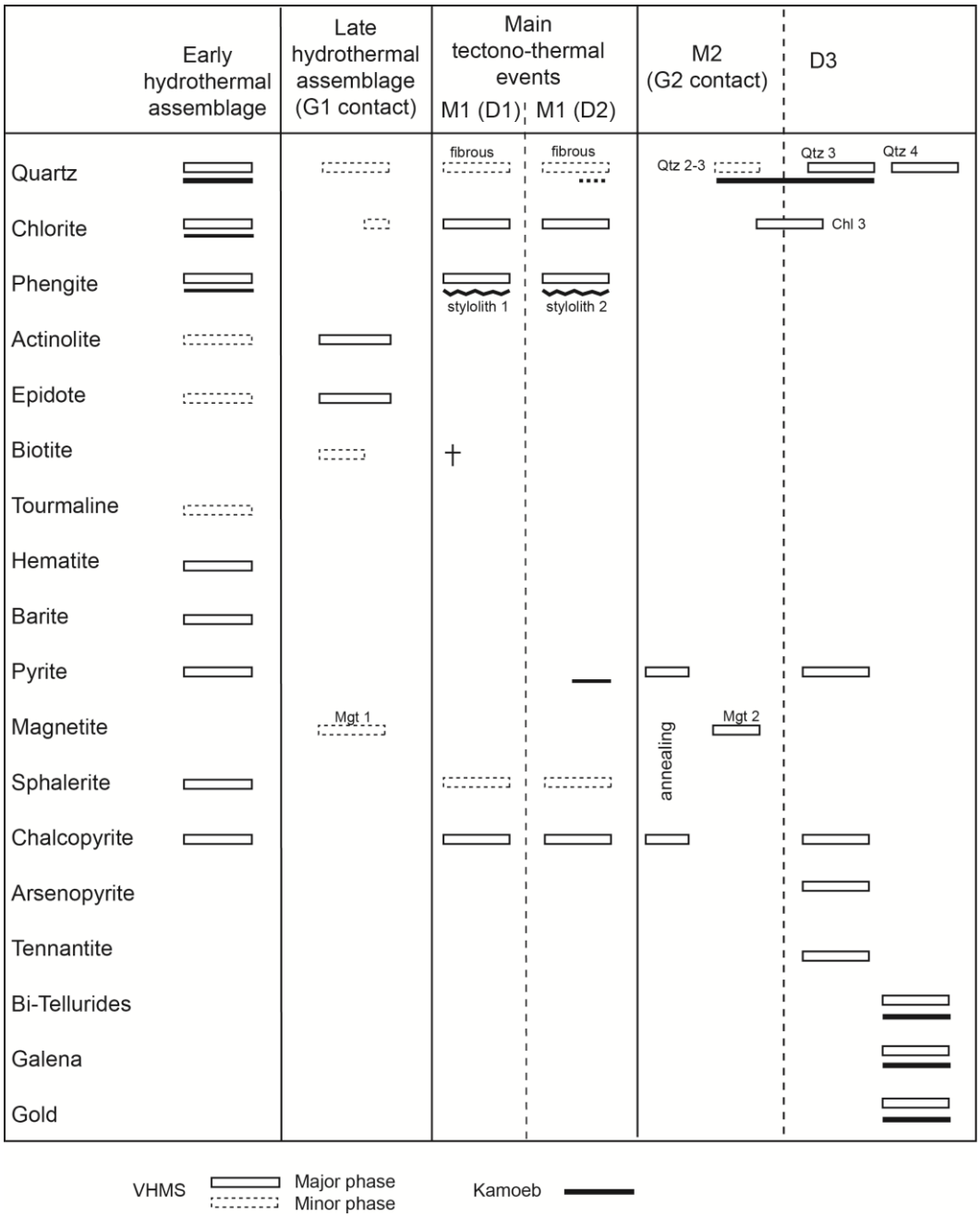

694

695 Figure 14. Paragenetic evolution in the VHMS and Kamoeb deposits.

696

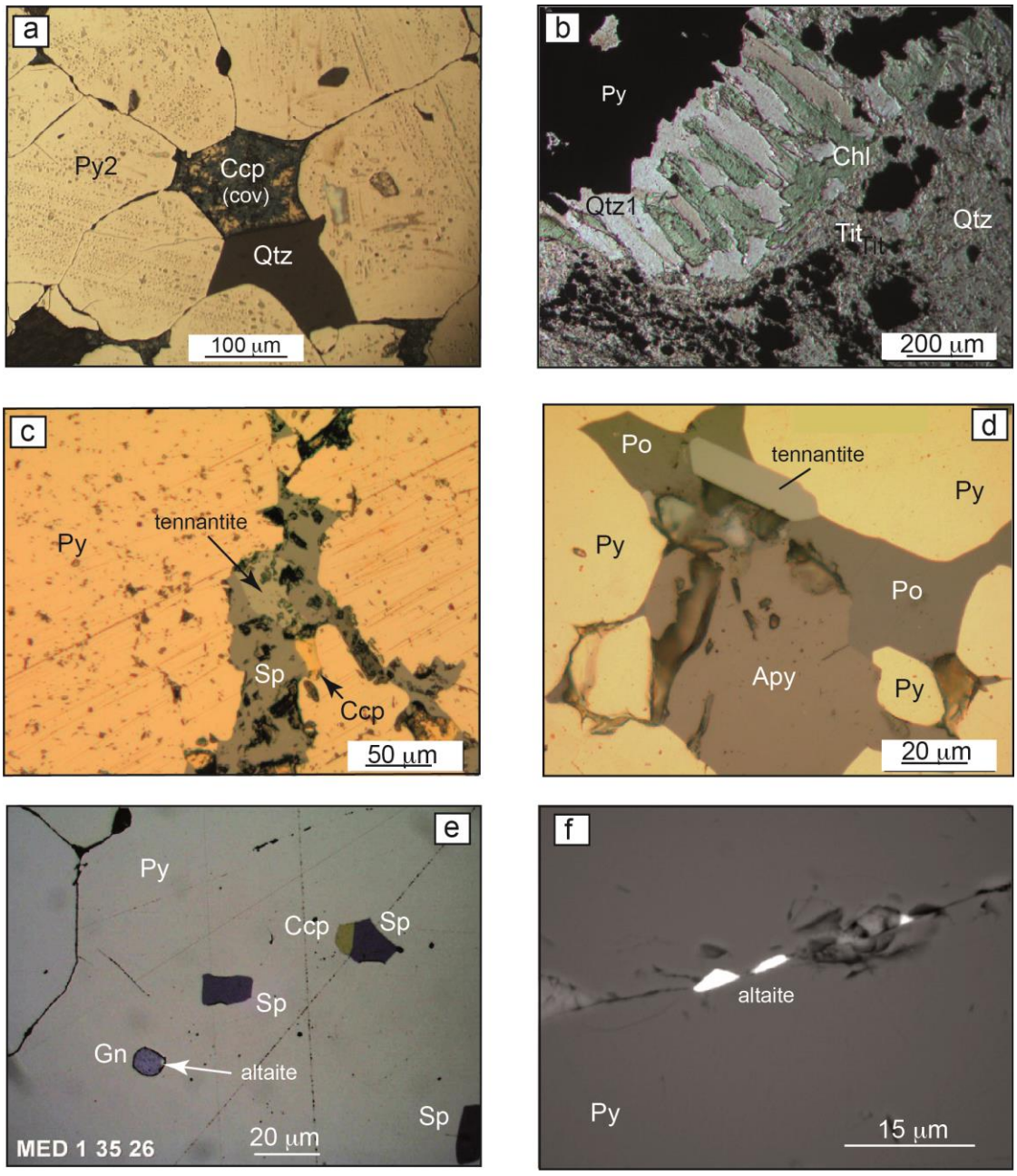

Figure 15. Late events in the massive sulphides. **a**. Quartz (Qtz) and chalcopyrite (Ccp) possibly recrystallised with pyrite (Py) annealing (Medadip 5). **b**. Replacement of syn-kinematic fibrous quartz (Qtz1) by post-kinematic chlorite (Chl) (Barut) Qtz: quartz; Tit: titanite. **c**. Fracture-dissolution in pyrite (Py), filled with chalcopyrite (Ccp), sphalerite (Sp), and tennantite (Hadal Ouatib). **d**. Dissolution cavity in pyrite (Py), filled by pyrrhotite (Po), arsenopyrite (Apy), and tennantite (Hassai). **e**. Microvugs inside annealed pyrite (Py), filled with sphalerite (Sp), chalcopyrite (Ccp), galena (Gn), and altaite (SEM-BSE, Medadip 1); note that the microvugs

developed independently from the pyrite joints. **f**. Microcrack in pyrite (Py) with altaite sealings (SEM-BSE, Hadal Aouatib).

(iii) Development of post-kinematic euhedral pyrite (py2) (Fig. 13-e) and pyrite annealing, without conspicuous BMS accumulations at the triple junctions except for a few chalcopyrite grains (Fig. 13-f and 15-a), are often (although not systematically) observed. The timing of this event is obscure, as it may record either the peak temperature of metamorphism associated with the relaxation following the collision events or the thermal effect of G2 emplacement.

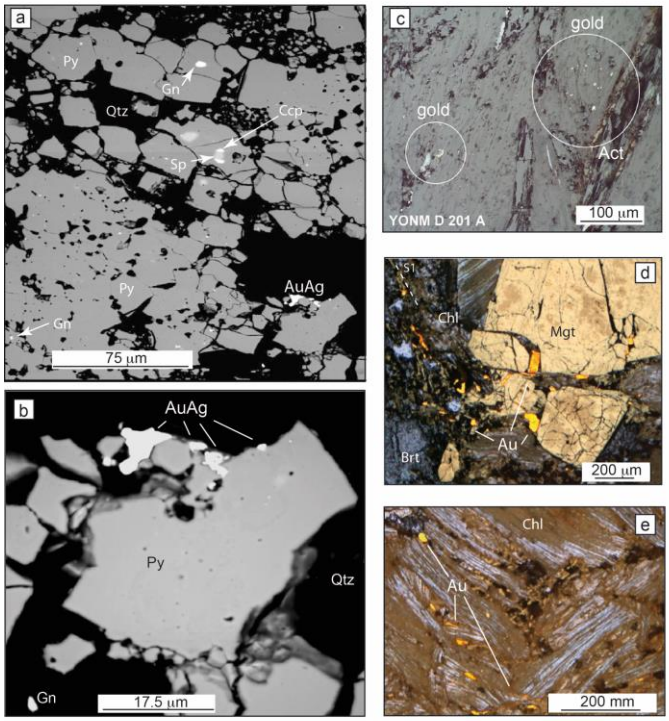

Figure 16. Gold setting in late microstructures. **a**. Brecciated microcrystalline pyrite (pyrite 1) with quartz filling (SEM-BSE, Adassedakh); Gn: galena; Sp: sphalerite; Ccp: chalcopyrite; AuAg: electrum. **b**. Detail of a: gold is associated with recrystallised pyrite in relation with the brecciation. **c**. Native gold along actinolite (Act) cleavages (SEM-BSE, Yonim). **d**. Gold (Au) in brittle fractures affecting magnetite (Mgt) and in re-activated S1 schistosity marked by

chlorite (Chl) (Ganaet); Brt: barite; Q2: fibrous (syn-D2) quartz ("pressure-shadow" around the magnetite). **e**. Gold (Au) in kinked chlorite (Chl) (D2 structure, Ganaet); note that gold is either along cleavage or cross-cutting them, demonstrating a post-D2 introduction.

(iv) Syn- G2 recrystallisation: apart from pyrite annealing, some interkinematic D2-D3 recrystallisation is observed, which may be tentatively attributed to the thermal effects of the G2 suite intrusion. These include pyrite transformation into magnetite 2, clearly distinct from the syn-G1 magnetite 1, the latter being consistently coated by syn-kinematic fibrous quartz), chlorite recrystallisation (Fig. 15-b), and quartz healing.

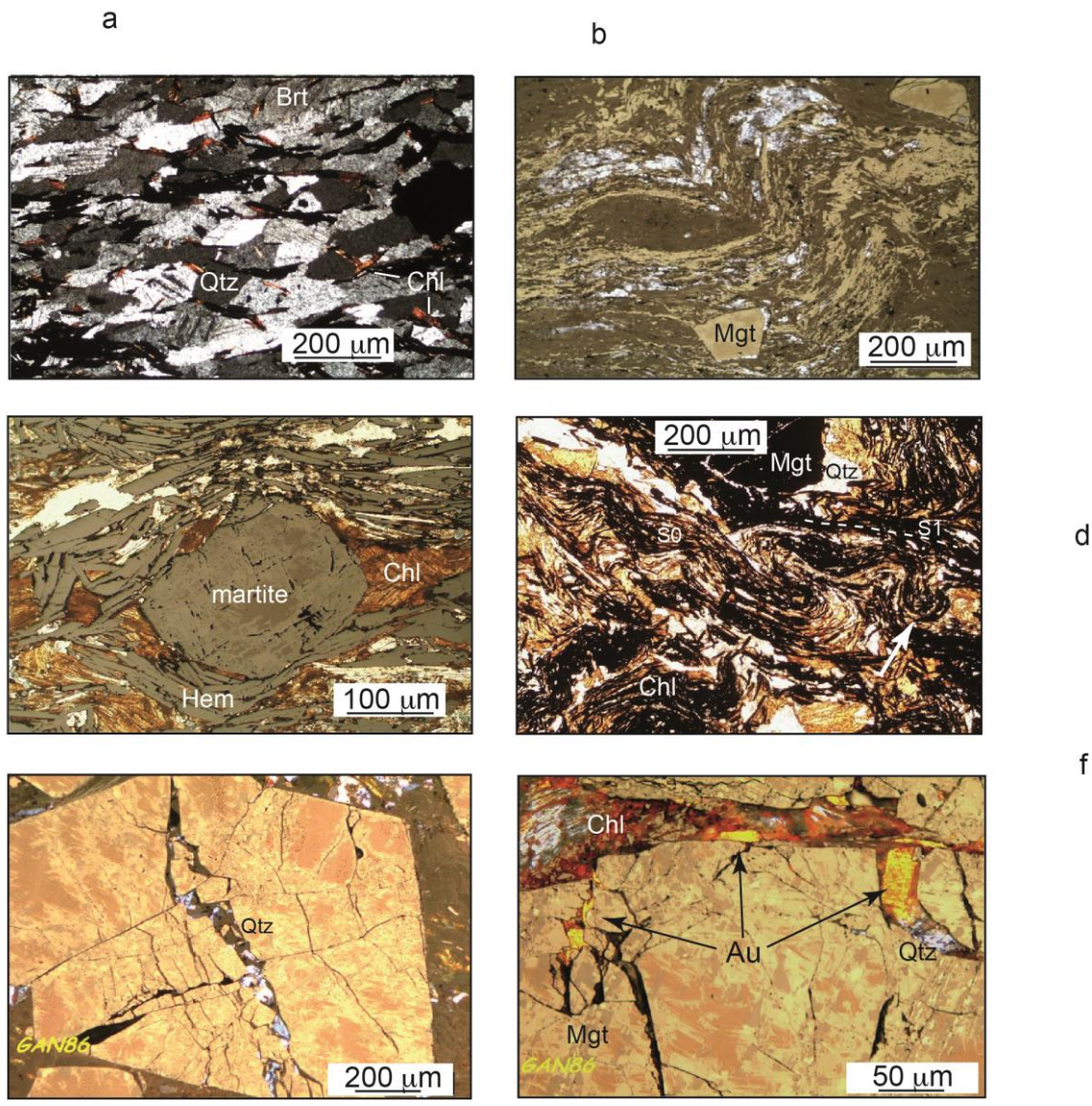

Figure 17. Massive barite and associated hematite-chlorite schists. **a**. Porphyroclastic barite (Brt) (Hamim) Qtz: quartz; Chl: chlorite. **b**. F2 microfold affecting the S1 hematite schistosity (Ganaet) Mgt: magnetite. **c**. Early magnetite (Mgt) wrapped in the S1 hematite (Hem) schistosity (Medadip 3); Chl: iron-stained chlorite. **d**. Early (pre-S1) microfolds (slumps?) (white arrow) (Hamim) S0: primary bedding; S1: main schistosity; Chl: iron-stained chlorite; Mgt: early magnetite; Qtz: quartz in "pressure-shadow". **e**. Late D3 microcracks and quartz (Qtz) infillings in magnetite (Ganaet). **f**. Gold association with late D3 microcracks in magnetite (Mgt) (Ganaet).

(v) Syn-D3 microfracturation and hydrothermal recrystallisation: microcracks with polymetallic mineralization crosscut all the preceding parageneses, including annealed pyrite and magnetite 2 (Fig. 15-c). Pyrite is often dissolved, with polymetallic mineralization coating the resulting micro-vugs (Fig. 15-d, e). Polymetallic mineralization includes pyrrhotite, chalcopyrite, sphalerite, tennantite, arsenopyrite, galena, and altaite (PbTe), but not gold. Brittle fracturing with galena-altaite sealing (Fig. 15-f) or fracturing and brecciation (hydraulic fracturing), with mainly quartz cement (Fig. 16-a), appears as slightly later.

(vi) Gold is always found as tiny particles of either native gold or electrum. It is most often associated with the latest syn-D3 manifestations (Fig. 16-a, b). More or less disseminated in the mafic silicates (chlorite, actinolite), it is systematically intercalated along the cleavages, as, for example, at Yonim (Fig. 16-c), and Ganaet (Fig. 16 d,e,f).

(vii) Post-dating gold, the latest hydrothermal events are carbonate vein fillings (mainly, calcite), usually preceding supergene alteration, and likely related to the D4 fracture event. Within the massive sulphide bodies, supergene alteration mostly affects chalcopyrite, with covellite as the main product, and to a lesser extent, pyrite.

3.1.3. Synthesis

Quantitatively, most of the BMS presently seen in the Ariab VHMS deposits (mainly, sphalerite) are expressed in the D3 hydrothermal event. Yet, sphalerite and chalcopyrite were present since the early deposition of massive sulphides and were remobilised throughout the G1 intrusive and D1-D2 tectonic-metamorphic events. Therefore, it is likely that most of the zinc and copper, now present as late-D3 BMS, was remobilised from the primary stock. The case for As is more problematic since all the observed arsenopyrite and tennantite are part of the D3 paragenesis. There is no evidence, however, of significant As contents in the primary pyrites. The timing of Ag introduction in the Ariab massive sulphides (with 18 $g.t^{-1}$ on average) also remains difficult to explain, because tennantite is the only silver-hosting mineral in these deposits.

On the other hand, gold is only seen in late-D3 micro-structures, as also it is the case for the galena-altaite association. Contrary to zinc and copper, there is no evidence of an early introduction of gold and lead. However, early galena would have been easily reworked in S1 structure, as usually in metamorphosed Pb-bearing VHMS worldwide. Early gold, if present, could have been dissimulated into primary sulphides, such as pyrite. But it would have been liberated and reconcentrated through the D1-D2 tectonic-metamorphic events, or even more likely, during the strong remobilisation of base metals at the onset of the syn-D3 hydrothermal event. That it was not observed puts a strong argument against the hypothesis of gold remobilization from a primary stock at the end of the D3 event (although this hypothesis may be realistic for silver).

There thus seems to exist a severe decoupling between gold and the main BM, the latter being part of the VHMS depositing event. In contrast, gold, together with lead, altogether rare in the Ariab deposits, were introduced later in the system, as tellurium and possibly silver.

3.2. Gold-bearing massive barite and hematite schists

Several small barite lenses (about 10mx100m) are found close to the top of the C2 unit (Fig. 4). Individual lenses contain no more than 150 to 300 kg Au, and the global resource in gold of the barite-hosted deposits is only 0.5 t @ 7.1 $g.t^{-1}$ Au. The barite lenses are usually topped by a thin layer of Mn-rich chert (1.9 to 3.1wt. % Mn) and black shales, possibly an exhalative horizon.

3.2.1. General characters

Description: The barite bodies are characterised by a conspicuous banding, with alternating barite-quartz and hematite-chlorite-barite-quartz layers (10 to 20 cm thick).

In the barite-quartz bands, barite is pre-kinematic, displaying a porphyroclastic texture (Fig. 17-a), with more or less pronounced annealing, not unlike the primary pyrite in the VHMS bodies. At the same time, quartz is remobilized as ribbon quartz.

The iron-rich bands display a laminated structure, with alternating barite (porphyroclastic)-quartz and hematite-chlorite-quartz laminas (50 to 100 μm?). The latter, platy hematite and chlorite (a ripidolite with Mg # ~ 0.5) defines S0-1 (Fig. 17-b). There are preserved amygdales showing a pre-kinematic quartz-magnetite-chlorite association, and some porphyroclastic hematised euhedral magnetites (martite) may be observed (Fig. 17-c). Locally, a pre-S1 complex folding of the platy hematite ribbon structure is well expressed, as, for example, at Medadip 3 and Hamim (Fig. 17-d).

Interpretation: The quartz-chlorite-hematite-(magnetite) layers are likely to represent metamorphosed chert-iron hydroxide hydrothermal deposits on the sea-floor, with magnetite as an early diagenetic product. Early (pre-S1) folds may be interpreted as slumps structures. These observations suggest, in turn, that the barite-quartz layers could have been of exhalative origin as well.

As a whole, the barite-iron oxide lenses are reminiscent of the external zones of many kuroko-type VHMS deposits, marking the vanishing of the exhalative seafloor hydrothermal systems.

3.2.2. Gold setting

Gold is present in the barite lenses, with values up to 7.0 $g.t^{-1}$ (Ganaet) or even 8.0 $g.t^{-1}$ (Hamim), generally associated with a few silver (up to 12 $g.t^{-1}$), likely as electrum. Bulk analyses demonstrate that gold is concentrated in the thick barite-quartz layers, the iron-rich layers being practically barren. Yet, likely due to polishing problems, gold was rarely seen in thin sections from barite-quartz layers, as small xenomorphic grains of native gold at barite boundaries. Inversely, gold was readily observed in thin sections from the hematite-chlorite schists, as tiny (10-15 μm) grains of native gold, either associated with late-D3 microcracks, that are particularly well expressed in the magnetite porphyroclasts (Fig. 15-d, 16-e, f, and 17-e,f), or dispersed in chlorite cleavage, clearly post-dating D1 and D2 deformation (Fig. 15-d, e).

3.2.3. Synthesis

Gold concentration in massive barite-quartz layers is of difficult interpretation. On the one hand, it could point to an early (syngenetic) enrichment in the exhalative barite. It is known from present-day barite-rich polymetallic VMS on the sea-floor that gold is effectively concentrated in Ba-rich environments (e.g., Herzig et al. 1993). Alternately, barite deposition could simply be the corollary of the H_2S-oxidation process, which by itself leads to gold precipitation (Ihle et al. 2005), in particular in barite lenses capping the massive sulphides (Huston et al. 1992). Thermodynamic calculations (McClenaghan et al., 2009) suggest that barite and gold co-precipitation is a distinct possibility. The systematically late-D3 introduction of gold in the iron-rich layers could, in this case, be interpreted as a remobilisation halo. Early gold enrichment can be expected in the other exhalative levels, such as the iron-rich layers and Mn-rich layer topping the barite horizon, with remobilisation beginning with the metamorphic

episode. As such, a process is not observed, the inverse relationship may be suspected, i.e., that gold was introduced during D3 in the barite lenses, particularly the massive barite-quartz layers.

3.3. Gold-bearing quartz veins: the Kamoeb deposits

The Kamoeb deposits (Fig. 18) are the unique occurrence in the Ariab area of the quartz-gold lode-type, otherwise frequent in the Red Sea Hills (see Fig. 1). The Kamoeb deposits consist of a set of pre-kinematic (folded, boudinaged, and schistosed) quartz veins, 0.5 m to 5m thick, up to 3 km along strike (Fig. 18). Rocks mainly from the C unit host them, where they are mostly sub-concordant due to tectonic accordance. They are also present at the G1-C contacts, with high discordance, or even inside the G1 granitoids. Four veins display significant gold values (Fig. 18): KN (4.3 $g.t^{-1}$), KS1 and 2 (4 g.t-1), and KE (6 $g.t^{-1}$), but KN, with about 1 t gold, is the only significant reserve.

The vein system is associated with zoned alteration haloes, up to 10 m thick, consisting of proximal sericite (a Ba-phengite, up to 1.35 BaO wt.%)-pyrite ("bleaching") zone and a distal Fe-carbonate-chlorite assemblage.

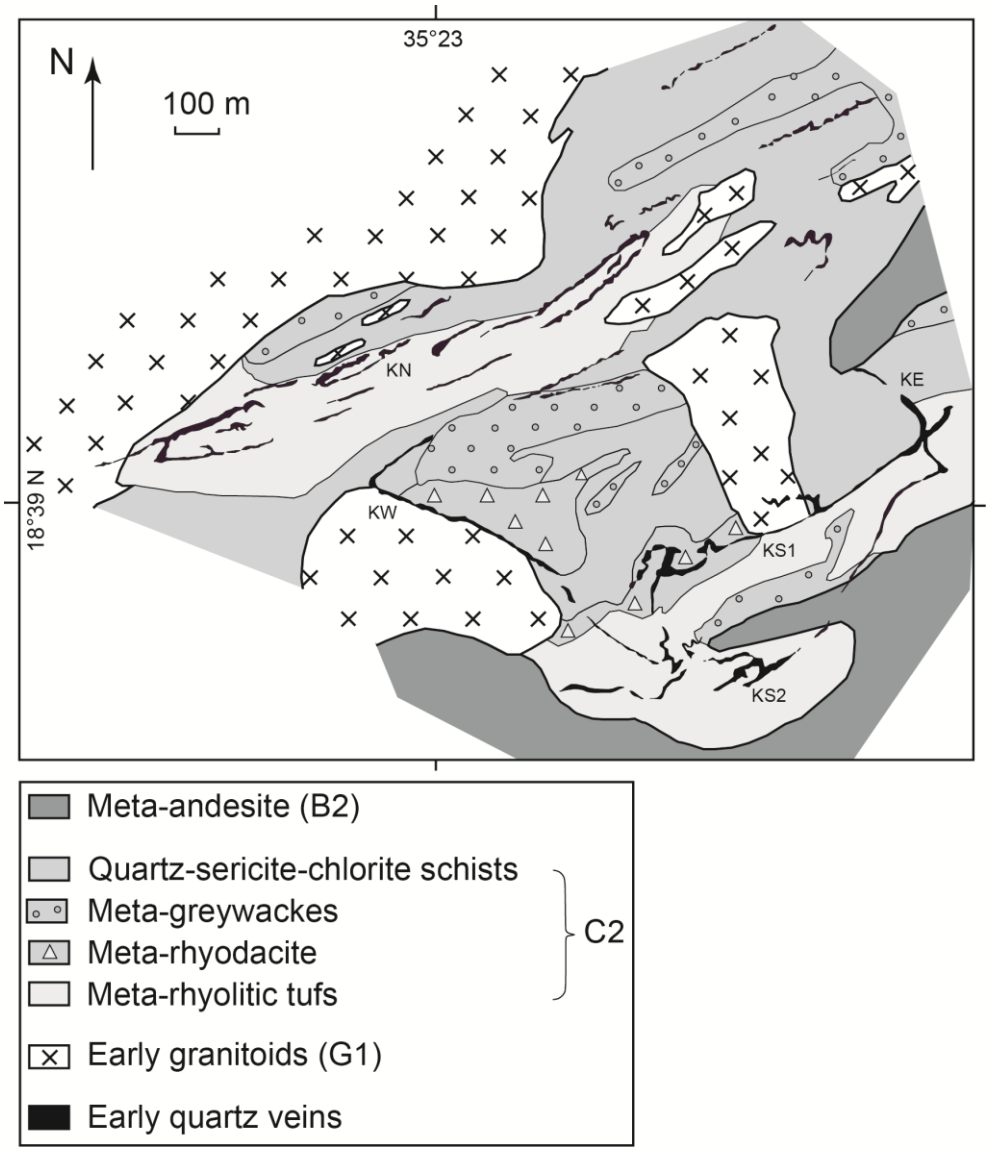

Figure 18. Geological map of the Kamoeb area, displaying the Kamoeb quartz vein setting (redrawn from Abu Fatima 2006, after Cortial et al., 1985). KE: Kamoeb east; KN: Kamoeb north; KS1, KS2: Kamoeb south, vein 1 and 2; KW: Kamoeb west.

3.3.1. Quartz microstructures

At the microscopic scale, all the Kamoeb quartz display ductile deformation microstructures testifying for D1 and D2 deformation stages, confirming that quartz deposition at Kamoeb was a pre-kinematic event. Minerals from the alteration haloes, being equally affected by the D1 and D2 events, were synchronous of quartz deposition.

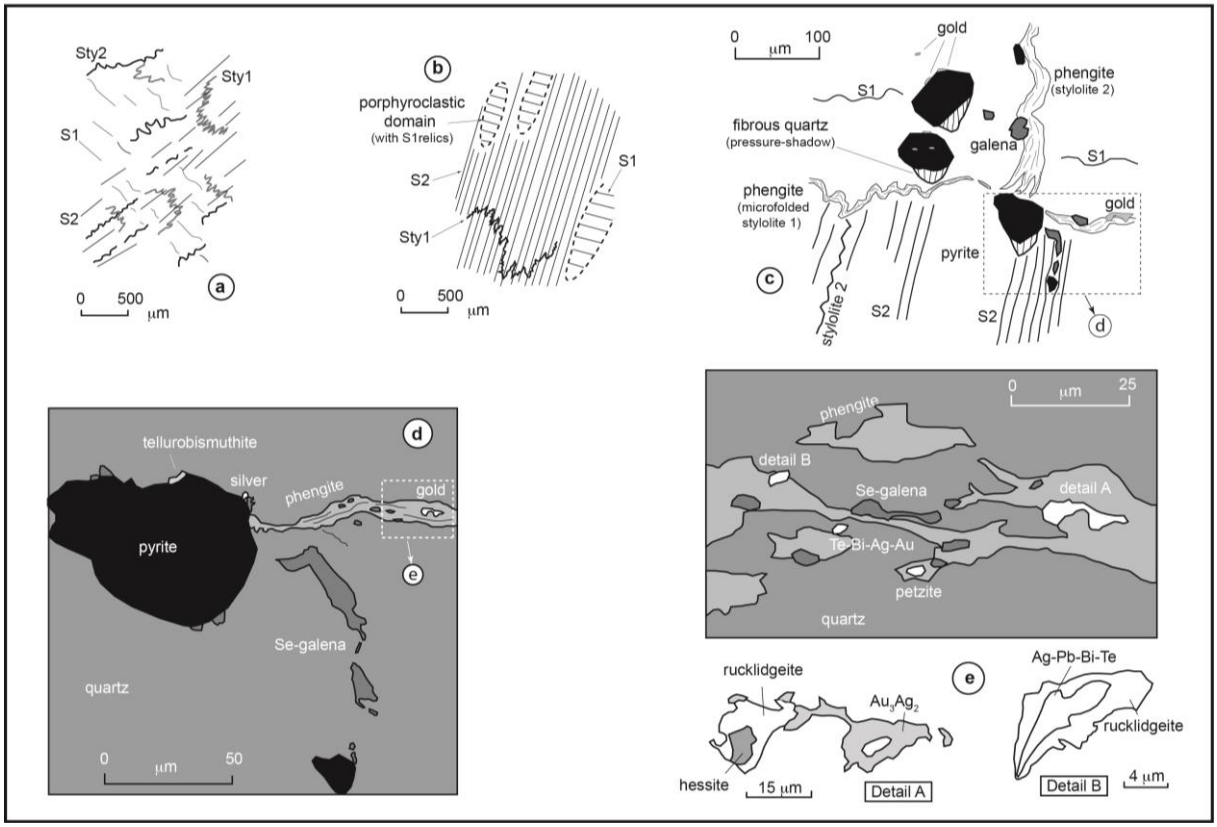

Figure 19. Microstructures in the deformed Kamoeb quartz and the gold and sulphides settings. **a**. Existence of two successive flattening surfaces (S1, S2) materialised by microcrystalline quartz, and the associated stylolites (Sty 1, Sty 2) expressed as either indented grain contacts or (more often) as Ba-phengite accumulations. Stylolites 1 are micro-folded with S2 as axial planes. Sample KAM 9209-3A. **b**. Schematic relationships in mylonitic quartz (Sample KAM 9309-123), with penetrative S2 and relicts of the pre-existing D1 microstructures, as S1 preserved within porphyroclastic domains and intensely microfolded stylolite 1. **c.** Sulphide setting in deformed quartz (Sample KAM9209-3C), with D1 relicts (mainly early phengite stylolite 1) and penetrative D2 features (S2, phengite stylolite 2). Pyrite is syn-kinematic for D2 (quartz pressure-shadows), whereas galena and gold overprint D2 features. **d**. Detail of c (redrawn from SEM-BSE imaging). **e**. Aspect of d (redrawn from SEM-BSE imaging).

The D1 and D2 events are expressed as two sets of more or less orthogonal planar features: (i) schistosities, marked by parallel bands of microcrystalline quartz (sometimes partly annealed), and (ii) stylolites, either as indented crystal boundaries or, more often, as accumulations of a Ba-phengite. Mutual relationships indicate that one set (S1, stylolite 1) is earlier than the other (S2, stylolite 2). In particular, early stylolites (Sty 1) are usually strongly microfolded with S2 as an axial plane (F2 microfolds) (Fig. 19-a to c).

Two other types of microstructures overprint the D1 and D2 features: (i) diffuse bands of recrystallised quartz with healed microcracks, still exhibiting a weak plastic deformation, and (ii) clear quartz veinlets corresponding to a macroscopic veining perceptible at the outcrop scale. These late features are interpreted as possible syn- to late- D3 events of hydrothermal circulation within the quartz veins.

3.3.2. Mineralization

Quartz veins host pyrite, galena, native gold and electrum, and several tellurides. The crystallization sequence of these minerals may be evaluated with the relative chronology of the above-described quartz microstructures (Fig. 14).

Pyrite is late-kinematic for D2 and occurs as sub-euhedral porphyroblasts (~ 100 □m in size) overprinting most D1 to D2 plastic deformation features, including stylolites 2. It still exhibits "pressure-shadows" textures with fibrous quartz, consistent with the D2 shortening direction (Fig. 19-c).

Galena (a selenium-rich variety, up to 7,000 ppm Se) as small anhedral crystals (~ 10 to 50 μm) is typically later, apparently following sealed (D3?) microcracks in the quartz and crosscutting pyrite. It is mainly found in close association with both generations of phengite stylolites (Fig. 19-c to e).

As tiny blebs a few μm in size, gold and tellurides are distinctly coeval and, such as galena, are late in the system. They are intimately associated with the phengite stylolites or the quartz-

pyrite boundaries (Fig. 19-c to e). Gold is present either as native gold or electrum (Au_3Ag_2) or gold-bearing tellurides. Based on SEM-EDS quantitative analyses, several tellurides were found, including calaverite ($AuTe_2$), petzite (Ag_3AuTe_2), hessite (Ag_2Te), and altaïte (PbTe), but also tellurobismuthite (Bi_2Te_3), rucklidgeite $(Bi, Pb)_3Te_4$ and volynskite ($AgBiTe_2$), without any preferential distribution.

3.3.3. Synthesis

From the preceding, main conclusions are as follows:

(i) The Kamoeb quartz vein systems are spatially associated with the G1 granitoids. They may be interpreted as peribatholitic quartz vein swarms reworked during the tectonic-thermal events affecting the Ariab area.

(ii) Gold, Te, Bi, Pb, and Se were introduced after the main D1-D2 events, likely at the late-kinematic D3 stage. Given the apparent absence of pre-kinematic gold-bearing association, it is difficult to envisage a hypothetical syn-quartz gold stock's late remobilisation.

(iii) As far as gold is considered, there is an evident parallel between the mineralization sequence at Kamoeb and in the VHMS (and barite) deposits. Gold is associated with Te, Bi, and Pb in the two types of deposits, and coeval galena is Se-enriched in both. These data reinforce the idea that gold was introduced during the late D3 stage in the Kamoeb quartz and emphasise the late introduction of silver in both types of deposits.

(iv) The dispersion and the variety of Au- and Ag-bearing minerals may be taken as evidence for a series of very local chemical equilibria, suggesting, in turn, low fluid-rock ratios at the time of gold deposition. The lack of gold-related quartz deposition also confirms it. Alternatively, the variety of Bi-Te minerals observed at Kamoeb could result from fractional crystallisation of a Bi-Te melt, and the gold enrichment is due to gold scavenging by this melt (Wagner 2007). Such melts do not exist, however, at low temperatures (< 300°C). The systematic association of the gold, tellurides, and galena within phengite stylolites suggests that

the latter acted as preferential fluid pathways. However, a kind of topochemical effect cannot be dismissed. The preferential association of gold- and Te-bearing minerals with the quartz-pyrite boundaries, on the other hand, is there strongly suggestive of a topochemical effect.

3.4. Gold mineralization close to the Nukasib shear zone: the Derbikwan showing

In the Derbikwan area, close to the Nukasib suture, swarms of poorly outcropping quartz veins hosted in carbonate-pyrite-rich mafic schists are spatially associated with a colluvial gold prospect. Although the quartz veins are barren, gold was worked in old times in discrete bodies (1-8m wide, 100-300 m long) striking parallel to the quartz veins on an overall distance of ~ 9 km. The deposit is at present poorly known, with only a few exploratory trenches dug at the time of our field study (2007). The following developments are a preliminary statement on the nature and origin of this type of gold occurrence in the Ariab area.

3.4.1 Quartz veins

Exploratory trenches favoured field observations of the quartz vein system. Conjugated flat-lying fault veins with sheared schists at both the footwall and the hanging wall are associated with sub-horizontal tension gashes (0.3 to 1 metre wide), consistent with the D3 shortening direction. Thus, the quartz vein array may be interpreted as an inverse fault splay associated with the D3 reactivation of the early (D1) Nukasib shear zone.

3.4.2 Carbonate-pyrite-rich mafic schists

Unfortunately, no sample from the close vicinity of the quartz veins could be studied. Yet, in one exploratory trench, the significant gold content was found in sheared pyrite-schists at the quartz footwall. The quartz-carbonate-chlorite-sericite-pyrite schists appear as pre-D1 altered mafic rocks. The large (mm-sized) pyrite cubes, as well as chlorite-quartz-epidote assemblages replacing an unknown mafic mineral (clinopyroxene?), are all pre-kinematic, with spectacular "pressure-shadows" (quartz + Fe-carbonate) recording both the D1 and the D2 events.

Interpretation: Although poorly constrained, the Derbikwan occurrence would appear as syn-D3 mineralization. Gold could have been conveyed through the quartz veins pathway and be trapped in the pyrite-rich surrounding schists. The noticeable absence of any sulphides inside the quartz veins would explain their barren character since no mineral trap such as pyrite could have favoured gold deposition in the quartz.

3.5. P-T conditions of gold deposition in the VHMS and Kamoeb deposits: a fluid inclusion study

Early quartz in either the VHMS or the Kamoeb deposits mainly contains decrepitated fluid inclusions (FI), with stellate or cuspate textures and peripheral clouds of tiny FI. Such features suggest implosion during the tectonic-thermal events, as it could have been expected (Marignac et al. 2003; Marignac and Cathelineau 2006). It is only in late undeformed quartz (inter D2-D3 $Q_{2\text{-}3}$ in the VHMS, and above all late-D3 Q_3 in both) that preserved FI may be studied. In the VHMS, these are often very small (< 5 μm) FI, only amenable to microthermometric measurements using x800 magnification. The Kamoeb quartz display, as a rule, larger FI of more comfortable study.

3.5.1 FI typology and petrography

The FI nomenclature follows Boiron et al. (1992). Briefly, the fluid inclusion terminology is based on their final homogenisation mode as either liquid (noted L) or vapour (noted V). According to their components' nature, indicated by a subscript, c for CO_2-dominated volatile species, w for water. For example, 3-phase FI at room temperature that finally homogenises in the liquid phase is noted as Lc-w. In contrast, those inclusions homogenising to the liquid that remain 2-phase even at low temperature, but displaying volatile species (more commonly as clathrates) are noted Lw-c. The volumetric fraction of the volatile phase (fvp) was estimated by

reference to the volumetric chart of Roedder (1979). FI assemblages correspond to fluid inclusions considered as following synchronous nomenclature of Bodnar (2003).

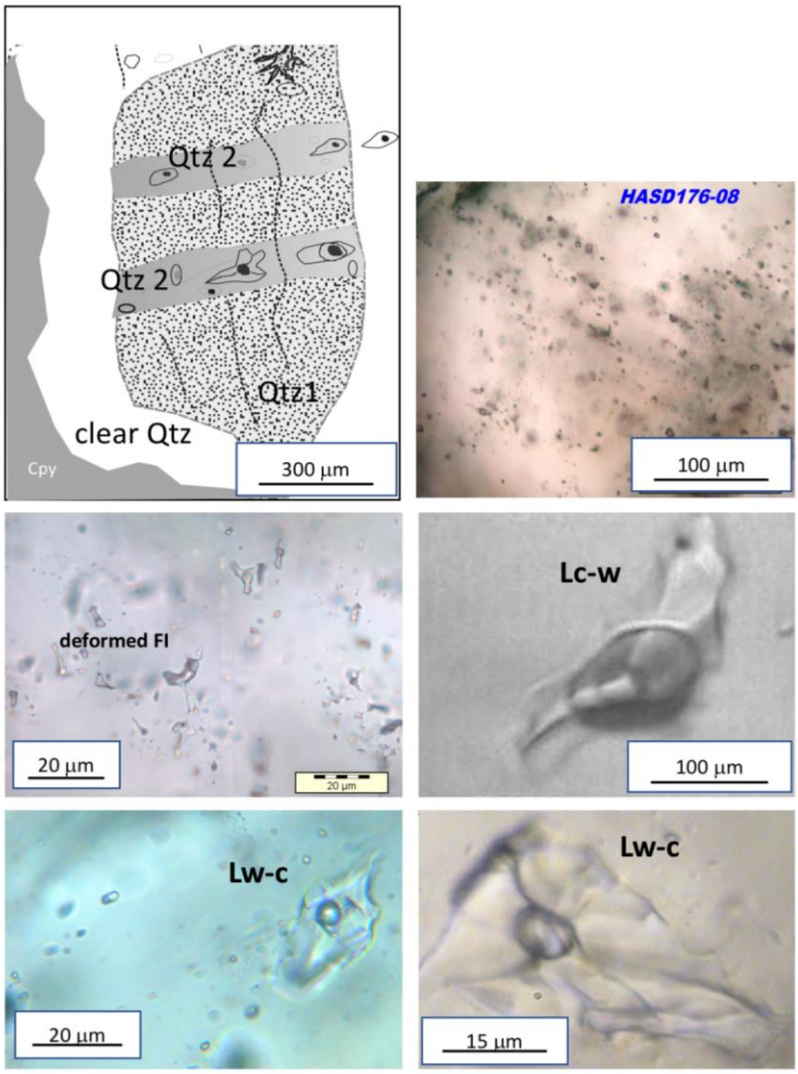

Fig. 20: Main types of fluid inclusions in quartz from Kamoeb and VHMS. a: quartz textures and simplified types of occurrences of fluid inclusions. b: microphotograph showing fluid inclusion FI assemblages in $Q_{2\text{-}3}$, c: deformed fluid inclusions in Q1, d: aqueous-carbonic three-phase Lc-w inclusion, e-f: Lw-c aqueous-carbonic two-phase fluid inclusions

The following types were observed in the present study (Fig. 20):

Lc-w FIA, mostly seen in the Kamoeb samples, have a large size (20-30 µm) and an fvp ranging between 0.6 and 0.9. They are also frequent in D2-3 quartz from the VHMS, where

most of them are 3-phase FI at room temperature. They are mainly present as isolated 3-D clusters (i.e., possibly primary, or at least, early), elongated as microdomain Q_{2-3} within Q_1.

Lw-c FIAs are absent in Kamoeb but present in Haddal Aouatib and Yonim. Lw-c FIs are 2-phases FI at room temperature and have a fvp ranging from 0.2 to 0.3. Based on a few intersecting relationships of difficult interpretation, they seem to post-date the Lc-w. They are mostly found as FIPs, and in the D3 VHMS quartz.

FI type	Tm CO_2 (°C)	Tm ice (°C)	Tm clat (°C)	Th CO_2 (°C) (L)	Th (°C)
Lc-w					
Kamoeb (n=66)	-58.3 to -56.8	-5.6 to -2.2	2.6 to 7.9	16.3 to 26.0	220 to 310
VHMS (n=118)	-59.7 to -57.2	-7.6 to -2.5	1.8 to 8.3	22.8 to 29.7	237 to 278
Lw-c					
VHMS (n=10)		-7.1 to -2.2	1.9 to 8.0		260 to 355

Table 2. Summary of the microthermometric measurements in the Kamoeb and VHMS (Yonim, Hadal Ouatib, and Hassai) quartz. Tm CO_2: melting temperature of the solid CO_2 Tm ice: final melting temperature of ice. Tm clat: final melting temperature of clathrates. Th CO_2: homogenisation temperature of the volatile phase. Th: bulk homogenisation temperature. L: homogenisation in the liquid phase, respectively.

3.5.2. Microthermometry and Raman results

A summary of the microthermometric results is given in Table 2. In the Lc-w FI, melting temperatures of CO_2 range from -59.7° to to 56.8°C. They are thus lower than for pure CO_2 (-56.6°C), indicating the presence of other volatiles. Raman microanalysis (Table 3) confirms the presence of small amounts of N_2, and the significant absence of a methane component. Th CO_2 ranges from 16 to 30 °C in the liquid phase.. Tm ice is ranging from -7.6 to -2.2°C and Tm clat

is observed between 1.8 and 8.3 °C. Bulk homogenisation occurs on a wide range of temperatures, mostly between 220° and 310°C.

In Lw-c FI, Tm clat attesting the presence of gas species is ranging from 1.9 to 8.0°C. Tm ice is measured between -7.1 to -2.2°C. Bulk homogenization occurs between 260 and 355°C.

The nitrogen concentration, mainly in the range 10 to 35 mol.% in the Lw-c FI, is higher than in the Lc-w FI. (1 to 6 mol.%).

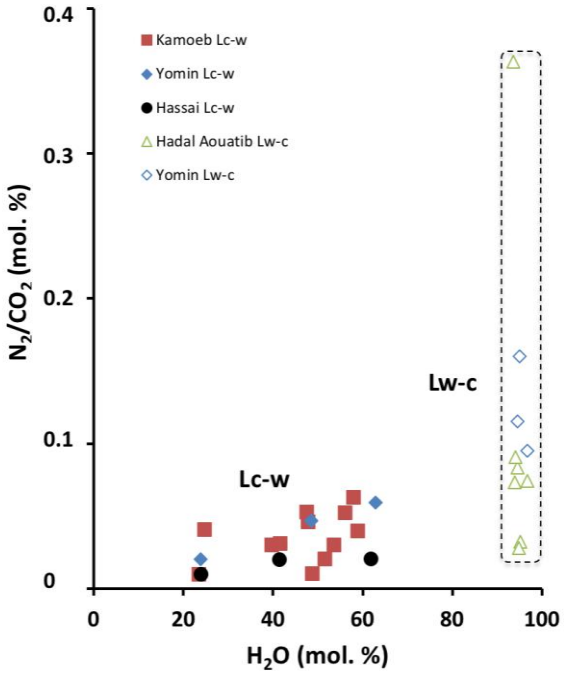

Figure 21. Calculated bulk compositions (in molar fractions) of representative FI s from the quartz at Kamoeb and several VHMS (Yonim, Haddal Aouatib, Hassai) in an N_2/CO_2-H_2O diagram.

3.5.3. Bulk compositions

Calculated bulk compositions (Table 3) are reported in the N_2/CO_2versus H_2O diagram (Fig. 21). The same volatile-rich fluids (Lc-w) are present in both the Kamoeb and the VHMS quartz. In WHMS quartz, a second fluid stage is recorded as Lw-c FIs which are characterised by (i) a water content higher than 94 mol.%, (ii) an increase of the N_2 /CO_2 ratio compared to Lc-w FI,

N_2 being always a minor component, the volatile fraction remaining CO_2-dominated, with no contribution of any CH_4 component.

	Microthermometry (°C)					Raman data (mol.%)			Bulk composition (mol. %)			
	Tm CO_2	Tm ice	Tm clat	Th CO_2 (L)	Th	fvp (%)	ZCO_2	ZN_2	XH_2O	XCO_2	XN2	XNaCl
Lc-w												
Kamoeb												
KAME02-11	-57.1	-4.2	7.6	23.2	241.5	75	97.0	3.0	48.8	49.3	0.5	1.4
KAME02-12	-57.3	-4.3	3.3	20.1	248.3	65	95.0	5.0	56.2	38.5	2.0	3.3
KAME02-13	-57.0	-5.3	2.6	23.6	234.1	70	98.0	2.0	51.7	44.3	0.9	3.1
KAME02-14	-58.1	-2.2	4.8	21.8	190*	80	97.0	3.0	39.7	56.8	1.7	1.8
KAME02-16	-57.1	-3.4	7.1	26.0	240.3	80	98.0	2.0	41.7	54.8	1.7	1.8
KAME02-18	-57.0	-3.0	7.1	23.6	235.7	90	96.0	4.0	24.7	71.6	2.9	0.8
KAME02-110	-57.2	-4.1	6.3	22.6	220.5	90	99.0	1.0	23.5	74.9	0.7	0.9
KAME02-111	-57.0	-5.1	7.2	20.6	241.3	75	95.5	4.5	47.9	48.3	2.2	1.6
KAME02-114	-57.8	-4.2	4.5	22.2	240.4	65	94.0	6.0	58.0	36.7	2.3	3.0
KAME02-23	-57.2	-5.6	7.5	19.8	310.1	65	96.0	4.0	58.9	37.8	1.5	1.8
KAME02-25	-57.0	-4.4	5.5	22.2	287.6	75	95.0	5.0	47.6	47.8	2.5	2.1
KAME02-26	-56.8	-3.1	7.9	22.1	281.9	70	97.0	3.0	53.6	43.7	1.3	1.4
Yonim												
YONM-202-N81	-56.9	-2.5	4.3	25.4	237.1	90	98.0	2.0	23.9	73.5	1.5	1.1
YONM-202-N82	-57.2	-4.7	6.4	25.4	230.3	70	96.5	3.5	48.5	47.3	2.2	2.0
YONM-202-N83	-57.2	-5.5	5.8	25.4	243.2	75	95.5	4.5	48.5	47.3	2.2	2.0
YONM-202-N84	-58.3		4.4	23.6	246.2	60	94.0	6.0	62.8	32.0	1.9	3.3
Hassai												
HASD176-081	-57.3	-3.6	4.2	23.3	239.5	60	98.0	2.0	62.0	34.3	0.7	3.0
HASD176-084	-56.8		7.7	22.8	245.3	90	99.0	1.0	24.0	74.7	0.7	0.6
HASD176-088	-57.3	-2.7	7.6	29.7	277.7	80	98.0	2.0	41.5	55.4	1.1	2.0
Lw-c												
Hadal Ouatib												
HDND77-111		-5.1	4.2		285*	30	89.0	11.0	95.2	3.1	0.1	1.6
HDND77-112		-5.0	8.0		341.9	20	89.5	10.5	94.9	3.6	0.1	1.4
HDND77-113		-5.6	7.6		260.5	30	86.0	14.0	94.0	4.1	0.3	1.6
HDND77-114		-5.1	6.5		354.7	30	83.0	17.0	94.6	3.6	0.3	1.5
HDND77-117		-2.3	4.3		275.7	30	84.5	15.5	96.7	2.7	0.2	0.4
HDND77-118		-7.1	6.3		278.3	20	80.0	20.0	94.1	3.3	0.3	2.3
HDND77-119		-2.2	6.6		345.9	20	50.0	50.0	93.7	3.3	1.2	1.8
Yonim												
YONM 202-N2-1	-56.8	-7.1			250 *	30	65.0	35.0	95.1	2.5	0.4	2.0
YONM 202-N2-2	-56.6	-3.6	1.9		240 *	35	71.5	28.5	94.6	2.6	0.3	2.5
YONM 202-N2-3	-56.6		1.7		220*	25	70.5	29.5	96.7	2.1	0.2	1.0

Table 3. Bulk compositions from Raman microanalysis of selected FI of both the Kamoeb and the VHMS (Yonim, Haddal Aouatib, and Hassai) quartz. Tm CO_2: melting temperature of the solid "CO_2". Tm ice: final melting temperature of ice. Tm clat: final melting temperature of clathrates. Th CO_2(L): homogenisation temperature of the volatile phase in the liquid state. Th: bulk homogenisation temperature, *: decrepitated under heating.

3.5.4. P-T-t evolution

Isochores were calculated for a set of FI of known bulk compositions, and are drawn in Fig. 22. They record a pressure drop from two series of Lc-w, and then the Lw-c trapping conditions with two sets of isochores.

The absence of biotite in the regional package of minerals means that regional temperature was never higher than ca. 420°C at ca. 350 MPa (e.g., Yardley 1989). More precise temperature and pressure estimations may be achieved using the Si-in-Muscovite geo-barometer of Massonne and Schreyer (1987) (assuming that Ba substitution to K does not significantly alter the equilibrium) and the Al-in-Chlorite geothermometer of Cathelineau (1988). The latter is known to yield relevant results, given that the chlorite grew in an Al-saturated medium, and no interlayered chlorite-other phyllite phase is used (Frimmel 1997, in Gartz and Frimmel 1999), two conditions respected in the present study. However, the problem is to find the relevant compositions, since the Ariab-Arbaat belt experienced a multistage thermal history, starting from the hydrothermal stage of metamorphism.

An electron microprobe survey of chlorite and phengite compositions in the belt revealed a clear bi-modal distribution of Al_{iv} p.f.u (in chlorite) or Si p.f.u (in phengite), with Al_{iv}-in-chlorite usually comprised between either 1.60 and 1.36 (most of them around 1.45) or 1.26 and 1.21 (with exceptional values as low as 1.07), and Si-in-phengite clustering either between 3.19 and 3.24 (up to 3.30) or 3.11 and 3.15 (exceptionally as low as 3.07). Two observations allow an interpretation of these distributions. First, kinked syn-S1 or syn-S2 phengites (i.e., likely un-recrystallized phengites having escaped later re-equilibration) display Si p.f.u. typical of the high-pressure range of compositions, whereas late overgrowths on early phengites yield Si p.f.u. in the lower (low P) range of compositions. Second, in a Barut sample, an early quartz-chlorite-phengite hydrothermal association preserved in an undeformed vug provided the higher Al_{iv}-in-chlorite found in our survey. In contrast, a late (possibly, syn-D3) chlorite

overprinting fibrous syn-kinematic D2 quartz yielded Al_{iv} = 1.26, in the low (low-T) range of compositions. The highest temperatures recorded by the Al-in-chlorite geo-thermometer of Cathelineau (1988) and the highest pressures recorded by the Si-in-phengite geo-barometer of Massonne and Schreyer (1987) provide a maximal P-T estimate. The latter is likely those of the first tectonic-metamorphic events (D1 and D2). The lowest values record more or less overprinting during a second thermal event, during D3 or later. When reported in the P-T diagram in Fig. 22, the two P-T pairs appear to be entirely consistent with the isochore sets, allowing the construction of a P-T-t path, shown in Fig. 20, characterised by a sub-isothermal pressure decrease from lithostatic to hydrostatic pressures. The isochores of a few FI from Haddal Ouatib are shifted to lower temperatures. However, it is difficult to know if they are trapped under litho, infra-litho or hydrostatic pressures.

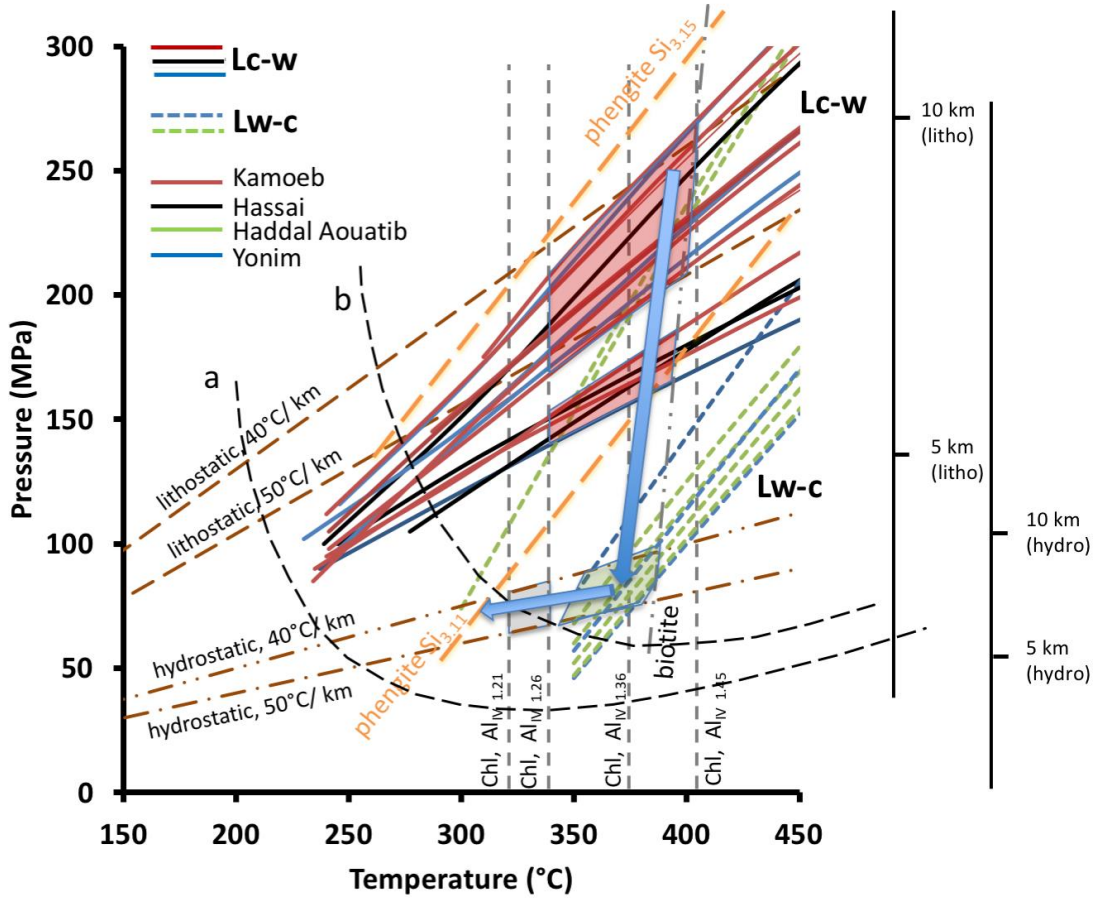

Figure 22. Reconstruction of the late (D3?) P-T-t evolution as recorded by fluid inclusion densities (isochores) from three representative areas (Yonim and Haddad Aouatib VHMS; Kamoeb quartz veins). The biotite-in isograd is from Yardley (1989, Fig. 3-11, p. 86). The Si-in-phengite geo-barometer isopleths (Massonne and Schreyer, 1987) and the Al-in-chlorite geo-thermometer isopleths (Cathelineau, 1988) have been drawn for relevant compositions. Isopleths (dotted dark blue lines) in the system H2O-CO2-NaCl are from Weisbrod (1984) for a salinity of 6 wt. % NaCl equiv., and a CO2 content of 10 (a) and 20 (b) mole%. See text for explanation.

The scenario for gold-related fluid circulation in the Ariab area implies the participation of two types of fluids. First, circulation of hot (350-400°C) volatile-rich fluids at around 260-200 MPa (10 to 8 km depth if lithostatic). Second, the water-dominated fluids (Lw-c FI), enriched in N_2 occur after a pressure drop from c. 200 MPa to c. 100 MPa at sub-constant temperatures (380-350°C), This late-stage may correspond to the stage of Bi-Te melts, as discussed in the preceding section.

This evolution finds similarities with the Late Carboniferous gold-forming fluid evolution reconstructed in the West Variscan belt (Boiron et al. .1996, 2001, 2003, Vallance et al., 2003) and the Limousin area (in the French Massif Central) in particular (Boiron et al. 1990; Essarraj et al. 2001; Vallance et al., 2004). A similar evolution was also reconstructed for the late-metamorphic (Visean) gold introduction in the VHMS deposits of the Iberian Pyrite Belt (Marignac et al., 2003, Marignac et Cathelineau, 2006). In the West Variscan Belt, the early gold introduction is interpreted to be deposited by similar late aqueous-carbonic fluids. The mixing with a "cold" low-salinity fluid is by contrast not recorded at Ariab. Both in Variscan terranes, Lc-w, and Lw-c fluids are likely to be of "metamorphic" origin, i.e., equilibrated with

metamorphic rocks (Boiron et al., 2003). In contrast, the latest water dominated fluids would record the progressive incoming of more surficial fluids evolving during their infiltration.

3.6 Supergene gold enrichment in the VHMS and barite deposits: gossans and SBR deposits

More than 20 gold-bearing gossans derived from the oxidation of the VHMS deposits, with the formation of silica-barite-rich rocks (SBR) hosting gold (and silver) concentrations, were discovered in the Ariab-Arbaat area (Cottard et al. 1986a), with a cumulative tonnage of 68 t gold averaging 9.7 $g.t^{-1}$ (from 4.2 to 17.1 $g.t^{-1}$) (Abu Fatima 2006). The main deposits are Hadab Ouatib W (16.2 t gold at 15.1 $g.t^{-1}$), Oderuk N (7 t gold at 5.0 $g.t^{-1}$), and Hademayet-Wali N (6.7 t gold at 6.2 $g.t^{-1}$).

The mineralised gossans are part of the regional weathering developed in the Red Sea Hills (Cottard et al. 1993). Usually present on a depth no more than 10-20 m, this alteration was enhanced by the intense deformation affecting the VHMS host-rocks and the sulphides' strong reactivity (mainly, the pyrite) themselves. As a consequence, extensive weathering at the origin of mineralized gossans could penetrate down to 90-100 m depth, being best developed onto tectonically verticalised VHMS bodies.

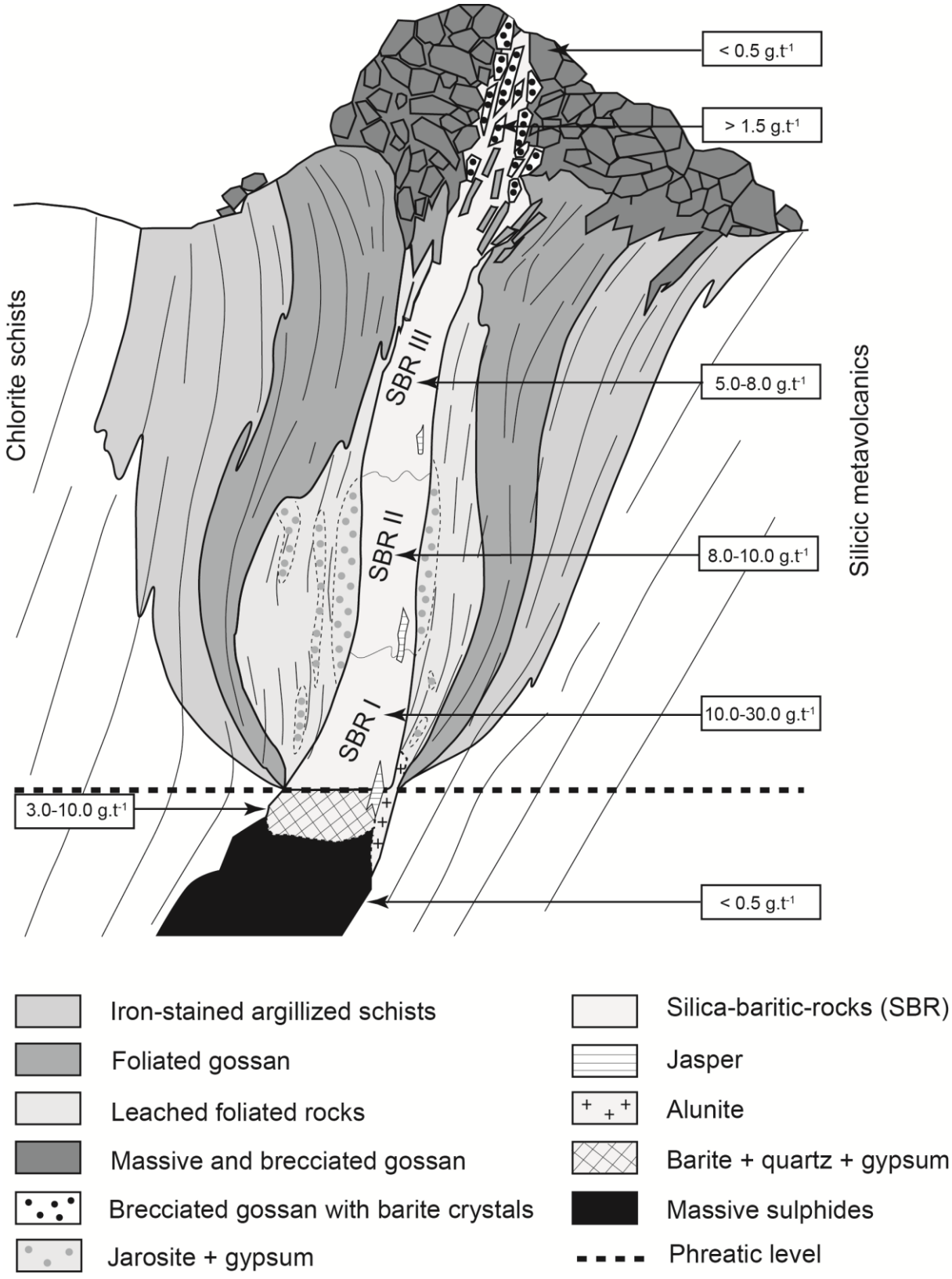

Figure 23 Cross-section model of a typical Au-bearing gossan developed at the expense of a VHMS deposit from the Red Sea Hills (redrawn from Abu Fatima 2006, after Recoché 1989).

The gold-bearing gossans structure (in Fig. 23) is mainly based on the results from Hottin and Laforet (1986), and Recoché (1989). The different weathering facies form broadly concentric envelopes, with from outside towards the inside (i) iron-stained clays (mostly kaolinite) and iron-oxide impregnation of the schistose host rocks ("foliated gossan"), (ii) leached (bleached) schistose host rocks, with patches of jarosite-rich facies, and (iii) the core of silica-barite rocks (SBR), that concentrate gold. The jarosite-rich rocks are mainly present as a 5-20 m thick halo surrounding the SBR in the lower part of the profile. Jarosite is the main component associated with gypsum, alunite, and Fe- and Cu-sulphates. The SBR is a heterogeneous silica-rich micro-brecciated rock, with chalcedonic or microcrystalline clastic quartz and a variable matrix always including barite, the nature of which defines three successive facies from bottom to top: (i) white sugary barite-rich SBR I, highly siliceous (amorphous silica and chalcedony) and containing the highest gold grades, (ii) yellowish-green SBR II, jarosite-rich, and (iii) reddish ferruginous SBR III, formed of micro-brecciated microcrystalline quartz and a matrix of goethite-hematite and barite (up to 15-20% in volume).

The base of the SBR defines a redox boundary, with complete leaching of the underlying sulphides, pyrite being currently transformed into jarosite, and transformation of the phyllites into silica. The underlying VHMS exhibits a cementation zone's typical mineralogy, with covellite, digenite, and bornite replacing primary copper minerals, anglesite formed after from galena, and barite from the dissolved Ba-phengites. Pyrite is partly dissolved, and sphalerite, tennantite, and tellurides are absent. The surrounding rocks, where phyllites are replaced by microcrystalline silica, are characterized by the association alunite-oxidised copper minerals (native copper, tenorite, and the rare delafossite $CuFeO_2$). Gold id often concentrated in the SBR as "invisible" gold, i.e., tiny gold particles (4-20 μm). It is associated with Ag, Pb, Ba, As (up to 1240 ppm), Te (up to 43 ppm), Se and Sb, whereas the mobile elements (Zn, Cu, Mg, Al, Ca) are leached, being trapped in the jarosite- or alunite-rich haloes.

At the surface, the three zones defining the oxidised body are prolonged into massive (the zones i and ii) and brecciated (the SBR III) gossans. Goethite and hematite are the main minerals of the massive gossan. Brecciated gossan is a collapsed facies of the massive gossan, with a barite matrix.

According to Recoché (1989), the mineralised gossan-SBR bodies of the Ariab-Arbaat belt result from a multi-stage weathering history, recording the climate fluctuations of the Late Cenozoic in the Arabian-Nubian Shield area. The upper part of the oxidised profile is interpreted as the bottom remnant of an older profile, developed under the Late Pliocene-Early Pleistocene's hot and wet conditions (1.1 Ma). The still-active lower part (with the VHMS-BSR boundary coinciding with the present-day phreatic level in Fig. 23) records the more arid conditions from the Quaternary until now. The collapse in the upper levels (brecciated gossan) results from the substantial volume diminution corresponding to sulphide dissolution.

4. DISCUSSION AND CONCLUSIONS

4.1 Base metals in an intra-oceanic arc, gold in an accreted terrane

in the Ariab-Arbaat belt of the Haya terrane, the main BM and gold mineralising events' geodynamic settings are quite different.

The BM-hosting VHMS have formed at ca. 900 Ma in an intra-oceanic arc setting, and may, therefore, be classified as Cu-Zn deposits of the Uralian type (Prokin and Buslaev 1999) – the "bi-modal mafic setting" class of Franklin et al. (2005). Although massive sulphides are present at different levels in the lithologic pile, most VHMS of the Ariab-Arbaat belt are located in the same felsic unit (C2), at the top of a thick andesite-dominated pile. The VHMS are associated with barite-hematite-chert lenses that are their lateral equivalent, and a wrapping exhalative horizon appears to close the hydrothermal process. Intense subsequent deformation precludes

a precise identification of the local tectonic environment of the VHMS. Still, the abundance of felsic domes in the C2 unit and the existence of a plutonic complex of similar geochemistry (G1), at depth, is suggestive of a caldera environment, as is indeed the case for many polymetallic VHMS of the Uralian or the similar Abitibi-Noranda class (Herrington et al. 2005, Franklin et al. 2005).

By contrast, all the primary gold occurrences of the Ariab-Arbaat belt, whatever their style (VHMS-, quartz lode- or shear-zone-hosted), appear to have been syn-to late-D3, i.e., formed in a mature continental arc, already accreted to the northern Gebeit terrane, in the context of the final Pan-African collision leading to the Arabian-Nubian Shield (poorly constrained at ca. 620-ca. 560 Ma). Gold deposition occurred at the final stage of the collision, in a thickened crust suffering rapid uplift (from ca. 17 km to ca. 7.5 km) and intense fluid circulation, mixing deep hot (~ 350°C) "metamorphic" and shallow cold (< 300°C) "meteoric" fluids.

4.2 **Gold (re)-mobilisation or gold-(re)introduction*?***

By contrast with recent sea-floor deposits, gold concentration in fossil metamorphosed polymetallic VHMS ores is often described as native gold or electrum deposited in late syn- to post-metamorphic tectonic traps. The latter are usually sets of micro-cracks crosscutting earlier pyrite or arsenopyrite. There, gold is commonly associated with either galena, bismuth tellurides, or both, whatever the deposit's age. Recently described examples are in the Archean (Hongtoushan, China: Gu et al. 2005), the Paleoproterozoic (Boliden, Sweden: Walter et al. 2007) or the Phanerozoic (Urals: Vikentyev 2005; New Brunswick: Thome et al. 2007; Iberian Pyrite Belt: Marignac et al. 2003).

The most probable host of the early gold pre-concentration is usually considered to be the early pyrite. In such a model, the tectonic-thermal events only act to free and upgrade earlier "invisible" gold incorporated in the hydrothermal sulphides from the VHMS (e.g., Huston et

al. 1992). Modern polymetallic VHMS from the SW Pacific, with a mean gold content of 3.7 $g.t^{-1}$ (Herzig et al. 1993), are gold-enriched by comparison with most fossil equivalents. Gold concentrations range between 0.6 and 1.4 $g.t^{-1}$ for all types (Franklin et al. 2005) as, the 0.6 to 1.7 $g.t^{-1}$ range in the New Brunswick district, with a mean of 0.66 $g.t^{-1}$ (Thome et al. 2007, McClenaghan et al. 2009) or the 0.6 to 1.2 $g.t^{-1}$ range of the present study. Yet, according to Herzig et al. (1993), the most promising geodynamic environments for gold enrichment in VHMS are immature back-arcs or arcs, a setting fitting well with the Ariab-Arbaat occurrences. At our knowledge, there are only very few studies addressing the actual gold content of early hydrothermal phases in the VHMS and monitoring gold behaviour during the subsequent events. In the Archean Mobrun deposit, Larocque et al. (1993) report ion microprobe data on primary (syngenetic) and secondary (metamorphic recrystallization). They show that the secondary pyrites are systematically depleted to a 60% reduction of the initial content than the first pyrite, which contains 0.4 to 10 ppm "invisible" gold as micro-inclusions < 0.2 □m. In the Paleoproterozoic Boliden deposits (Skellefte belt), Walter et al. (2007), using the LA-ICP-MS technique, clearly demonstrated the early presence of sulphide-hosted gold and its strong remobilisation/exportation in syn-metamorphic veins. Yet, these deposits are exceptionally arsenopyrite-rich, and it is indeed early arsenopyrite that appears to be the main gold repository, the dominant early pyrite being poor in gold (< 0.2 ppm). In the Tharsis deposit (Iberian Pyrite Belt of Tournaisian age), Conde et al. (2009), equally using the LA-ICP-MS technique, found gold and correlated arsenic contents up to 8 ppm in the early framboidal or colloform pyrites. In contrast, syn-kinematically recrystallised euhedral pyrites are strongly depleted. However, in the same deposit, a detailed study of gold relationships with (micro)tectonic events could not find any evidence for a syn-kinematic gold deposition, as all visible native gold was deposited in late-kinematic features and associated with late- to post-metamorphic fluids (Marignac et al. 2003). In the Bathurst N°12 deposit (New Brunswick), McClenaghan et al. (2009) document

"invisible gold" mainly located in pyrite and arsenopyrite. Pyrite exhibits relict cores that concentrate gold (up to 21 ppm, with a mean of 2.7 ppm), whereas syn-metamorphic overgrowths are systematically depleted (down to 0.02 ppm, with a mean of 1.9 ppm). Arsenopyrite, a syn-metamorphic phase overprinting the pyrite, is equally poorer in gold, with a 1 ppm mean, and often relatively lower values, and is always " (...) depleted in gold relative to relict inclusions of pyrite" (p. 545). Whereas McCleneghan et al. (2009) think that at Bathurst N°12 "(...) redistribution of gold was limited"(p. 552) during the metamorphism, there is room to estimate, from their data, that indeed gold was extracted from the VHMS. At least, late metamorphic up-grading is excluded in that case.

Thus, two arguments favour gold export during the recrystallisation of massive sulphides during metamorphic events; i) the limited evidence for strictly syn-metamorphic gold remobilisation, and ii) the mere fact of the fossil VHMS deposits are relatively gold-poor when compared with their modern equivalents. The observed gold concentrations in late brittle structures within the same VHMS bodies (and notably in their quartz-rich feeder stockworks, that are prone to late fracturing and fluid circulation) may then be taken as a particular occurrence of the orogenic class of gold deposits. Thus, they are the result of gold re-introduction by late orogenic fluids and trapping on the pre-existing sulphides (pyrite, arsenopyrite) that are universally known to be efficient topochemical traps for gold. Detailed observations at Tharsis in the Iberian Pyrite Belt (Marignac et al. 2003) and the VHMS of the Ariab-Arbaat belt (this study) are good examples of this process.

4.3 An integrated model for gold in the Red Sea Hills?

The late-D3 gold event in the Ariab-Arbaat belt has all the makings of an orogenic gold system, being in particular very similar to the Late Carboniferous gold event in the West European Variscan belt. The existence of a crustal-scale hydrothermal system may, therefore, be inferred. Gold deposits and showings at the scale of the whole Red Sea Hills area (Fig. 1), either cluster

around the main D3 shear zones (notably, Oko and Hamisana SZ) or are dispersed in specific terranes (Gabgaba, Haya).

It is thus possible to propose that, at the very end of the Pan-African collision event (poorly constrained at ca. 560 Ma), fluids released from the root of the newly formed terrane (the Red Sea Hills area) were channelled towards the upper crust through the major D3 shear zones. Then, outpouring from these major drains, they conveyed through fault plays and damaged zones up to specific chemical traps. The latter are either the micro-fractured massive sulphide ore bodies or mineral and structural trap such as the Kamoeb quartz veins systems. In this scheme, occurrences such as the Debikwan prospect testify the fluid transfer reality through secondary tectonic features.

Therefore, the Ariab-Arbaat gold district would be classified as a representative of the shear-zone related orogenic gold deposits class (Groves et al. 2005 and references therein).

The source of the gold remains speculative. Yet, it may be observed that the high gold endowment of the Arabian-Nubian Shield is correlated with the abundance of ophiolitic sutures, making the shield to be " a massive graveyard of Neoproterozoic oceanic lithosphere" (Stern et al. 2004). Thus the mafic-ultramafic rocks could have been a source for the gold, and Stern et al. (2004) have drawn attention to the pervasive alteration of the harzburgites (serpentinisation, carbonatation, often considered as "post-obduction"), that could have mobilised gold. In this connection, the role plaid by the reactivated D1 sutures (such as the Nakasib in the Haya terrane) in locating some gold clusters (Fig. 1) could be significant.

4.4 The Ariab gold deposits in the ANS context

In recent years, the orogenic gold deposits from the Eastern Desert terranes were thoroughly investigated (Harraz 2000; El Tokhi and El Muslem 2002; Zoheir 2008a, b; Zoheir et al. 2008a, b; Zoheir and Akawy 2010; Zoheir and Moritz 2014; Boskabadi et al. 2017; Cheng et al. 2017;

Abd El Monsef et al. 2018; Talmer et al. 2018; Zoheir et al. 2018, 2019b; Perret et al. 2020). Most of the deposits are associated with the Najd fault system's second and third-order plays (Zoheir et al. 2019a). Based on a few direct c. 600 Ma Ar/Ar or Re/Os ages (Zoheir et al. 2019a and references therein), or the observation that the gold lodes are often observed to overprint the late alkalic granite plutons (e.g., Harraz 2000, Zoheir 2008b, Zoheir et al. 2008a), the gold deposition could be related to the late activity of the Najd system during the ductile to brittle transition. The gold lodes are typically syn- to late-kinematic quartz-carbonate-sulfide veins hosted in the shear-zones, with bleached alteration zones (quartz-sericite-carbonates-pyrite). The dominant fluids in the quartz lodes are described as volatile-rich (CO_2-CH_4-N_2) with variable salinity, from low (0.3-3 wt % eq NaCl) to moderate (4-8 w% eq NaCl) salinity (exceptionally reaching 17-20 wt % eq NaCl in a few deposits). Similar conclusions are proposed for the Hamadi deposit for initial "homogeneous aqueous-carbonic mixture" are inferred to form during retrogress metamorphism (Cheng et al., 2016). Gold is thought to have been deposited from these fluids, at temperatures and pressures variably estimated between 225° to 380°C, and 35 to 260 MPa, a pressure drop (possibly associated with fluid unmixing) being often considered to have been the key factor in gold deposition (Abu-Alam et al., 2019, Cheng et al., 2016). Concerning the origin of ore-forming fluids, Talmer et al. (2018) assert that "gold-bearing fluids were generated due to the metamorphic devolatilization processes along with the greenschist-amphibolite-facies transition of ophiolite and metasedimentary source rocks". In contrast, Boskabadi et al. (2017) proposed that "carbonation of ANS ophiolitic rocks due to the influx of mantle-derived CO_2-bearing fluids caused the breakdown of Au-bearing minerals such as pentlandite, releasing Au and S to the hydrothermal fluids that later formed the Au-deposits".

All these results converge so that the Neoproterozoic gold deposits in the ANS are considered as representatives of the mesothermal class (Zoheir et al. 2019a). Our findings in the Ariab belt

fit rather well with these results, with however significant differences. In the Ariab belt, gold is demonstrated to have been deposited late in the tectono-thermal history, clearly at the end of the exhumation. The late-D3 gold event in the Ariab belt has all the makings of an orogenic gold system, notably similar to the Late Carboniferous gold event in the West European Variscan belt (Boiron et al., 2003).

Does this mean that the Ariab deposits were formed under exceptional conditions not encountered elsewhere in the ANS? A careful reading of the published works shows that it is not the case and that, to the contrary, the Ariab style of evolution must be considered the rule for all ANS. The crucial point is that the workers take the tight association of gold with either arsenopyrite or As-rich pyrite as evidence that gold was coevally deposited with these sulphides. Consequently, the studied fluid inclusions (FI), mainly representative of the quartz-pyrite or quartz-arsenopyrite association in the mineralised veins, are currently considered representative of gold deposition stage. The main cited evidence for coeval gold and sulphide deposition is that gold is often found as inclusions in As-pyrite or arsenopyrite. Yet, when looked carefully at, gold inclusions in the sulphides are later. What is more, in all the published occurrences, gold, alone, or in rare cases, associated to galena and or tellurides, is also found in microcracks in either quartz or pyrite or arsenopyrite. Therefore, it may be concluded that in the other ANS gold deposits, gold was, as at Ariab, introduced later than pyrite or arsenopyrite and that, consequently, the studied FI in these deposits cannot be representative of gold deposition.

It is thus possible to propose that, at the very end of the collision events, fluids released from the root of the newly formed terrane (Boskabadi et al., 2017; Talmer et al., 2018), were channelled towards the upper crust through the major D3 shear zones such as the Najd system in the northern terranes, and the Oko shear zone for the Ariab belt. The fluids outpouring from

these major drains were then conveyed through fault plays and damaged zones, up to specific chemical traps like massive sulphide ore bodies or quartz veins systems.

5. Conclusions

- The existence of a crustal-scale hydrothermal system is linked to a late-D3 event in the Ariab-Arbaat belt. Thus, at the end of the Pan-African collision event, fluids released from the root of the newly formed terrane, the Red Sea Hills area, were channelled towards the upper crust through the major D3 shear zones. Then, the outpouring from these major drains, they conveyed through fault plays and damaged zones up. Most fluids are deep-seated CO2 rich fluids mixed with a water component, thanks to the system's decompression and subsequent downward penetration of waters.

-Specific chemical traps for gold are either the micro-fractured massive sulphide ore bodies or mineral and structural trap such as the Kamoeb quartz veins systems. The high gold endowment of the Arabian-Nubian Shield is correlated with the abundance of ophiolitic sutures. It could have been a source for the gold after syn to post-obduction serpentinisation and carbonatation. Thus, massive sulphides are not necessarily the main source for gold, and deformation of VHMS not only the main process of metal extraction.

Therefore, the Ariab-Arbaat gold district would be classified as a representative of the shear-zone-related orogenic gold deposits class. The late-D3 gold event in the Ariab-Arbaat belt has all the makings of an orogenic gold system, remarkably similar to the Late Carboniferous gold event in the West European Variscan belt.

Acknowledgements

This work was conducted through Dr A. Fatima's PhD and was financed by a contract between Areva (now Orano) and CREGU. Authors are indebted to Ariab Arbat company for logistics

and authorisation to sample and study these deposits. J-L Lescuyer (Areva, now Orano) is warmly acknowledged for following and co-supervising parts of the PhD work.

REFERENCES

Abdel Rahman, E.M., 1993. Geochemical and geotectonic controls of the metallogenic evolution of selected ophiolite complexes from the Sudan. Berliner Geowissenschaftliche Abhandungen, Reihe A, 145, 1-175.

Abdelsalam, M.G., 1994. The Oko shear zone, Sudan: post-accretionary deformation in the Arabian-Nubian Shield. Journal of the Geological Society, London 151, 767-776.

Abdelsalam, M.G., Stern, R.J., 1993. Timing of events along the Nakasib suture and the Oko shear zone, Sudan. In: Thorweihe, U., Schandelmeier, H. (Eds.), Geoscientific research in Northeast Africa. Balkema, Rotterdam, 93-103.

Abdelsalam, M.G., Stern R.J., 1996. Sutures and shear zones in the Arabian-Nubian Shield. Jourrnal of African Earth Sciences 23, 289-310.

Abu-Alam, T., Abd El Monsef, M., Grosch, E., 2019. Shear-zone hosted gold mineralization of the Arabian–Nubian Shield: devolatilization processes across the greenschist–amphibolite-facies transition. In: Ferrero, S., Lanari, P., Goncalves, P., Grosch, E. G. (Eds.), Metamorphic Geology: Microscale to Mountain Belts. Geological Society, London, Special Publications 478, 287–313.

Abu Fatima, M., 2006. Metallogenesis and geotectonic evolution of the polymetallic massive sulphide and associated gold deposits in the Ariab-Arbaat belt (Red Sea Hills, NE Soudan). Ph.D. thesis, Nancy1 University (UHP), France.

Almond, D.C., Darbyshire, D.P.F., Ahmed, F., 1989. Age limits for major shearing episodes in the Nubian Shield of NE Sudan. Journal of African Earth Sciences 9, 489-496.

Anders, E., Grevesse, N., 1989. Abundances of the elements: Meteoritic and solar. Geochimica Cosmochimica Acta 53, 197-214.

Barrie, C.T., Hannington, M.D., 1999. Classification of Volcanic-Associated Massive Sulfide Deposits Based on Host-Rock Composition. Reviews in Economic Geology, 1-11

Blasband, B., White, S., Brooljmans, P., De Boorder, H., Visser, W., 2000. Late Proterozoic extensional collapse in the Arabian-Nubian Shield. Journal of the Geological Society 157, 615-628.

Bodnar, R. J., 2003. Introduction to fluid inclusions. In: Samson, I., Anderson, A., Marshall, D. (Eds.), Fluid Inclusions: Analysis and Interpretation. Mineralogical Association of Canada, Short Course 32, 1-8.

Boiron, M.C., Cathelineau, M., Dubessy, J., Bastoul, A.M., 1990. Fluids in Hercynian Au-veins from the French Variscan belt. Mineralogical Magazine 54, 231-243.

Boiron, M.C., Essarraj, S., Sellier , E., Cathelineau, M., Lespinasse, M., Poty, B, 1992. Identification of fluid inclusions in relation to their host microstructural domains in quartz by cathodoluminescence. Geochimica Cosmochimica Acta 56, 175-185.

Boiron, M.C., Cathelineau, M., Banks, D.A., Yardley, B.W.D., Noronha, F., Miller, M.F., 1996. P-T-X conditions of late Hercynian fluid penetration and the origin of the granite-hosted Au quartz veins in NW Iberia: a multidisciplinary study of fluid inclusions and their chemistry. Geochimica Cosmochimica Acta, 60, 43-57.

Boiron, M.C., Barakat, A., Cathelineau, M., Banks, D.A., Durisova, J., Moravek, P., 2001. Geometry and P-V-T-X conditions of microfissural fluid migration: the Mokrsko gold deposit (Bohemia). Chemical Geology 173, 207-225.

Boiron, M.-C., Cathelineau, M., Banks, D.A., Fourcade, S., Vallance, J., 2003. Mixing of metamorphic and surficial fluids during the uplift of the Hercynian upper crust: consequences for gold deposition. Chemical Geology 194, 119-142.

Cathelineau, M., 1988. Cation site occupancy in chlorites and illites as a function of temperature. Clay Minerals 23, 471-485.

Cheng, X.H., Xu, J-H., Wang, J-X., Xue, Q-B., Zhang, H., 2016. Carbonic fluids in the Hamadi gold deposit, Sudan: Origin and contribution to gold mineralization. Canadian Journal of Earth Sciences 54, 494-511.

Conde, C., Tornos, F., Large, R., Danyushevsky, L.V., Solomon, S., 2009. Laser ablation-ICPMS analysis of trace elements in pyrite from the Tharsis massive sulphide deposit. In: Williams, P.J. et al. (Eds)., Smart science for exploration and mining. Proceedings of the 10th SGA Biennal Meeting, Townsville, 418-420.

Cortial, P., Lefevre, J.C., Salah, H.A., 1985. Gold deposits related to the volcano-sedimentary sequences of Ariab, Sudan. In: Prospecting in areas of desert terrain, Institute of Mining and Metallurgy, London, 155-159.

Cottard, F., Braux, C., Cortial, P., Deschamps, Y., Elsamani, Y., Hottin, A.M., Younis, M.O., 1986a. Les amas sulfurés polymétalliques et les minéralisations aurifères du district d'Ariab (Red Sea Hills, Soudan). Historique de la découverte, cadre géologique et principaux caractères des gisements. Chronique des Mines et de la Recherche Minière 483, 19-40.

Cottard, F., Deschamps, Y., Braux, C., Elsamani, Y., 1986b. Gold deposits of Ariab area. BRGM Report 86SDN 110.

Cottard ,F., Abdulhay, G.J., Artignan, D., Gélot, J.L., Roubichou, P., Trinquart, R., Vadala, P,. 1993. The Al Hajar gold deposit (Kingdom of Saudi Arabia): a newly discovered example of supergene enrichment from a massive sulphide deposit of Late Proterozoic age. Chronique des Mines et de la Recherche Minière 510, 13-24.

Debon, F., Le Fort, P., 1988. A cationic classification of common plutonic rocks and their magmatic associations: Principles, method, applications. Bulletin de Minéralogie 111, 493–510.

Deschamps, Y., Lescuyer, J.L., Guerrot, C., Osman, A.A., 2004. Lower Neoproterozoic age of the Ariab volcanogenic massive sulphide mineralization, Red Sea Hills, Sudan. 20th Coll. African Geology, BRGM, Orléans, 133.

Dostal, J., Keppie, J.D., Zhai, M., 1992. Geochemistry of mineralized and barren Late Proterozoic felsic volcanic rocks in southeastern Cape Breton Island, Nova Scotia (Canada). Precambrian Research 56, 33-49.

Essarraj, S., Boiron, M.-C., Cathelineau, M., Fourcade, S., 2001. Multistage deformation of Au-quartz veins (Lauriéras, French Massif Central): evidence for late gold introduction from microstructural, isotopic and fluid inclusion studies. Tectonophysics 336, 79-99.

Franklin, J.M., 1993. Volcanic-associated massive sulphide deposits. In: Kirkham, R.V., Sinclair, W.D., Thorpe, R.I., Duke, J.M. (Eds.), Mineral deposits modelling. Geological Association of Canada Special Paper 40, 315-334.

Franklin, J.M., Gibson, H.L., Jonasson, I.R., Galley, A.G., 2005. Volcanogenic massive sulfide deposits. In: Hedenquist, J.W., Thompson, J.F.H., Goldfarb, R.J., Richards, J.P. (Eds.), Economic Geology One Hundreth Anniversary Volume. Society of Economic Geologists, InC., Littleton, Colorado, 523-560.

Glasby, G.P., Iizara, K., Yuase, M., Usui, A., 2000. Submarine hydrothermal mineralisation on the Izu-Bonin Arc, south of Japan: an overview. Marine Geosciences and Technology 18, 141-176.

Goldfarb, R.J., Baker, T., Dubé, B., Groves, D.I., Hart, C.J.R., Gosselin, P., 2005. Distribution, character and genesis of gold deposits in metamorphic terranes. In: Hedenquist, J.W., Thompson, J.F.H., Goldfarb, R.J., Richards, J.P. (Eds.), Economic Geology One Hundreth Anniversary Volume. Society of Economic Geologists, InC., Littleton, Colorado, 407-450.

Gartz, V.H., Frimmel, H.E., 1999. Complex metasomatism of an Archean placer in the Witwatersrand Basin, South Africa; the Ventersdorp contact reef; a hydrothermal aquifer? Economic Geology 94, 689-706

Grant, J.A., 1986. The isocon diagram – a simple solution to Gresen's equation for metasomatic alteration. Economic Geology 81, 1976-1982.

Gu, L.X., Tang, X.Q., Zheng, Y.C., Wu, C.Z., Lu, J.J., Ni, P., Xiao, X.J., 2005. Formation mechanisms of oreshoots in massive sulphide orebodies at Hongtoushan, NE China. In: Mao, J., Bierlein, F.P. (Eds.), Mineral deposit research: Meeting the global challenge. Proceedings of the 8th Biennal SGA meeting, Beijing, China, Springer, 611-614.

Hart, T.R., Gibson, H.L., Lesher, C.M., 2004. Trace element geochemistry and petrogenesis of felsic volcanic rocks associated with volcanogenic massive Cu-Zn-Pb sulfide deposits. Economic Geology 99, 1003-1013.

Herrington, R., Maslennikov, V., Zaykov, V., Seravkin, I., Kosarev, A., Buschman, B., Orgeval, J.J., Holland, N., Tesalina, S., Nimis, P., Armstrong, R., 2005. Classification of VMS deposits: Lessons from the South Uralides. Ore Geology Reviews 27, 203-237.

Herzig, P.M., Hannington, M.D., Fouquet, Y., von Stackelberg, U., Petersen, S., 1993. Gold-rich polymetallic sulfides from the Lau back-arc and implications for the geochemistry of gold in sea-floor hydrothermal systems in the Southwest Pacific. Economic Geology 88, 2182-2209.

Höhndorf, A., Meinhold, K.-D., Vail, J.R., 1995. Geochronology of anorogenic igneous complexes in the Sudan: isotopic investigations in North Kordofan, the Nubian Desert and the Red Sea Hills. Journal of African Earth Sciences 19, 3-15.

Hottin, A.M., Laforet, B., 1986. Expression minéralogique de l'or dans les roches silico-barytiques et les amas sulfurés d'Ariab (Soudan). BRGM Report 86SDN004GEO.

Huston, D.L., Bottrill, R.S., Creelman, R.A., Zaw, K., Ramsden, T.R., Rand, S.W., Gemmell, J.B., Jablonski, W., Sie, S.H., Large, R.R., 1992. Geologic and geochemical controls on the mineralogy and grain size of gold-bearing phases, Eastern Australia volcanic-hosted massive sulphide deposits. Economic Geology 87, 542-563.

Ihle, T., Petersen, S., Herzig, P.M., Hannington, M.D., 2005. Siting of gold and characteristics of gold-bearing massive sulfides from the interior of the felsic-hosted PACMANUS massive sulfide deposit, eastern Manus basin (PNG). In: Mao, J., Bierlein, F.P. (Eds.), Mineral deposit research: Meeting the global challenge. Proceedings of the 8th Biennal SGA meeting, Beijing, China, Springer, 623-626.

Johnson, P.R., Woldehaimanot, B., 2003. Development of the Arabian-Nubian Shield: perspectives on accretion and deformation in the northern East Africa Orogen and the assembly of Gondwana. In: Yoshida, M., Dasgupta, S., Windley, B. (Eds.), Proterozoic

Eastern Gondwana: Supercontinent assembly and break-up. Geological Society of London Special Paper 206, 289-325.

Kroner, A., Greiling, R., Reischmann, T., Hussein, I.M., Stern, R.J., Durr, S., Kruger, J., Zimmer, M., 1987. Pan-African crustal evolution in the Nubian segment of northeast Africa. American Geophysical Union Geodynamic Series 17, 235-257.

Kroner, A., Stern, R.J., Linnebacker, P., Reischmann, T., Manton, W., Hussein, I.M., 1991. Evolution of Pan-African island arc assemblages in the southern Red Sea Hills, Sudan, as exemplified by geochemistry and geochronology. Precambrian Research 53, 99-118.

Kusky, T.M., Matsah, M.I., 2003. Neoproterozoic dextral faulting on the Najd Fault System, Saudi Arabia, preceded sinistral faulting and escape tectonics related to closure of the Mozambique Ocean. Geological Society, London, Special Publications 206, 327-361.

Kusky, T.M., Abdelsalam, M., Tucker, R., Stern, R., 2003. Evolution of the East African and related orogens and the assembly of Gondwana. Special Issue of Precambrian Research 123, 81-144.

Kuster, D., Hengst, M., Piolel, J., 1993. Evolution of Pan-African granitoid magmatism along the southern Nakasib suture zone, Red Sea Hills, Sudan. In: Thorweihe, U., Schandelmeier, H. (Eds.), Geoscientific research in Northeast Africa. Balkema, Rotterdam, 111-115.

La Roche, H. de, 1980. Granites chemistry through multicationic diagrams. Sciences de la Terre Informatique Géologique 13, 65–88.

Lentz, D.R., 1998. Petrogenetic evolution of felsic volcanic sequences associated with Phanerozoic volcanic-hosted massive sulphide systems: the role of extensional geodynamics. Ore Geology Reviews 12, 289-327.

Lescuyer, J.L., Cassard, D., Deschamps, Y., 1994. Mise en évidence d'une tectonique ductile transcurrente dextre dans les ceintures volcano-édimentaires de Samran (Arabie Saoudite) et d'Ariab (Soudan) au Protérozoïque supérieur. Comptes Rendus de l'Académie des Sciences Paris, 319, série II, 1545-1554.

Lesher, C.M., Campbell, H.L., 1987. Trace-element geochemistry of ore-associated and barren, felsic metavolcanic rocks in the Superior Province, Canada: Reply. Canadian Journal of Earth Sciences 24, 1498-1500.

Lesher, C.M., Goodwin, A.M., Campbell, I.H., Gorton, P., 1986. Trace-element geochemistry of ore-associated and barren, felsic metavolcanic rocks in the Superior Province, Canada. Canadian Journal of Earth Sciences 23, 222-237.

Marignac, C., Cathelineau, M., 2006. Comment on the paper by Sanchez-España et al.: source and evolution of ore-forming hydrothermal fluids in the northern Iberian pyrite belt massive

sulphide deposits (SW Spain): evidence from fluid inclusions and stable isotopes (Mineralium Deposita 38: 519-537). Mineralium Deposita 40, 742-748.

Marignac, C., Diagana, B., Cathelineau, M., Boiron, M.-C., Banks, D., Fourcade, S., Vallance J., 2003. Remobilization of base metals and gold by Variscan metamorphic fluids in the south Iberian belt: evidence from Tharsis VMS deposit. Chemical Geology 194, 143-165.

Massonne, H.-J., Schreyer, W., 1987. Phengite geobarometry based on the limiting assemblages with K-feldspar, phlogopite, and quartz. Contributions to Mineralogy and Petrology 96, 212-234.

McClenaghan, S. H., Lentz, D.R., Martin, J., Dieger, W.G., 2009. Gold in the Brunswick No. 12 volcanogenic massive sulfide deposit, Bathurst Mining Camp, Canada: Evidence from bulk ore analysis and laser ablation ICP─ MS data on sulfide phases Mineralium Deposita 44, 523-557.

Mercier-Langevin, P., Hannington, M.D., Dubé, B., Bécu, V., 2010. The gold content of volcanogenic massive sulfide deposits. Mineralium Deposita 46, 509-539.

Patchett, P.D., Chase, C.G., 2002. Role of transform continental margins in major crustal growth episodes. Geology 30, 39-42.

Pearce, J.A., Peate, D.W., 1995. Tectonic implication of the composition of volcanic arc lavas. Annual Reviews in Earth and Planetary Sciences 23, 251-285.

Prokin, V.A., Buslaev, F.P., 1999. Massive copper-zinc sulphide deposits in the Urals. Ore Geology Reviews 14, 1-69.

Recoché, G., 1989. Les concentrations aurifères supergènes liées aux minéralisations sulfurées polymetalliques de la ceinture volcano-sédimentaire d'Ariab-Arbaat (Red Sea Hills) : étude du gisement de Hassai. Document du Bureau de Recherches Géologiques et Minières (BRGM) 226.

Ringwood, A.E., 1991. Phase transformations and their bearing on the constitution and dynamics of the mantle. Geochimica Cosmochimica Acta 55, 2083-2110.

Rollinson, H., 1993. Using geochemical data: evaluation, presentation, interpretation. Longman Group UK Limited, 1-352.

Stern, R.J., Johnson, P.R., Kröner, A., Yibas, B., 2004. Neoproterozoic ophiolites of the Arabian-Nubian Shield. In: Kusky, T.M. (Ed.), Precambrian ophiolites and related rocks. Developments in Precambrian Geology 13 (Condie K.C., Series Editor), 95-128.

Stern, R.J., Nielson, K.C., Best, E., Sultan, M., Arvidson, R.E., Kroner, A., 1990. Orientation of late Precambrian sutures in the Arabian-Nubian Shield. Geology 18, 1103-1106.

Syme, E.C., Lucas, S.B., Bailes, A.H., Stern, R.A., 1998. Contrasting arc and MORB-like assemblages in the Paleoproterozoic Flin Flon Belt, Manitoba, and the role of intra-arc extension in localizing volcanic-hosted massive sulphide deposits. Canadian Journal of Earth Sciences 36, 1767-1788.

Teklay, M., Haile, T., Kröner, A., Asmerom, Y., Watson, J., 2003. A back-arc palaeotectonic setting for the Augaro Neoproterozoic magmatic rocks of Western Eritrea. Gondwana Research 6, 629-640.

Thome, K.G., McLeod, M.J., Lentz, D.R., 2007. Spatial and temporal distribution of gold mineralization in the New Brunswick segment of the Northern Appalachians, eastern Canada. In: Andrew, C.J. et al. (Eds.), Digging Deeper. Proceedings of the 9th Biennal SGA Meeting, Dublin, 923-926.

Vallance, J, Cathelineau, M., Boiron, M.-C., Shepherd, T. J., Naden, J., 2003. Impact of late aplitic magmatism on C-rich rocks and gold deposition at Castromil (North Portugal). Chemical Geology 194, 201-224.

Vallance, J., Boiron, M.-C., Cathelineau, M., Fourcade, S., Marignac, C., 2004. The granite hosted gold deposit of Moulin de Cheni (St Yrieix District, Massif Central, France): petrographic, structural, fluid inclusion and oxygen isotope constraints. Mineralium Deposita 39, 265-281.

Vikentyev, V.I., 2005. Gold and silver in Cu-Zn massive sulphide deposits of the Urals. In: Mao, J., Bierlein, F.P. (Eds.), Mineral deposit research: Meeting the global challenge. Proceedings of the 8th Biennal SGA meeting, Beijing, China, Springer, 709-710.

Wagner, T., 2007. Thermodynamic modelling of Au-Bi-Te melt precipitation from high-temperature hydrothermal fluids: Preliminary results. In: Andrew, C.J., et al. (Eds.), Digging Deeper. Proceedings of the 9th Biennal SGA Meeting, Dublin, 769-772.

Wagner, T., Klemd, R., Wenzel, T., Mattsson, B., 2007. Gold upgrading in metamorphosed massive sulfide ore deposits: direct evidence from laser-ablation-inductively coupled plasma-mas spectrometry analysis of invisible gold. Geology 35, 775-778.

Weisbrod, A., 1984. Utilisation des inclusions fluides en géothermométrie. In : Lagache, M., (Ed.), Thermométrie et Barométrie Géologiques. Société Française de Minéralogie et de Cristallographie 2, 416-481.

Whalen, J.B., Syme, E.C., Stern, R.A., 1998. Geochemical and Nd isotopic evolution of Paleoproterozoic arc-type granitoid magmatism in the Flin Flon Belt, Trans-Hudson orogen, Canada. Canadian Journal of Earth Sciences 36, 227-250.

Winchester, J.A., Floyd, P.A., 1977. Geochemical discrimination of different magma series and their differentiation products using immobile elements. Chemical Geology 20, 325-343.

Yardley, B.W.D., 1989. An introduction to metamorphic petrology. Longman Earth Science Series, 1-248.

Figure captions

Figure 1. Schematic tectonic map of the Arabian-Nubian Shield, with the location of the Ariab belt (redrawn and adapted from Johnson et al., 2011, with complementary data from Barrie et al. 2016, Bierlein et al., 2016), and Zoheir et al., 2019)

Figure 2. Diagrammatic cross-section through the Gebeit-Oshib-Haya terranes, showing the Amur-Nakasib ophiolitic suture and the Ariab Series (redrawn from Abu Fatima, 2006, after Abdel Rahman, 1993 and Wipfler, 1996).

Fig. 3. Main events affecting the Haya terrane (see text for explanation and references).

Figure 4. Reconstruction of the Ariab series lithologic pile before the D1 deformation event (redrawn from Abu Fatima, 2006).

Figure 5. Classification of the Ariab belt magmatic rocks in the SiO_2 *vs* Zr/TiO_2 (A) and Nb/Y vs Zr/TiO_2 (B) diagrams (Winchester and Floyd, 1977). The use of the "immobile" elements Zr and Ti partly alleviates the bias introduced by the strong hydrothermal alteration affecting most volcanic and many plutonic rocks (see text).

Figure 6. Projection of the Ariab belt magmatic rocks in adapted mineral-chemical diagrams. A. The A-B diagram of Debon and Le Fort (1988) for volcanic rocks of the Ariab Series. Numbers associated with rock symbols are the LOI. B. The A-B diagram of Debon and Le Fort (1988) for the Ariab-Arbaat belt plutonic G1 and G2 suites. C. The Q-P diagram of La Roche (1980) for all magmatic rocks of the Ariab-Arbaat belt. Although most of the volcanic and

many plutonic rocks are affected by an intense alteration (involving an increase of the peraluminous index A), a differentiation trend, common to all the volcanic series and, at least, the G1 plutonic rocks, remains discernable in all diagrams (see text).

Figure 7. Isocon plots (Grant 1986) for selected couple of "unaltered"-altered rocks from (A): Unit A basalts; (B): Unit B1 andesites; and (C): Unit C2 rhyolites.

Figure 8. Chondrite-normalized REE plots for the Ariab belt magmatic rocks (C1 chondrite normalizing values from Anders and Grevesse 1989). Data from the Augaro back-arc basalts in Eritrea (Teklay et al. 2003) have been added to the Unit A plot for comparison (see text).

Figure 9. MORB-normalized plots for the Ariab-Arbaat belt magmatic rocks, using the normalization and ordering scheme of Pearce (1983) (in Rollinson 1993), with LILE on the left and HFSE on the right, and incompatibility growing outward from Ba-Th (save the Cr addition on the right). Data for comparison with Ariab basalts: Flin Flon arc tholeiites, redrawn from Syme et al. (1998); Eritrea arc and back-arc basalts, redrawn from Teklay et al. (2003) (see text).

Figure 10 Projection of the Ariab-Arbaat belt volcanic rocks in the Th/Yb *vs* Nb/Yb diagram of Pearce and Peate (1995), showing clearly their oceanic island-arc affinity. G1 and G2 suites have also been projected for comparison.

Figure 11. Comparison of C2 felsic lavas with reference series in primitive mantle-normalized LILE-HFSE plots (normalizing values from Ringwood 1991). A: Comparison with the FI and FII Archean felsic metavolcanic rocks (redrawn from Lesher et al. 1986). B: Comparison with

the FIIIa and FIIIb Archean felsic metavolcanic rocks (redrawn from Lesher et al. 1986). C: Comparison with the Neoproterozoic Cape Breton Island felsic metavolcanic rocks from an ensimatic arc (redrawn from Dostal et al. 1972). D: Comparison with the Paleoproterozoic Flin Flon Belt felsic metavolcanic rocks from a primitive ensimatic arc (redrawn from Syme et al. 1998).

Figure 12. Geologic map of the central part of the Ariab area, with the location of the main gold occurrences (redrawn from Abu Fatima 2006).

A Adasselakh B Baderuk D Dimdim G Ganaet H Hassai HA Hadal Aouatib Hm Hamim Ht Hadayamet K Kamoeb M1-M5 Medadip 1 to 5 O Oderuk R Rukab S Shidimam T Talaiderut Y Yonim

Figure 13 Post-depositional transformations in the VHMS deposits. **a**. Porphyroclastic pyrite (py) in a quartz-sericite matrix (diffuse stockwork, Talaiderut) Qz1 and 2: two generations of syn-kinematic fibrous quartz ("pressure-shadows"). **b**. Porphyroclastic muscovite (mus) and pyrite (py) in a schistosed stockwork (Medadip 1) quartz: quartz amygdale. **c**. Differential behaviour of massive sulphides during deformation (Yonim): fractured pyrite (py) and ductile chalcopyrite (cp) (left); sketch of relationships in the same thin section (right) chl: chlorite; qtz: porphyroclastic quartz; S1, T1, and S2, T2: two generations of schistosity and related tension gashes. **d**. Differential behaviour of massive sulphides (Hassai): porphyroclastic pyrite (py) and sphalerite (sp) fractured and enclosed in ductile chalcopyrite (cp) elongated in S1; Qz: quartz; cv: supergene covellite. **e**. Two pyrite generations in the massive sulphides (Medadip 5): cataclastic pyrite (py1), quartz (qz), and chalcopyrite (cp) banding (S0+S1) and porphyroblastic euhedral pyrite (py2). **f**. Annealed pyrite (py) (Baderuk) Qz: quartz.

Figure 14. Paragenetic evolution in the VHMS and Kamoeb deposits.

Figure 15. Late events in the massive sulphides. **a**. Quartz (Qtz) and chalcopyrite (Ccp) possibly recrystallised with pyrite (Py) annealing (Medadip 5). **b**. Replacement of syn-kinematic fibrous quartz (Qtz1) by post-kinematic chlorite (Chl) (Barut) Qtz: quartz; Tit: titanite. **c**. Fracture-dissolution in pyrite (Py), filled with chalcopyrite (Ccp), sphalerite (Sp), and tennantite (Hadal Ouatib). **d**. Dissolution cavity in pyrite (Py), filled by pyrrhotite (Po), arsenopyrite (Apy), and tennantite (Hassai). **e**. Microvugs inside annealed pyrite (Py), filled with sphalerite (Sp), chalcopyrite (Ccp), galena (Gn), and altaite (SEM-BSE, Medadip 1); note that the microvugs developed independently from the pyrite joints. **f**. Microcrack in pyrite (Py) with altaite sealings (SEM-BSE, Hadal Aouatib).

Figure 16. Gold setting in late microstructures. **a**. Brecciated microcrystalline pyrite (pyrite 1) with quartz filling (SEM-BSE, Adassedakh); Gn: galena; Sp: sphalerite; Ccp: chalcopyrite; AuAg: electrum. **b**. Detail of a: gold is associated with recrystallised pyrite in relation with the brecciation. **c**. Native gold along actinolite (Act) cleavages (SEM-BSE, Yonim). **d**. Gold (Au) in brittle fractures affecting magnetite (Mgt) and in re-activated S1 schistosity marked by chlorite (Chl) (Ganaet); Brt: barite; Q2: fibrous (syn-D2) quartz ("pressure-shadow" around the magnetite). **e**. Gold (Au) in kinked chlorite (Chl) (D2 structure, Ganaet); note that gold is either along cleavage or cross-cutting them, demonstrating a post-D2 introduction.

Figure 17. Massive barite and associated hematite-chlorite schists. **a**. Porphyroclastic barite (Brt) (Hamim) Qtz: quartz; Chl: chlorite. **b**. F2 microfold affecting the S1 hematite schistosity (Ganaet) Mgt: magnetite. **c**. Early magnetite (Mgt) wrapped in the S1 hematite (Hem) schistosity (Medadip 3); Chl: iron-stained chlorite. **d**. Early (pre-S1) microfolds (slumps?)

(white arrow) (Hamim) S0: primary bedding; S1: main schistosity; Chl: iron-stained chlorite; Mgt: early magnetite; Qtz: quartz in "pressure-shadow". **e**. Late D3 microcracks and quartz (Qtz) infillings in magnetite (Ganaet). **f**. Gold association with late D3 microcracks in magnetite (Mgt) (Ganaet).

Figure 18. Geological map of the Kamoeb area, displaying the Kamoeb quartz vein setting (redrawn from Abu Fatima 2006, after Cortial et al., 1985). KE: Kamoeb east; KN: Kamoeb north; KS1, KS2: Kamoeb south, vein 1 and 2; KW: Kamoeb west.

Figure 19. Microstructures in the deformed Kamoeb quartz and the gold and sulphides settings. **a**. Existence of two successive flattening surfaces (S1, S2) materialised by microcrystalline quartz, and the associated stylolites (Sty 1, Sty 2) expressed as either indented grain contacts or (more often) as Ba-phengite accumulations. Stylolites 1 are microfolded with S2 as axial planes. Sample KAM 9209-3A. **b**. Schematic relationships in mylonitic quartz (Sample KAM 9309-123), with penetrative S2 and relicts of the pre-existing D1 microstructures, as S1 preserved within porphyroclastic domains and intensely microfolded stylolite 1. c. Sulphide setting in deformed quartz (Sample KAM9209-3C), with D1 relicts (mainly early phengite stylolite 1) and penetrative D2 features (S2, phengite stylolite 2). Pyrite is syn-kinematic for D2 (quartz pressure-shadows), whereas galena and gold overprint D2 features. d. Detail of c (redrawn from SEM-BSE imaging). e. Aspect of d (redrawn from SEM-BSE imaging).

Fig. 20 : Main types of fluid inclusions in quartz from Kamoeb and VHMS. a: quartz textures and simplified types of occurrences of fluid inclusions. b: microphotograph showing fluid inclusion FI assemblages in Q_{2-3}, c: deformed fluid inclusions in Q1, d: aqueous-carbonic three-phase Lc-w inclusion, e-f : Lw-c aqueous-carbonic two-phase fluid inclusions

Figure 21. Calculated bulk compositions (in molar fractions) of representative FI s from the quartz at Kamoeb and several VHMS (Yonim, Haddal Aouatib, Hassai). in a N_2/CO_2-H_2O diagram.

Figure 22. Reconstruction of the late (D3?) P-T-t evolution as recorded by fluid inclusion densities (isochores) from three representative areas (Yonim and Haddad Aouatib VHMS; Kamoeb quartz veins). The biotite-in isograd is from Yardley (1989, Fig. 3-11, p. 86). The Si-in-phengite geo-barometer isopleths (Massonne and Schreyer, 1987) and the Al-in-chlorite geo-thermometer isopleths (Cathelineau, 1988) have been drawn for relevant compositions. Isopleths (dotted dark blue lines) in the system H2O-CO2-NaCl are from Weisbrod (1984) for a salinity of 6 wt. % NaCl equiv., and a CO2 content of 10 (a) and 20 (b) mole%. See text for explanation.

Figure 23 Cross-section model of a typical Au-bearing gossan developed at the expense of a VHMS deposit from the Red Sea Hills (redrawn from Abu Fatima 2006, after Recoché 1989).

Table captions

Table 1. Representative analyses of the main rocks types from the Ariab Series and G1 and G2 suites. Italics designate the altered samples.

Table 2. Summary of the microthermometric measurements in the Kamoeb and VHMS (Yonim, Hadal Ouatib, and Hassai) quartz. Tm CO_2: melting temperature of the solid CO_2 Tm ice: final melting temperature of ice. Tm clat: final melting temperature of clathrates. Th CO_2: homogenisation temperature of the volatile phase. Th: bulk homogenisation temperature. L: homogenisation in the liquid phase, respectively.

Table 3. Bulk compositions from Raman microanalysis of selected FI from both the Kamoeb and the VHMS (Yonim, Haddal Aouatib, and Hassai) quartz. Tm CO_2: melting temperature of the solid "CO_2". Tm ice: final melting temperature of ice. Tm clat: final melting temperature of clathrates. Th CO_2(L): homogenisation temperature of the volatile phase in the liquid state. Th: bulk homogenisation temperature, *: decrepitated under heating.

Research highlights

VMS belong to an ensimatic Tonnian arc and cannot be considered as a gold-rich VMS

Gold is introduced in a late metamorphic brittle stage, part of the AN Shield gold province

Gold is mostly exploitable in gossans

Declaration of interests

☒ The authors declare that they have no known competing financial interests or personal relationships that could have appeared to influence the work reported in this paper.

☐The authors declare the following financial interests/personal relationships which may be considered as potential competing interests:

Author contributions

A.F: Investigation

CM: Supervision, Writing (original draft)

MC: Supervision, Writing (review, editing)

MCB : Data Curation

Fig. 1

Click here to access/download;Figure;Fig.1-Sudan-ANS-setting.tif

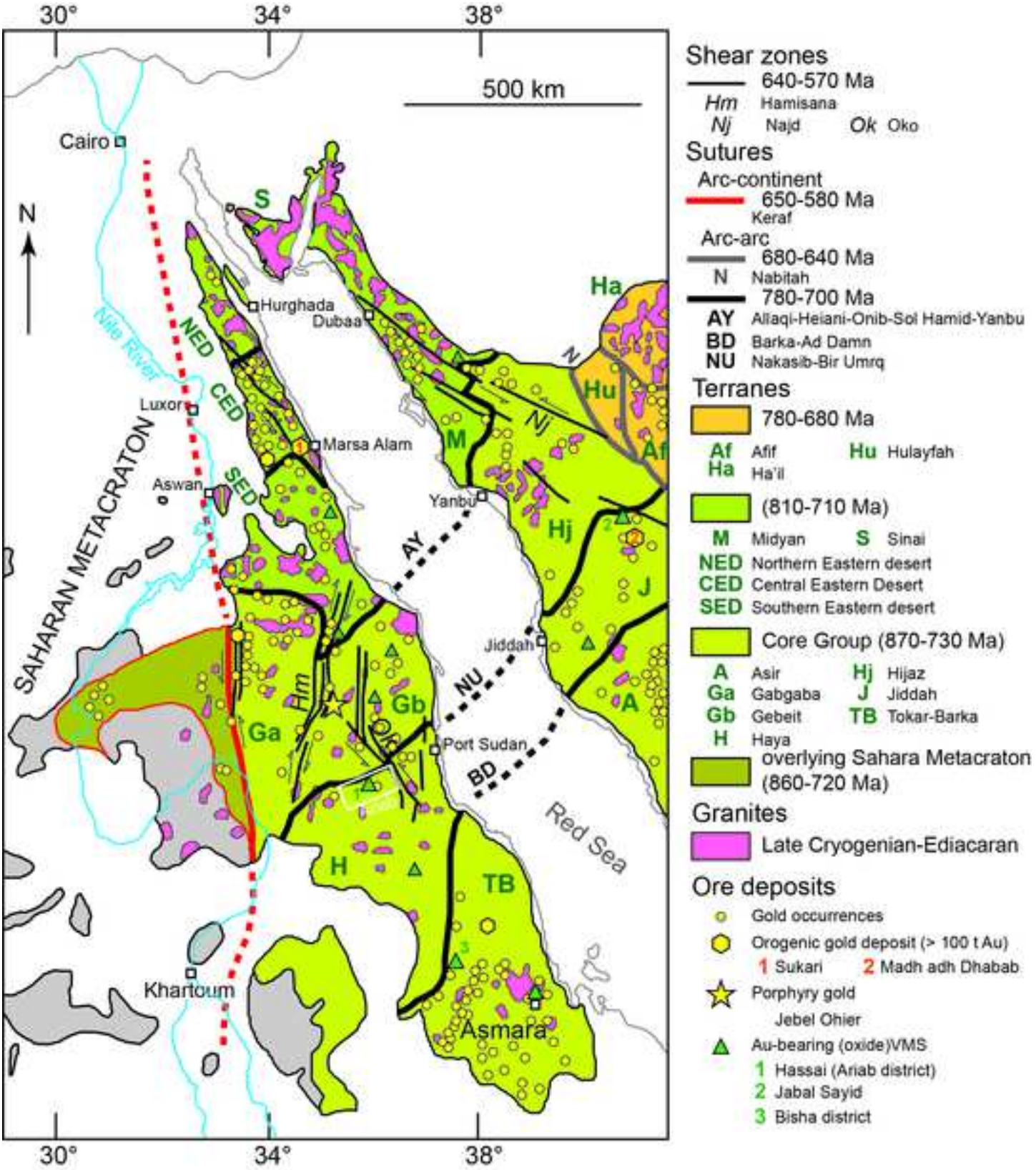

Fig. 2

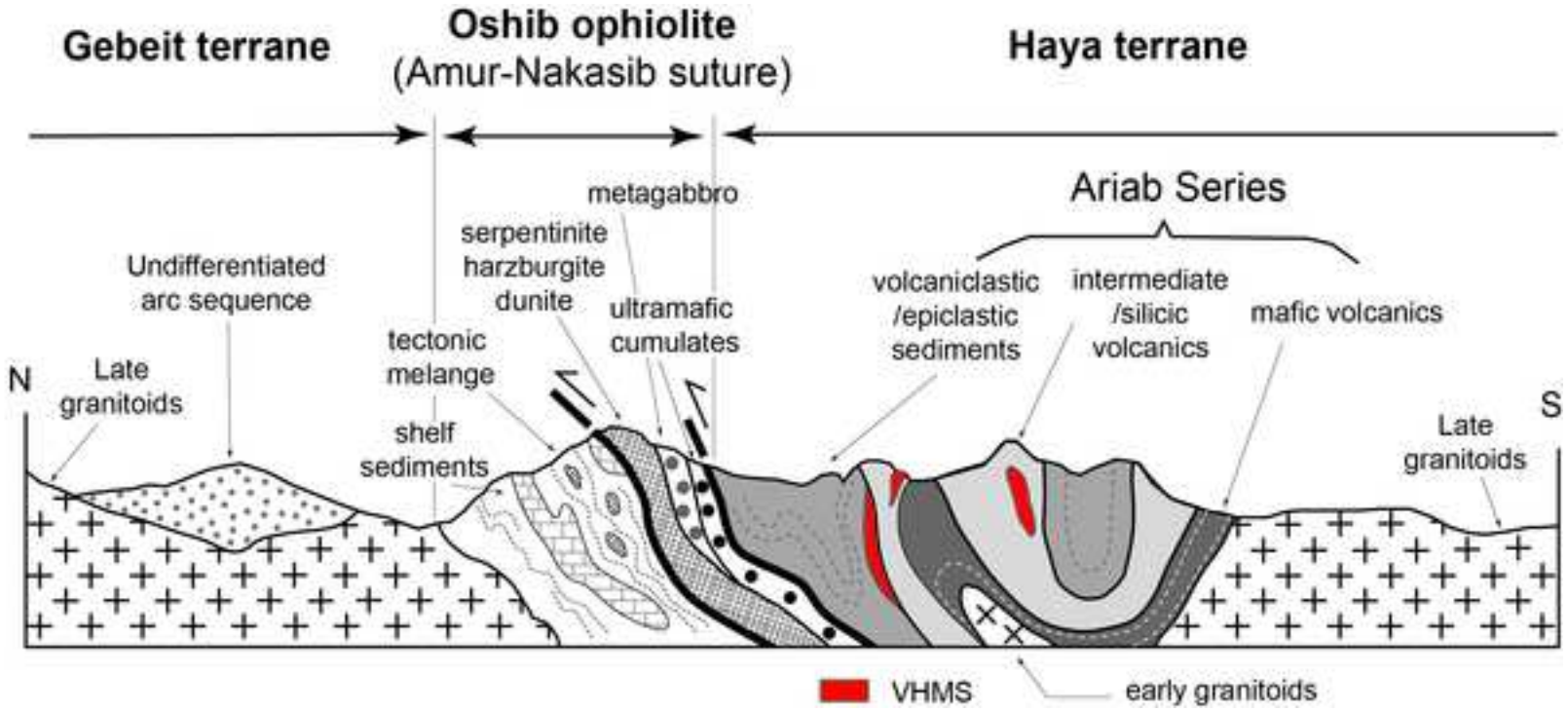

Fig. 3

Cycle	Global event	Tectono-metamorphic event	Objects	Age
Pan-African	Juvenile arc in oceanic environment	Hydrothermal sub-sea floor metamorphism	Basalt to rhyolite submarine to subaerian volcanism (Ariab Series) and coeval plutonism (G1 suite) VHMS and barite deposits	ca. 900 Ma G1 granitoids at 888±3.7 Ma
	Arc accretion and thickening	D1 Obduction and oblique arc collision Low-grade metamorphism	Regional S1 schistosity Recumbent to upright regional N60-70°E F1 folds Transpressive SZ	ca. 770 Ma
	unconformity	D2 Late shortening Low-grade metamorphism	Upright local N0-30°E F2 folds Regional S2 schistosity Dextral reactivation of D1 SZ	
	Evolved mature arc	Contact metamorphism	Awat-Aseriba calk-alkaline series Coeval to late plutonism (G2 suite)	730-720 Ma 720-680 Ma
	Final collision	D3 Transpression	Conjugated sinistral NW-SE to NNW-ESE and dextral NNE-SSW ductile to brittle SZ Faint local S3 schistosity	620-580 Ma
Gondwana break-up			Anorogenic plutonism	150 ± 4 Ma
Red Sea rift	Red Sea early opening	D4 Fracturation	NE-SW faults	Miocene

Fig. 4

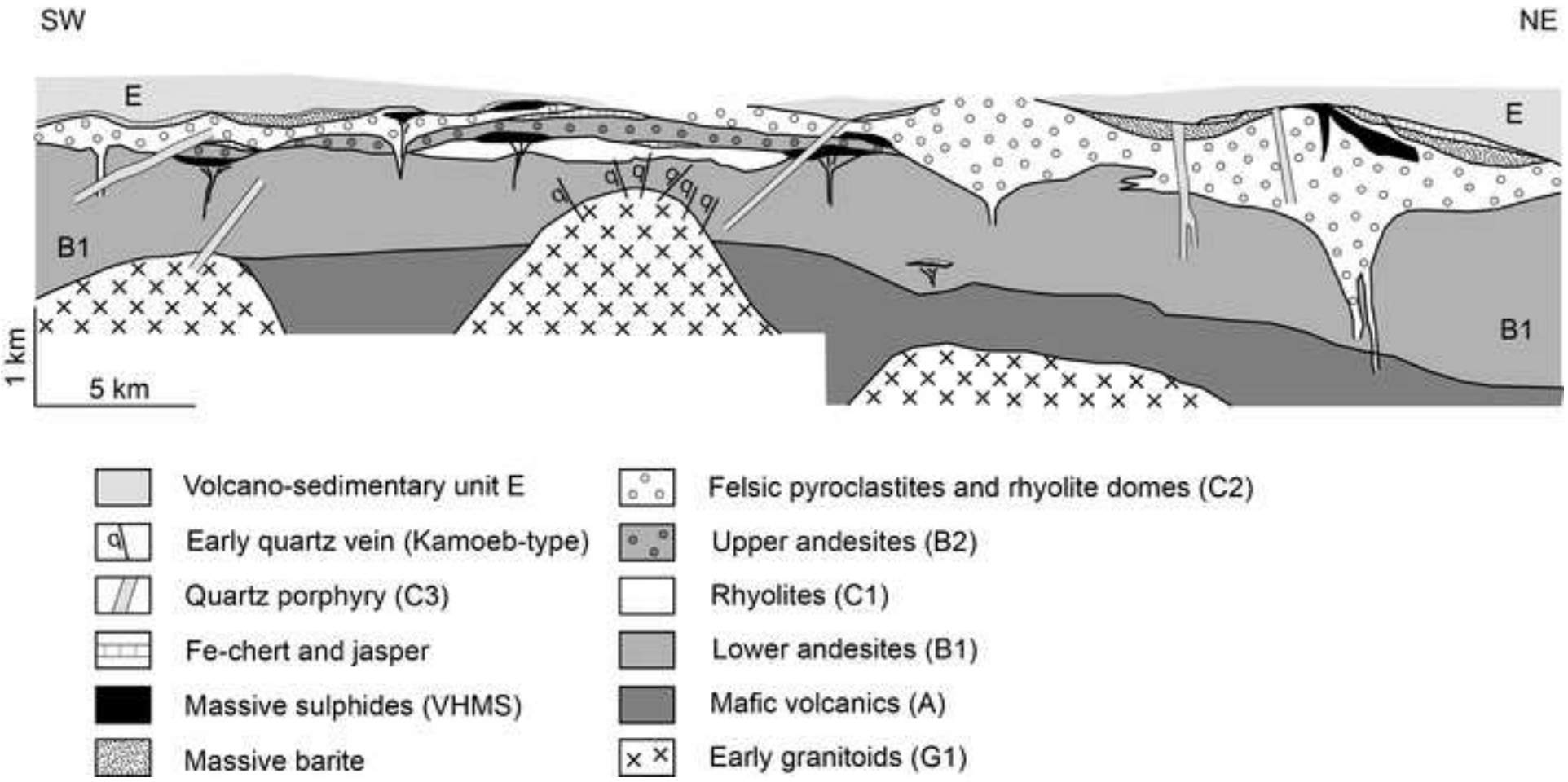

Fig. 5

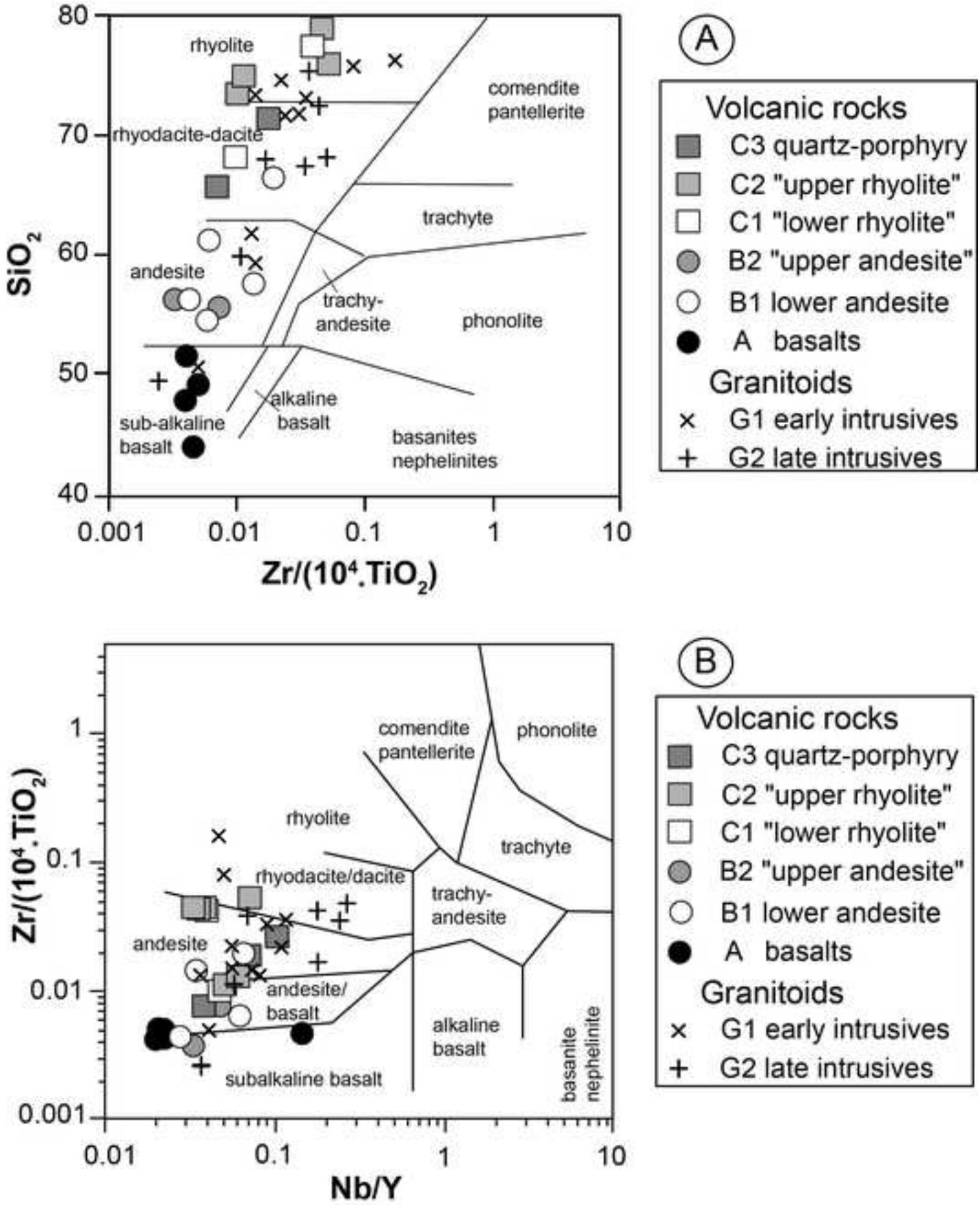

Fig. 6

Click here to access/download;Figure;Fig.6-Soudan-petro-AB-QP-vs1.tif

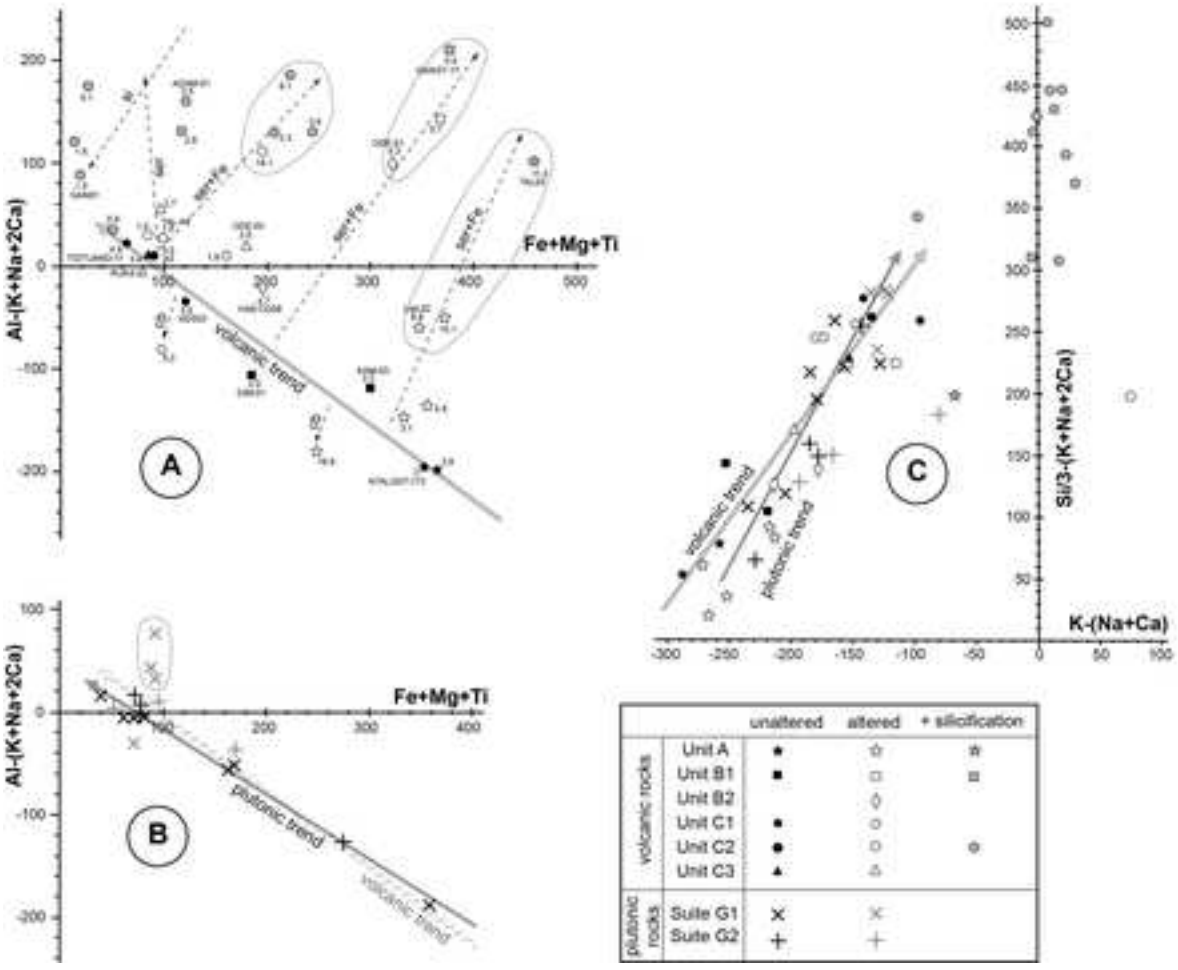

Fig. 7

Click here to access/download;Figure;Fig.7-Soudan-isocon.tif

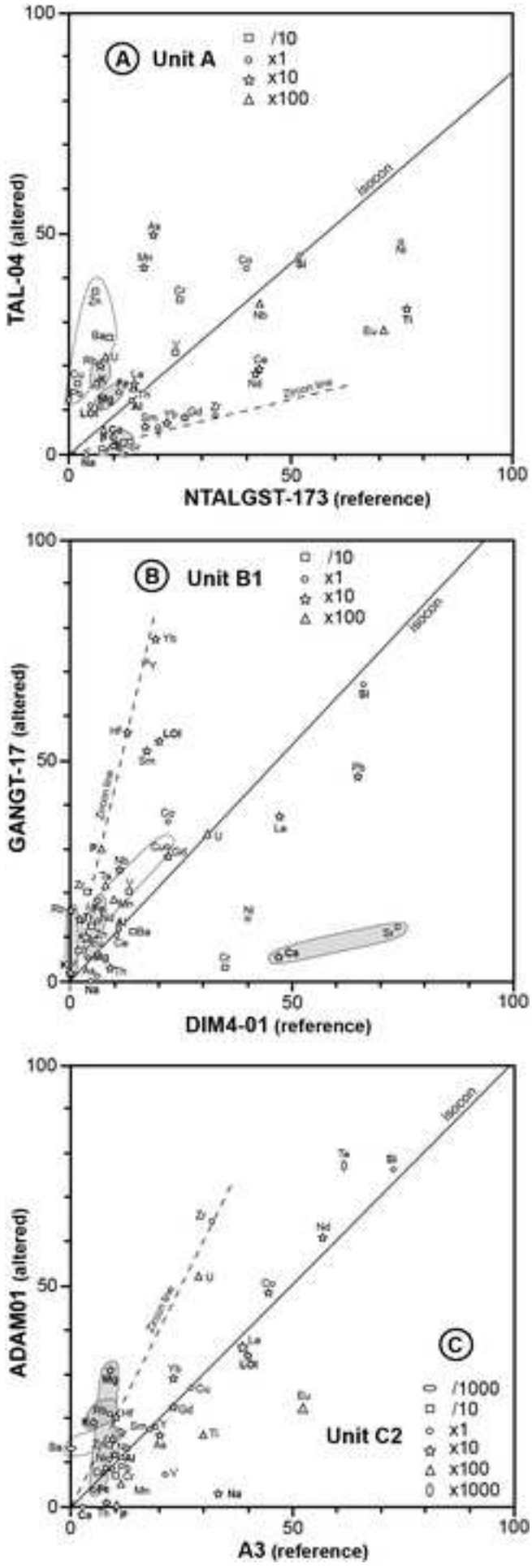

Fig. 8

Click here to access/download;Figure;Fig.8-Soudan-REE.tif

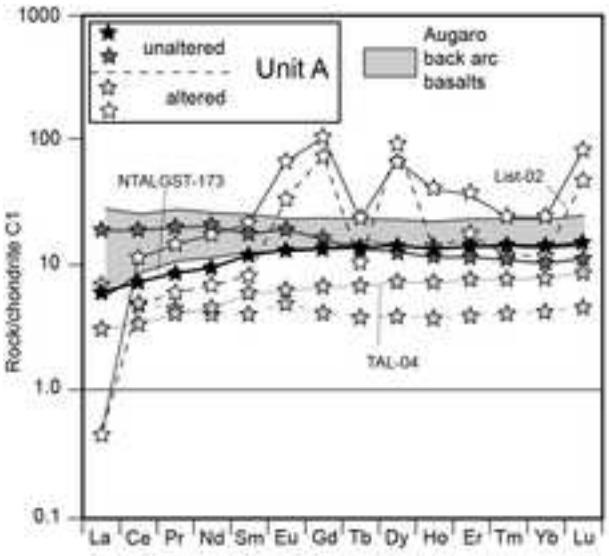

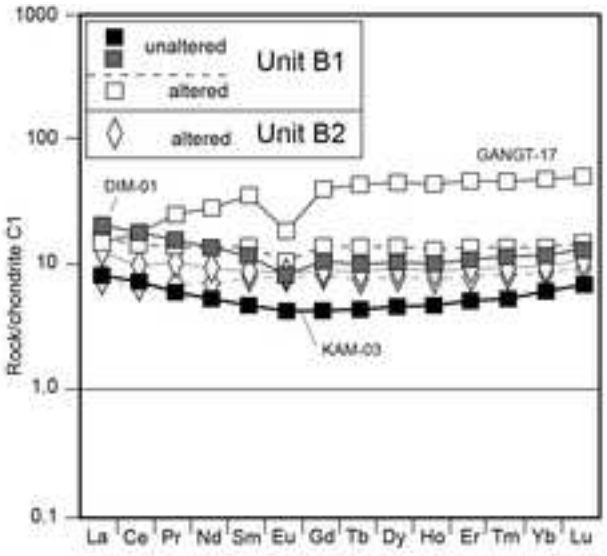

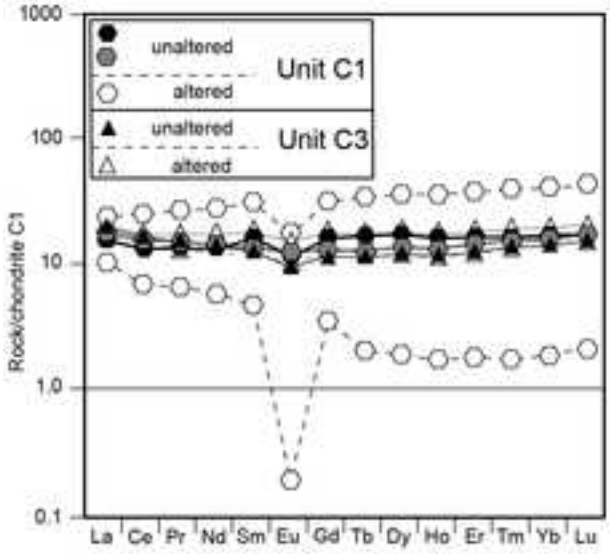

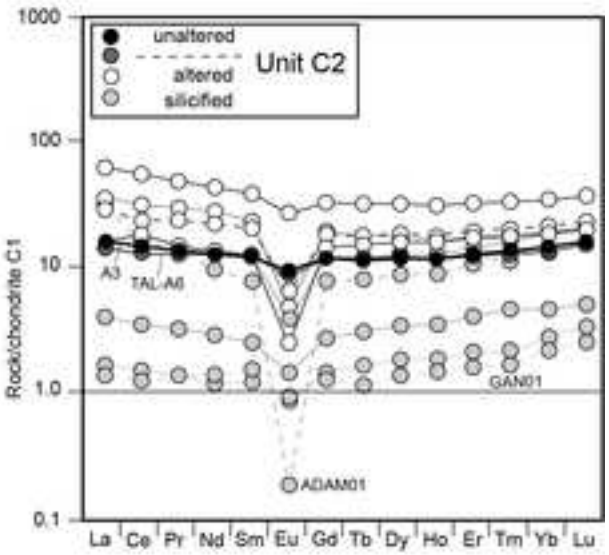

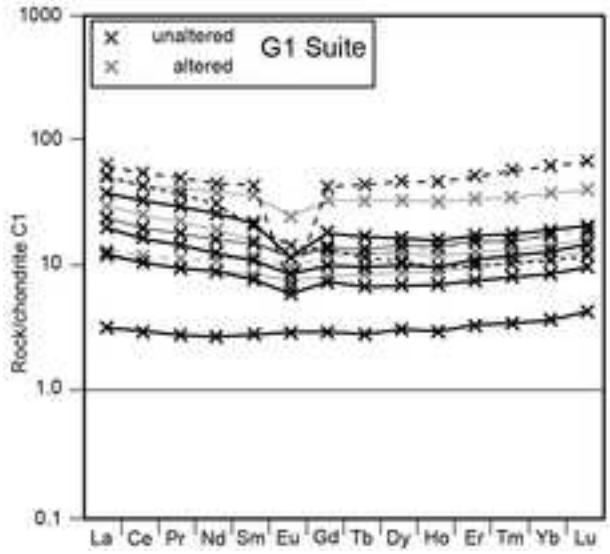

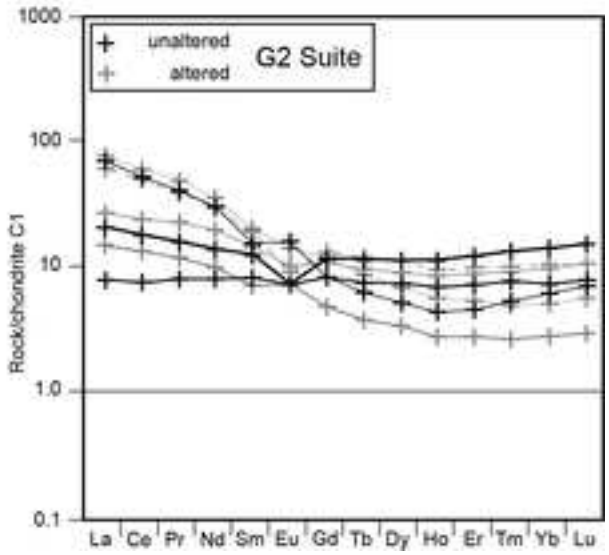

Fig. 9

Click here to access/download;Figure;Fig.9-Soudan-spider-total-vs2.tif

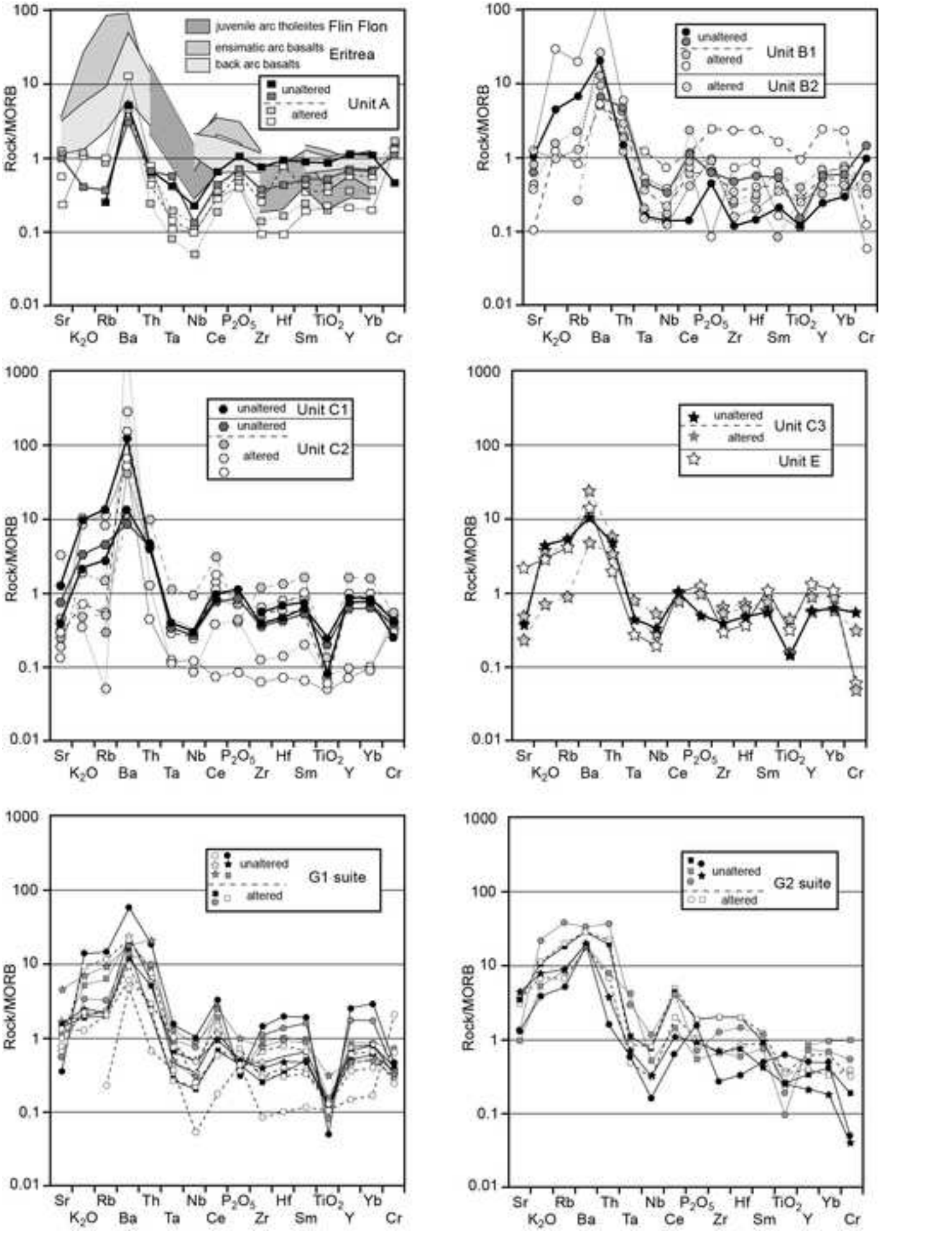

Fig. 10

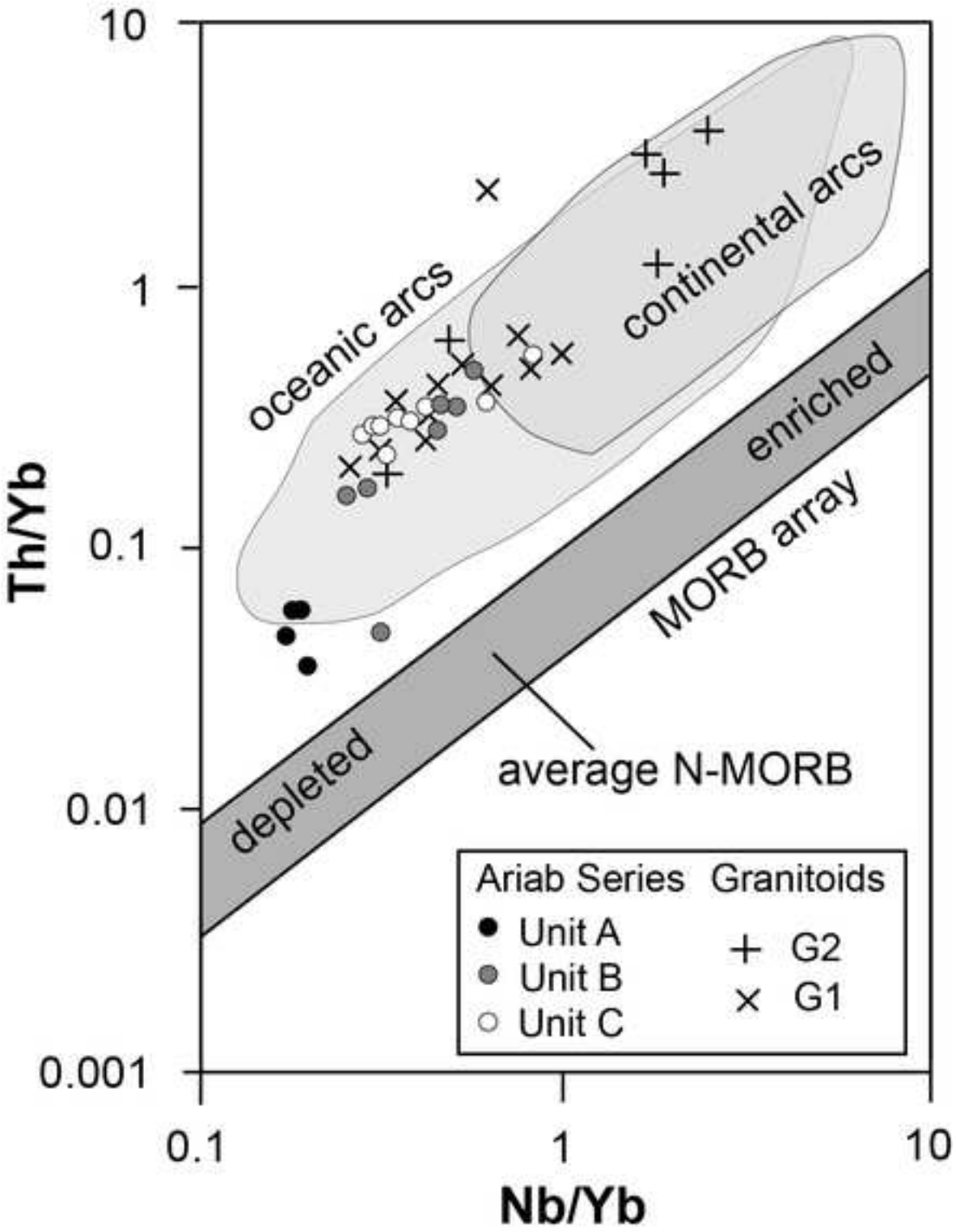

Fig. 11

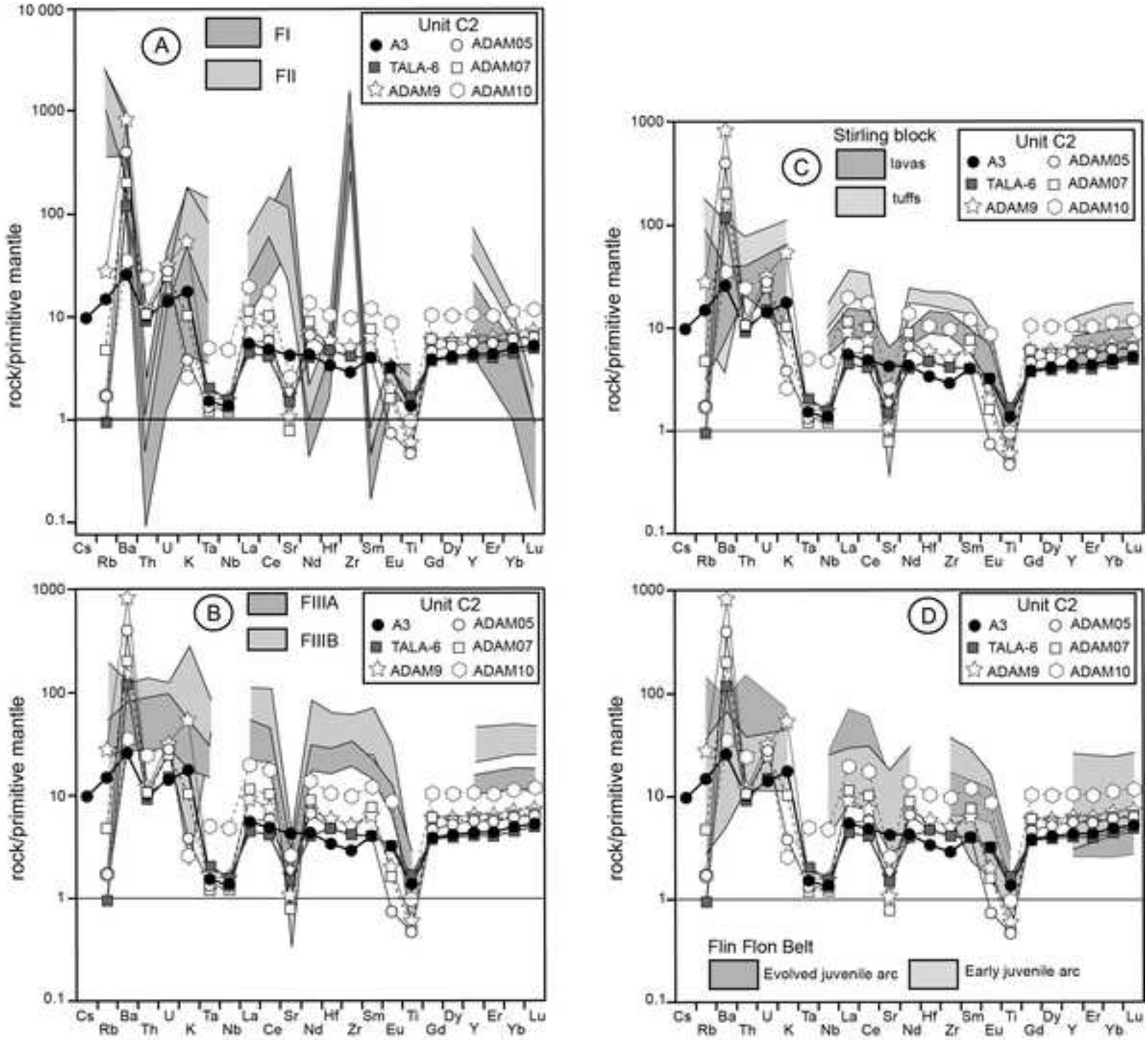

Fig. 12

Click here to access/download;Figure;Fig.12-Soudan-map-VMS.tif

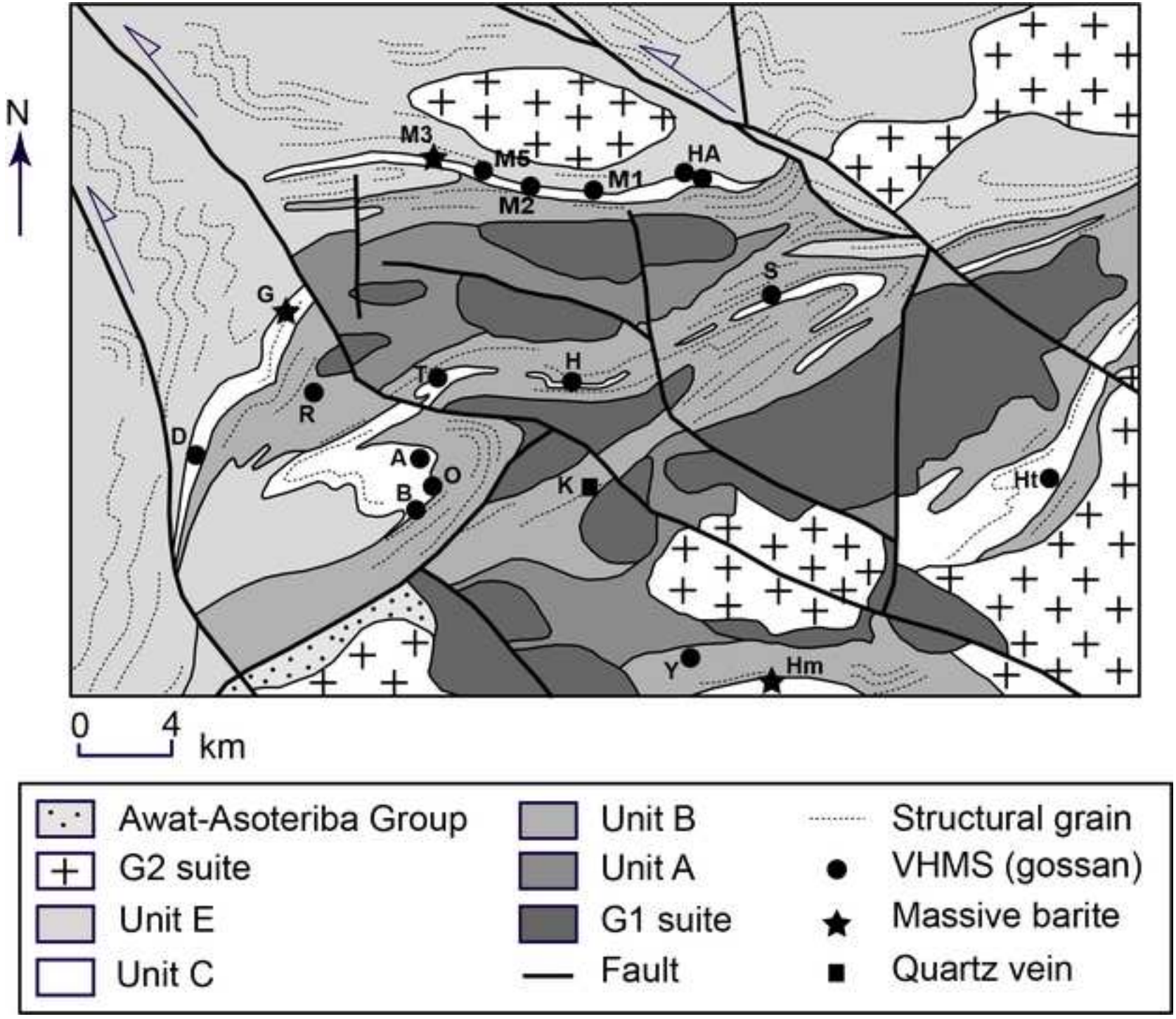

Fig. 13

Click here to access/download;Figure;Fig.13-Soudan-planche-1.tif

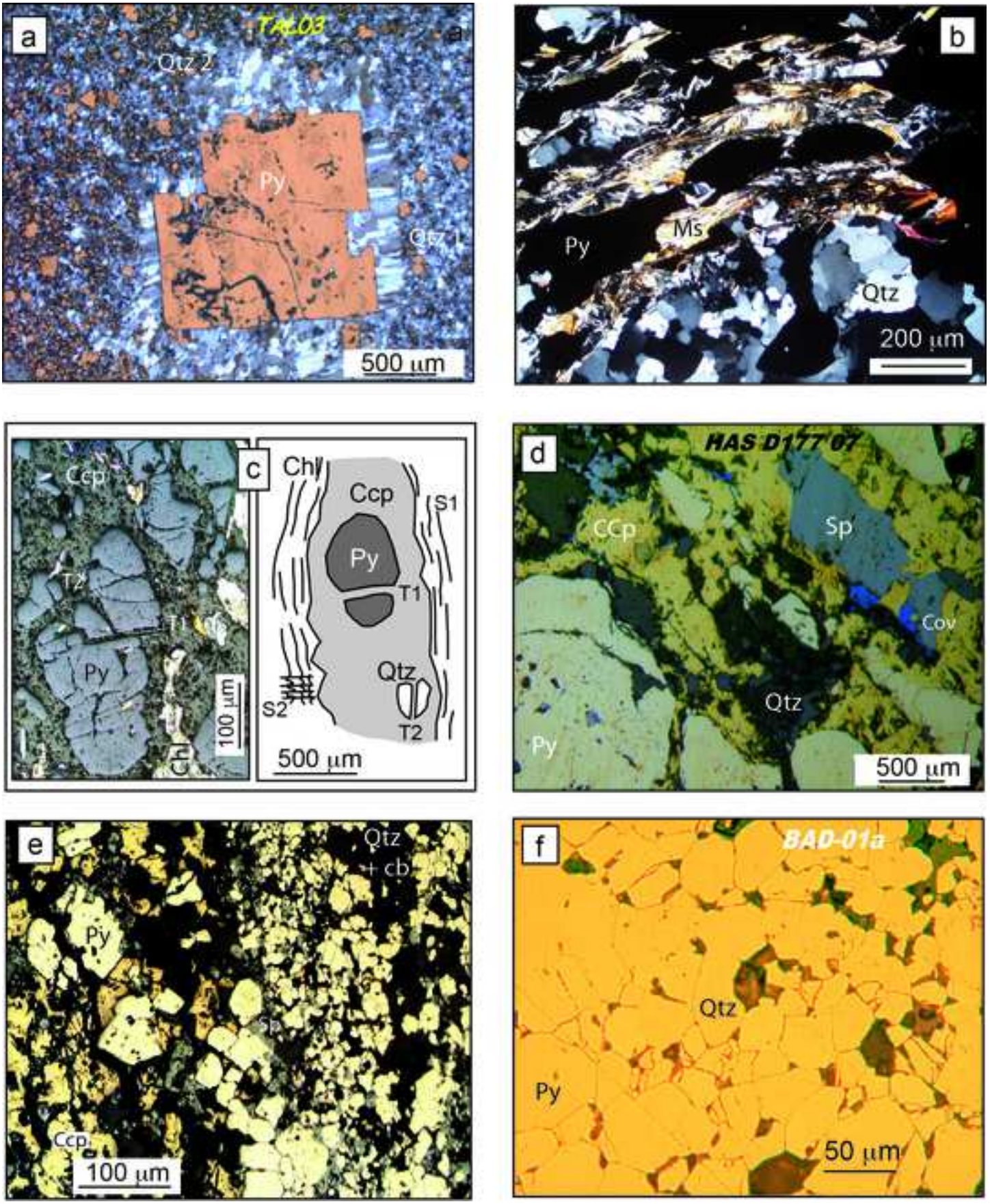

Fig. 14

Click here to access/download;Figure;Fig.14-Soudan-parageneses.tif

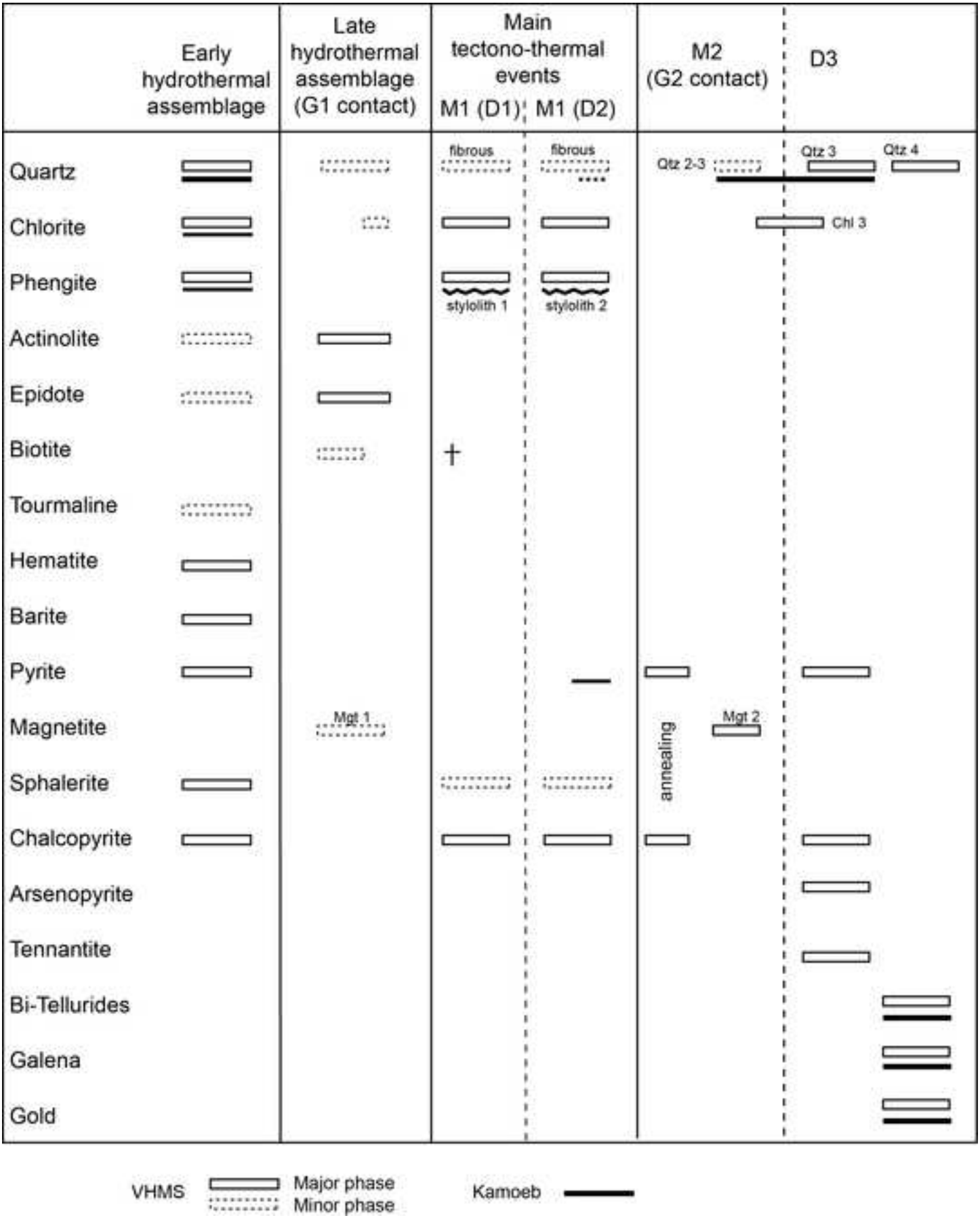

Fig. 15

Click here to access/download;Figure;Fig.15-Soudan-planche-2 - copie.tif

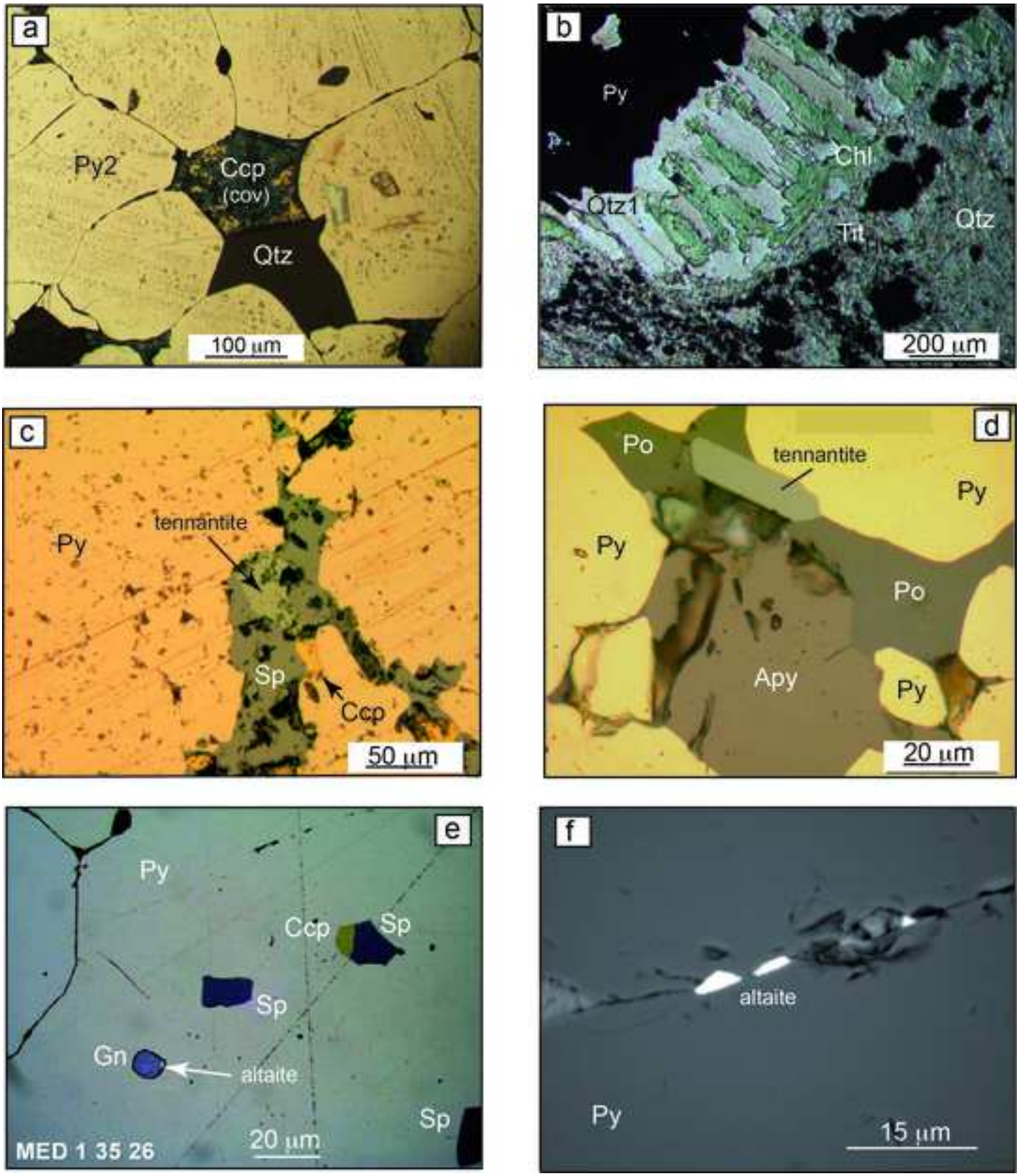

Fig. 16

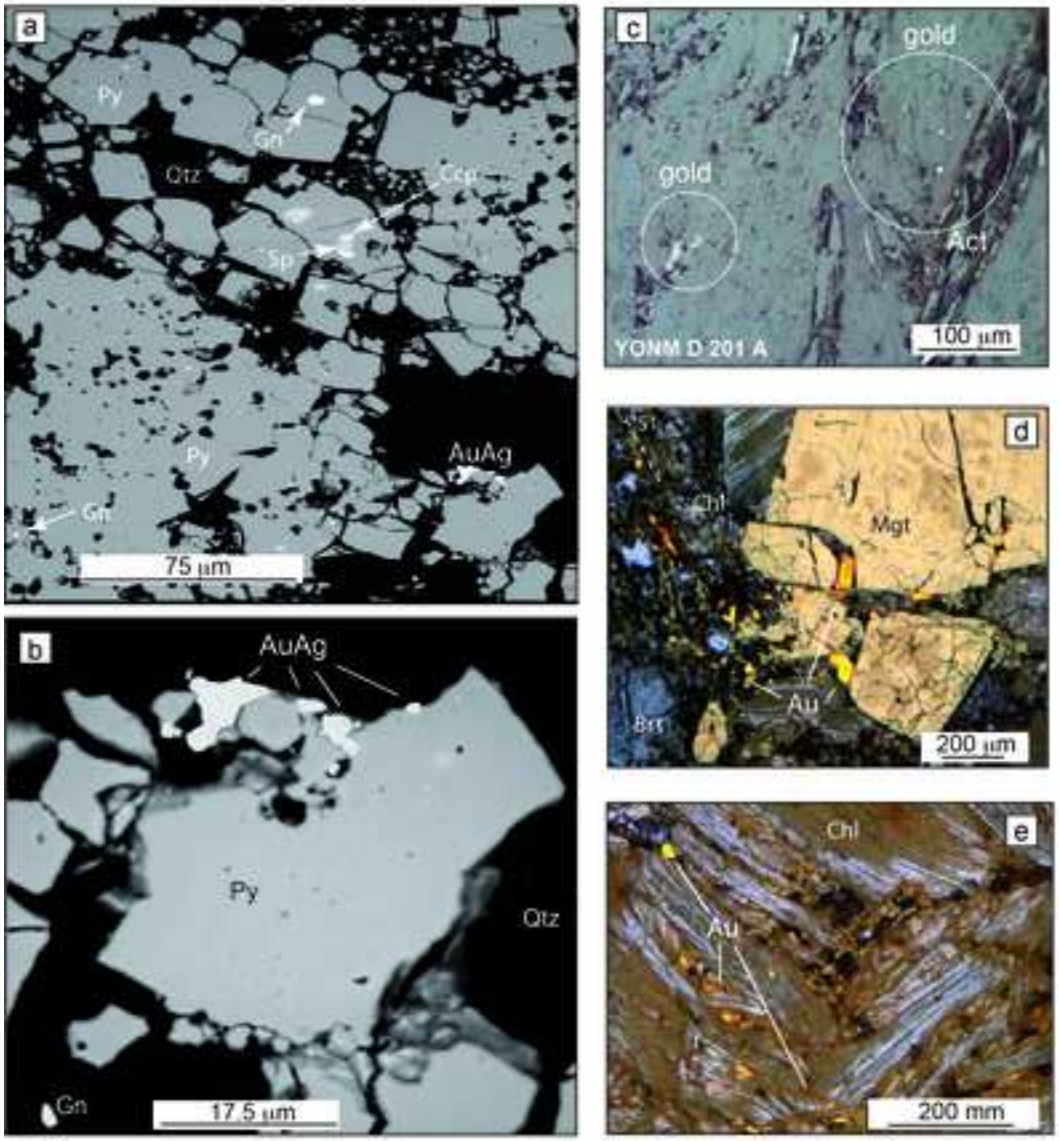

Fig. 17

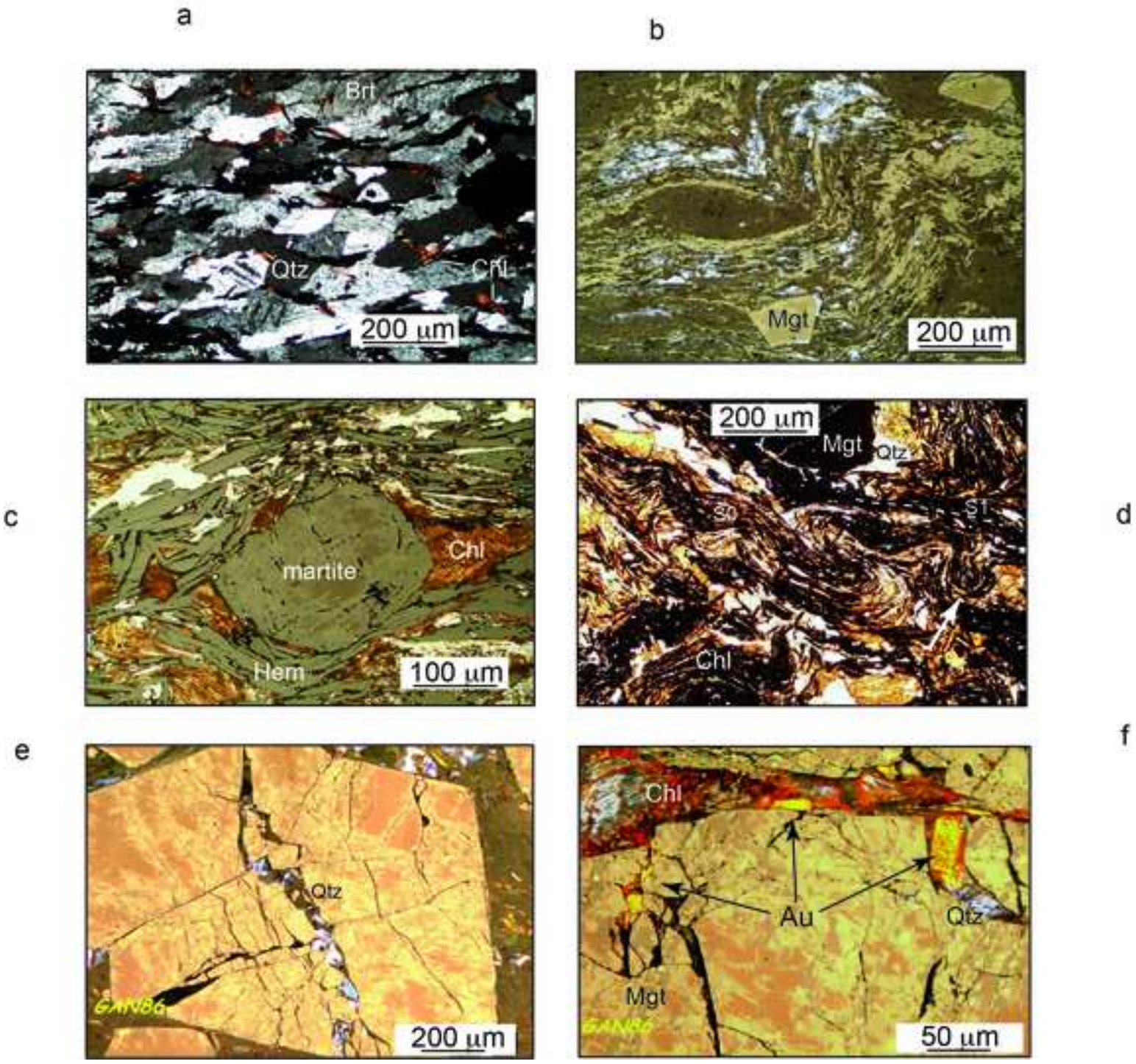

Fig. 18

Click here to access/download;Figure;Fig.18-Soudan-Kamoeb-map.tif

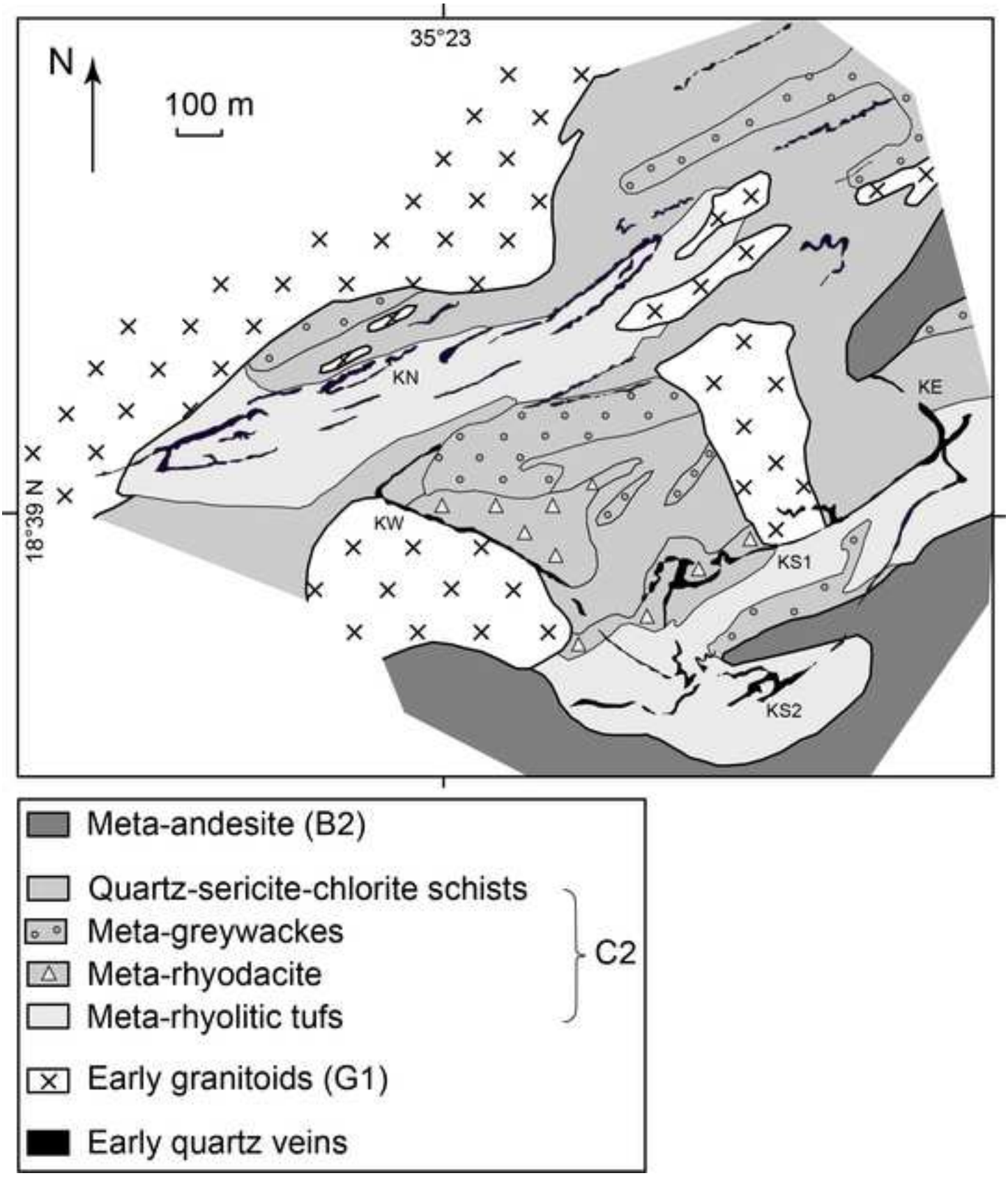

Fig. 19

Click here to access/download;Figure;Fig.19-Soudan-Kamoeb.tif

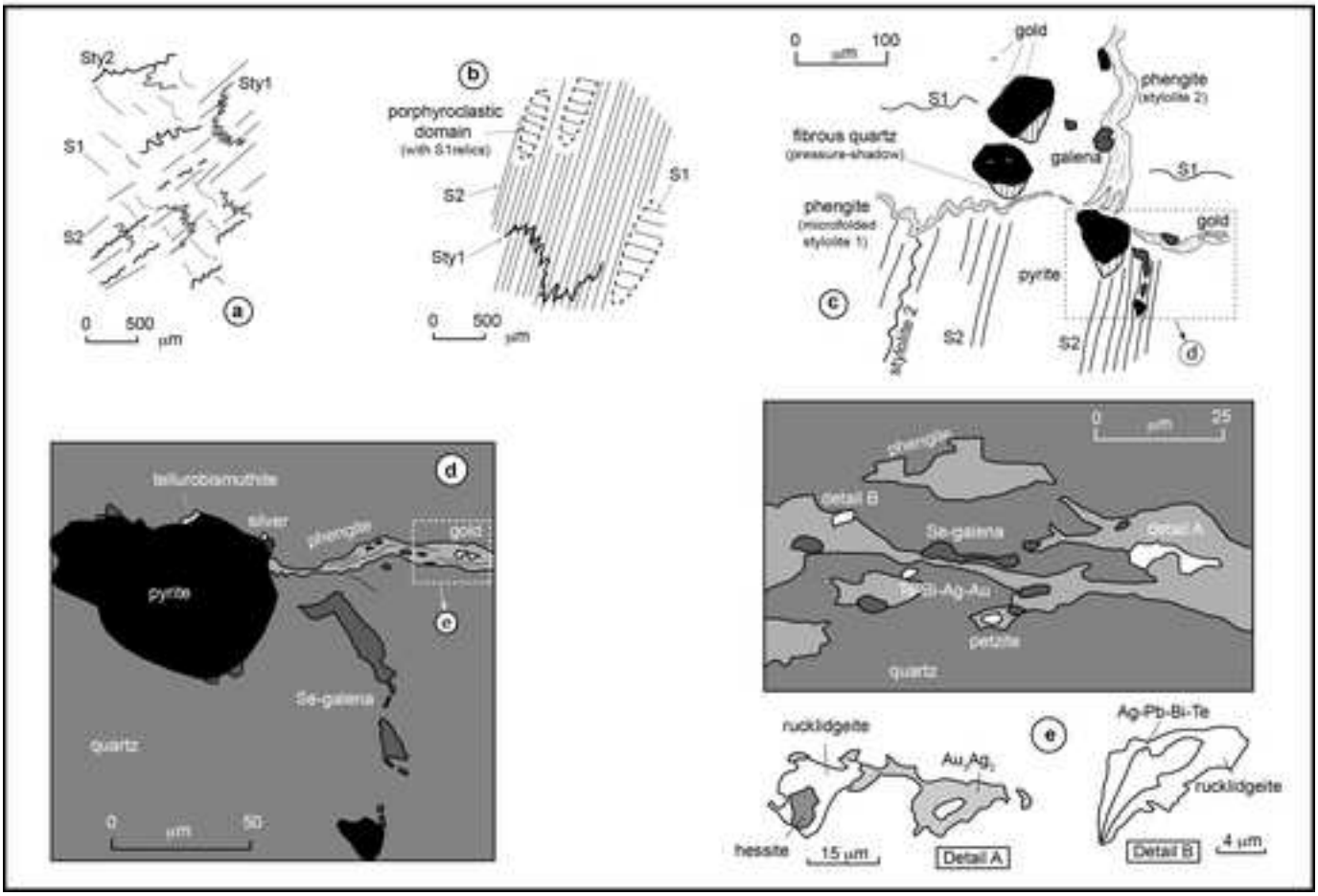

Fig. 20

Click here to access/download;Figure;Fig.20-IF.tiff

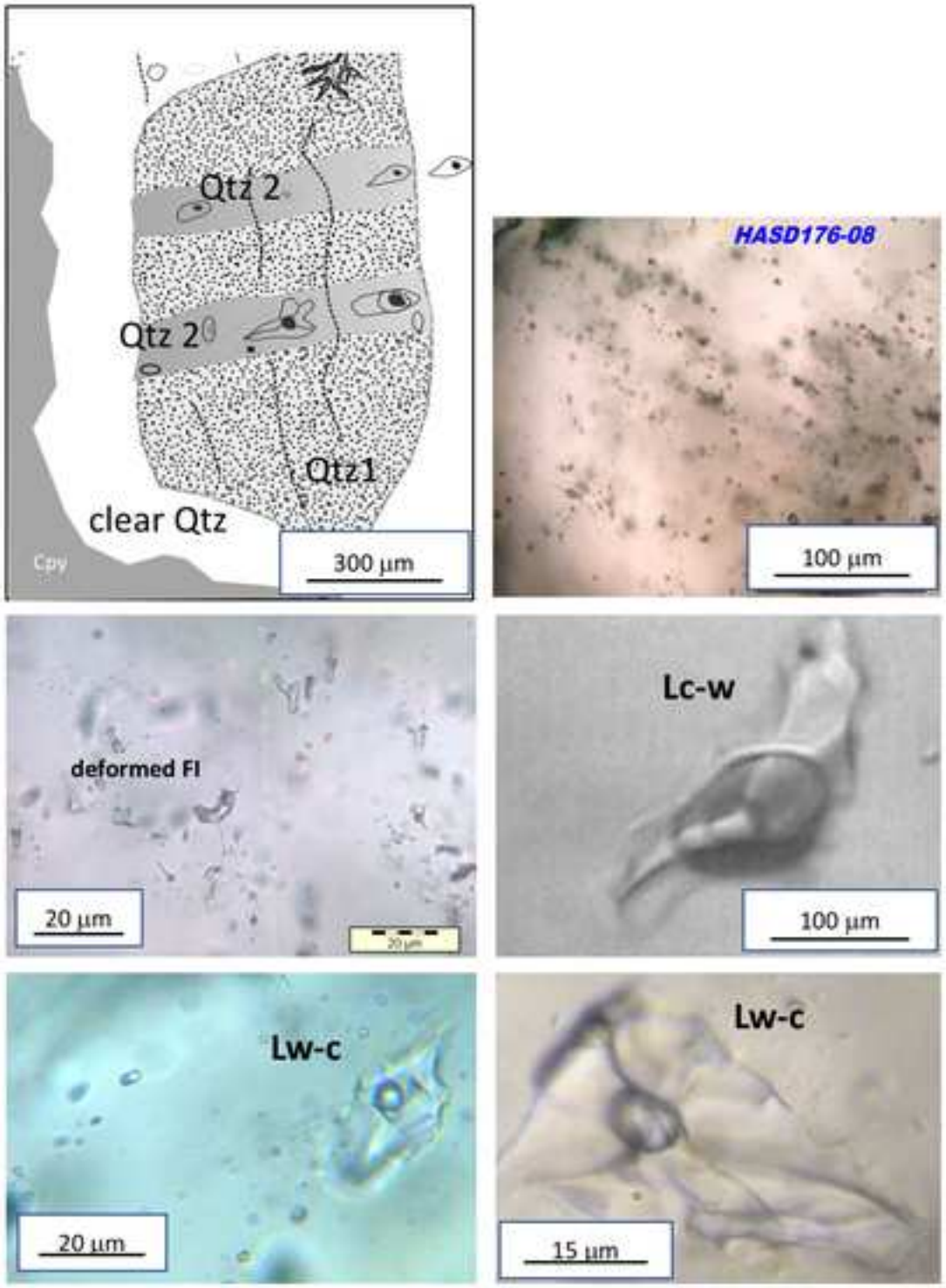

Fig. 21

Click here to access/download;Figure;Fig.21- H2O-Co2-N2.tiff

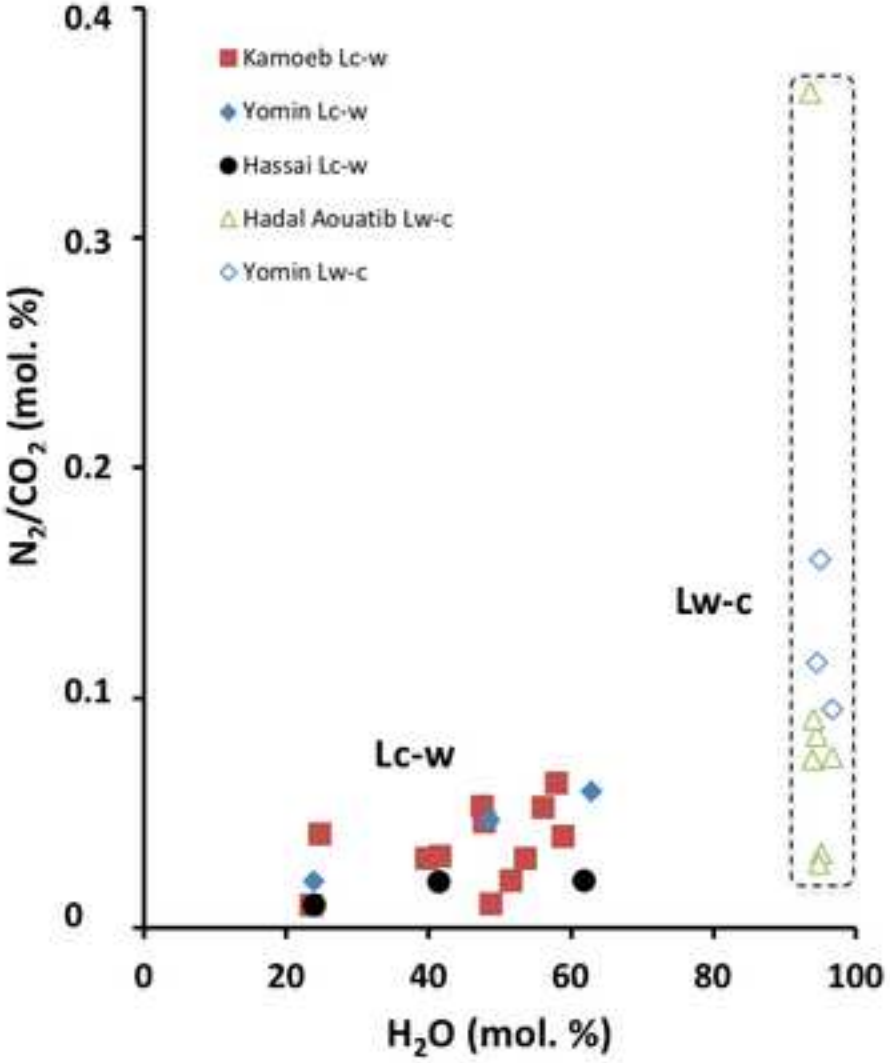

Fig. 22

Click here to access/download;Figure;Fig.22-P-t.tiff

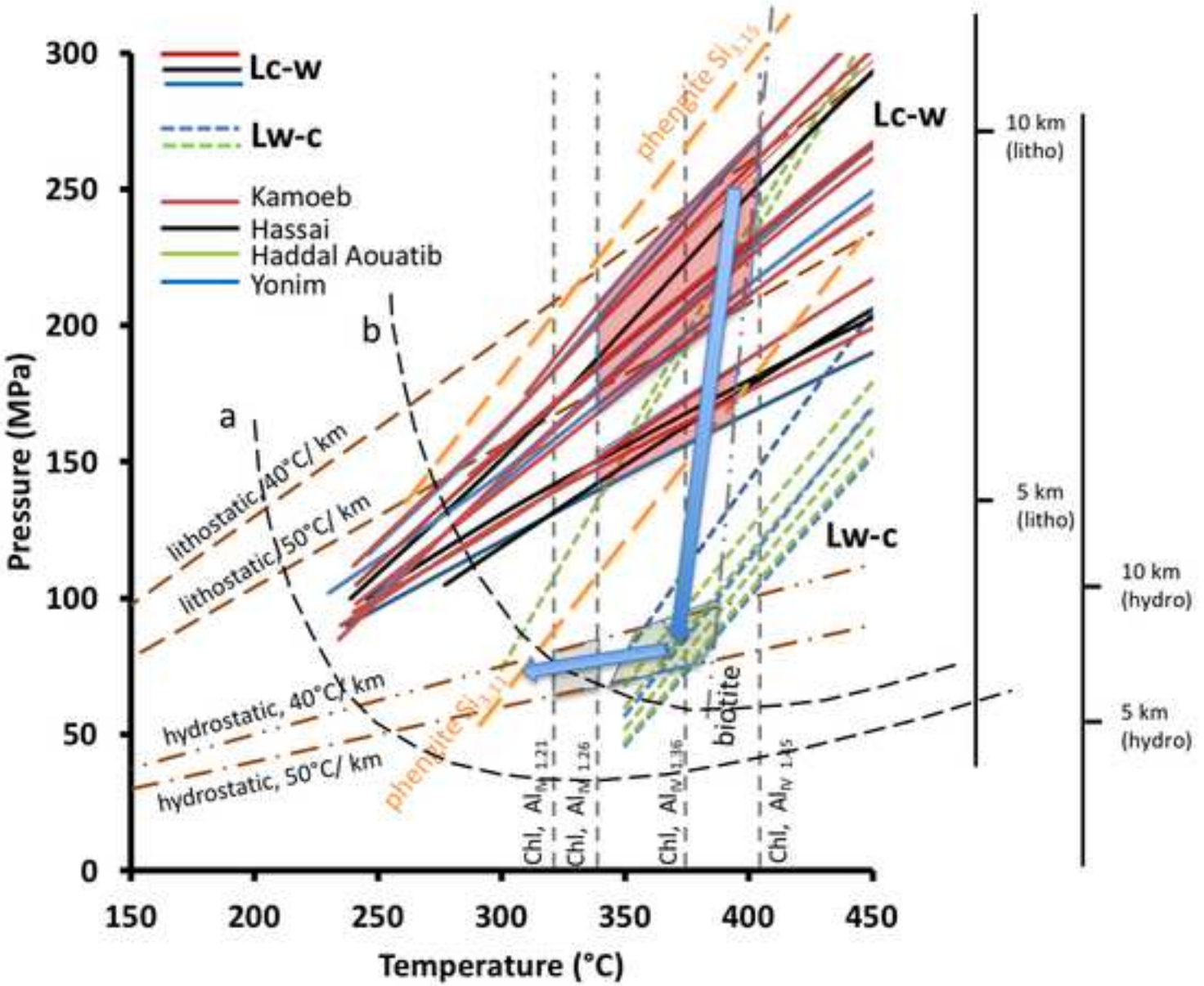

Fig. 23

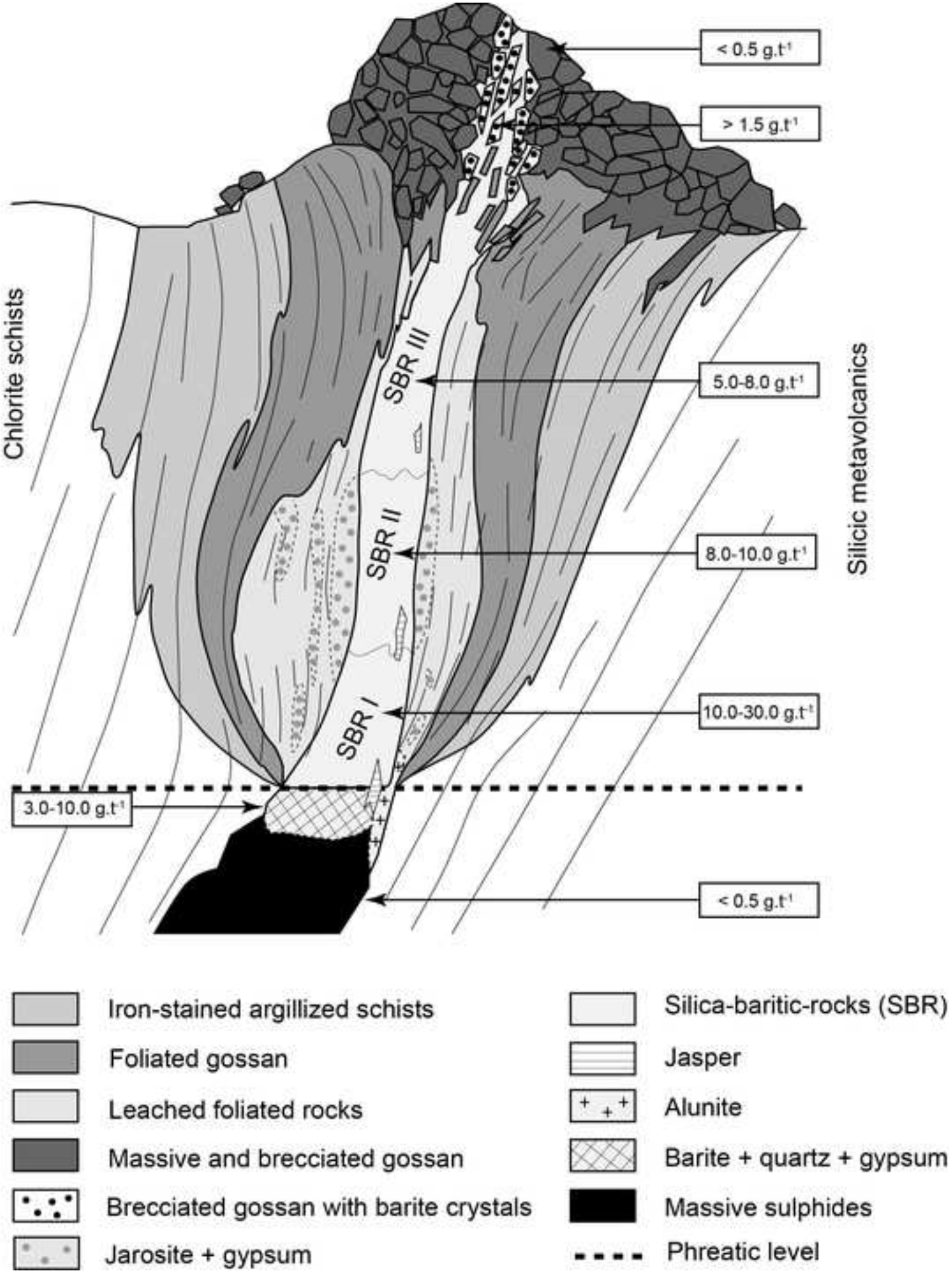

Table 1

Click here to access/download;Table;Tab.1-Soudan-geoch-cor.xls

	Unit A			Unit B1			Unit B2		Unit C1		Unit C2				Unit C3		G1 Suite						G2 Suite			
	NTALGST-173	*List-02*	*TAL04*	KAM-03	DIM4-01	*GANGT-17*	*HAE-CD08*	*ODE-01*	TIDTUAND-11	ADS03	A3	*TAL-A6*	*ADAM01*	*GAN01*	RUK4-02	*ODE-03*	SWKAM137	BAD-25	BIRAJM8	EKITL-2	*UMHASH-7*	*TOMB-01*	HADND77-99	KAMLG-131	*ADAMG-12*	*LGRAN*
SiO_2	51.69	47.87	44.71	54.74	66.51	57.63	56.32	55.58	68.18	77.51	73.14	74.99	75.82	88.18	71.69	65.88	50.82	59.21	71.65	76.46	75.79	72.32	49.57	75.34	59.37	67.37
TiO_2	0.76	0.52	0.33	0.17	0.21	1.39	0.37	0.40	0.34	0.12	0.30	0.36	0.16	0.07	0.20	0.65	0.16	0.48	0.16	0.08	0.12	0.19	0.94	0.16	0.52	0.53
Al_2O_3	13.67	14.84	12.63	14.00	11.48	11.78	15.25	15.47	11.05	9.32	10.80	11.00	10.73	6.98	11.83	12.38	14.11	16.12	13.10	12.02	12.00	11.67	13.47	11.40	16.25	15.65
Fe_2O_3*	11.29	9.72	13.98	11.01	6.29	18.20	9.54	10.78	6.42	4.45	5.10	5.03	3.68	1.43	4.97	9.27	9.65	6.87	4.23	1.88	3.51	3.19	12.52	3.33	6.86	4.29
MnO	0.17	0.11	0.42	0.19	0.10	0.17	0.30	0.17	0.17	0.04	0.11	0.06	0.05	<DL	0.08	0.19	0.18	0.12	0.06	0.04	0.06	0.16	0.20	0.08	0.14	0.09
MgO	7.29	8.79	11.24	6.43	4.19	5.29	2.93	7.39	1.47	0.30	0.86	1.29	3.11	<DL	0.90	2.17	9.45	2.86	1.03	0.57	1.88	1.13	4.24	0.61	3.08	1.39
CaO	9.69	7.56	3.95	8.20	4.78	0.48	5.61	1.43	5.58	0.37	2.33	0.69	<DL	<DL	2.14	1.19	12.30	.88	3.35	0.82	0.75	3.97	7.65	2.74	6.52	3.12
Na_2O	3.60	2.57	<DL	2.69	5.20	<DL	3.60	4.71	0.77	4.37	3.25	5.06	0.31	0.34	4.02	5.54	0.82	3.29	4.13	4.54	3.69	2.76	3.27	3.49	3.10	4.60
K_2O	0.06	<DL	0.16	0.66	<DL	0.18	0.144	<DL	1.34	0.30	0.51	<DL	1.87	1.48	0.70	0.11	<DL	1.03	0.37	2.04	0.51	1.38	0.59	0.81	1.06	1.76
P_2O_5	0.08	0.07	0.05	0.05	0.07	0.31	0.11	0.08	0.13	<DL	0.10	0.09	<DL	<DL	0.06	0.12	0.5	0.12	0.06	0.04	<DL	0.05	0.19	0.07	0.12	0.23
LOI	2.05	8.84	11.21	2.23	1.98	5.36	4.65	4.27	4.92	3.49	3.51	1.53	3.46	1.54	2.36	1.98	3.20	2.45	1.37	1.30	1.69	2.82	7.66	1.50	2.05	0.75
Total	100.35	100.91	98.68	100.37	100.82	100.79	98.83	100.26	100.38	100.29	100.00	100.07	99.19	100.03	99.94	99.47	100.74	99.41	99.52	99.79	99.99	99.63	100.31	99.53	99.43	99.76
Ba	86	101	267	409	130	108	527	105	2539	263	179	850	13,560	1,042	220	98	92	348	234	1,132	269	415	371	396	410	579
Rb	0.7	<DL	2.0	13	<DL	1.6	2.5	<DL	25	5.1	9.3	0.6	21	24	11	1.8	0.5	18	4.3	28	6.4	23	11	18	14	41
Sr	121	68	29	123	130	12	146	43	145	45	87	32	136	44	45	28	84	537	191	43	67	94	151	116	437	348
Cu	25	<DL	155	89	23	30	858	255	37	217	27	29	27	42	272	384	76	70	11	13	5	8	114	125	50	5
Pb	1	2	12	6	7	5	8	3	20	70	9	16	9	339	7	4	5	8	5	8	4	12	7	4	6	7
Zn	62	47	367	98	50	124	1172	408	134	149	87	78	138	21	93	798	99	67	23	29	21	39	129	129	82	66
As	1.9	5.8	4.9	1.5	6.2	1.1	6.4	2.1	2.7	15	2.0	3.7	1.6	37	2.5	<DL	6.8	6.4	1.3	<DL	<DL	1.4	4.2	2.2	1.6	<DL
Cr	273	322	348	254	351	29	79	131	60	100	107	95	75	97	134	12	516	78	91	116	89	62	12	244	78	97
Ni	75	94	48	52	40	14	21	69	6	14	8	9	9	6	7	19	64	18	8	19	7	10	12	14	18	9
Co	40	40	42	46	22	36	41	33	6	6	4	6	5	0.4	8	18	55	18	9	4	5	5	41	137	18	7
V	231	232	229	270	132	197	183	262	14	19	21	21	8	24	43	134	190	169	44	15	17	25	383	16	150	39
Nb	0.43	0.33	0.34	0.46	1.11	2.51	0.42	0.74	0.96	0.95	0.97	1.10	1.22	0.43	1.20	1.01	0.19	1.09	1.71	3.53	2.59	1.73	0.56	1.75	1.09	2.92
Ta	0.10	0.03	0.02	0.03	0.08	0.21	0.03	0.06	0.07	0.07	0.06	0.08	0.08	0.02	0.08	0.08	0.07	0.09	0.12	0.28	0.17	0.14	0.11	0.76	0.09	0.16
Zr	33	22	9	10	42	198	14	30	34	47	32	45	64	5	36	48	8	68	36	129	100	62	24	60	59	188
Hf	1.0	1.9	0.2	0.3	1.3	5.6	0.5	0.9	1.1	1.5	1.0	1.4	2.0	0.2	1.1	1.6	0.2	2.3	1.2	4.7	3.3	1.9	0.8	1.5	2.0	5.0
Th	0.13	0.09	0.16	0.29	0.93	0.37	0.25	0.57	0.76	0.86	0.80	0.73	1.11	0.09	0.96	0.69	0.14	4.07	1.02	3.63	1.94	1.54	0.33	1.65	1.40	4.60
U	0.09	0.04	0.22	0.33	0.31	0.23	0.22	0.16	0.28	0.67	0.29	0.32	0.53	0.27	0.37	0.24	0.07	1.65	0.74	1.20	0.67	0.63	4.01	0.54	0.71	2.65
Y	20	17	6	7	17	73	13	16	21	24	19	18	18	2	18	27	5	15	16	76	52	19	15	25	19	12
La	1.43	0.11	1.62	1.92	4.89	3.57	1.77	3.03	4.07	3.62	3.85	3.21	3.64	0.32	4.34	4.63	0.72	11.8	4.59	14.3	11.2	6.92	2.61	6.81	8.86	25.0
Ce	4.30	2.79	2.91	4.38	10.8	11.0	4.04	6.02	9.05	7.97	8.73	7.50	11.1	0.74	9.38	9.79	1.78	25.2	9.68	32.2	25.6	14.9	6.36	15.0	20.3	51.2
Pr	0.74	0.52	0.39	0.54	1.40	2.27	0.62	0.93	1.28	1.19	1.22	1.11	1.26	0.12	1.28	1.49	0.24	3.22	1.26	4.34	3.60	1.98	0.99	1.95	2.85	6.02
Nd	4.22	3.00	1.87	2.36	6.20	12.9	3.23	4.33	6.04	6.11	5.76	5.53	6.01	0.58	5.85	7.50	1.19	13.6	5.49	20.0	17.1	8.47	5.21	8.72	12.6	22.4
Sm	1.72	1.17	0.59	0.69	1.76	5.24	1.16	1.33	1.92	2.28	1.77	1.78	1.87	0.22	1.78	2.50	0.40	2.92	1.58	6.24	5.26	2.30	1.68	2.53	3.01	4.08
Eu	0.72	1.79	0.27	0.24	0.46	1.04	0.45	0.48	0.69	0.63	0.53	0.53	0.22	0.05	0.51	0.83	0.16	0.78	0.47	0.35	1.35	0.62	0.56	0.56	0.81	1.10
Gd	2.62	14.0	0.81	0.84	2.09	7.89	1.60	1.75	2.48	3.12	2.26	2.30	2.22	0.25	2.17	3.37	0.55	2.58	1.92	8.18	6.53	2.56	2.28	3.21	2.96	3.17
Tb	0.49	0.37	0.14	0.16	0.37	1.58	0.28	0.32	0.45	0.59	0.41	0.42	0.41	0.04	0.39	0.60	0.10	0.41	0.34	1.56	1.17	0.44	0.38	0.58	0.49	0.43
Dy	3.36	209	0.95	1.12	2.54	11.0	1.96	2.23	3.22	4.03	2.88	2.85	2.95	0.33	2.78	4.15	0.73	2.51	2.43	11.1	7.94	2.99	2.54	3.91	3.07	2.35
Ho	0.73	0.72	0.21	0.26	0.57	2.45	0.43	0.50	0.72	0.86	0.65	0.63	0.68	0.08	0.62	0.92	0.16	0.53	0.54	2.51	1.76	0.65	0.55	0.88	0.65	0.43
Er	2.20	2.64	0.63	0.82	1.73	7.48	1.31	1.49	2.23	2.56	2.02	1.92	2.19	0.25	1.93	2.78	0.51	1.56	1.71	8.02	5.37	2.01	1.60	2.76	1.94	1.16
Tm	0.34	0.28	0.10	0.13	0.28	1.14	0.20	0.23	0.36	0.39	0.33	0.30	0.37	0.04	0.31	0.44	0.08	0.24	0.28	1.34	0.84	0.32	0.25	0.45	0.31	0.17
Yb	2.27	1.87	0.68	1.00	1.94	7.74	1.43	1.58	2.49	2.66	2.31	2.15	2.87	0.35	2.19	3.04	0.58	1.69	2.04	9.76	5.88	2.26	1.67	3.21	2.19	1.13
Lu	0.36	1.08	0.11	0.17	0.32	1.23	0.23	0.26	0.41	0.40	0.39	0.36	0.49	0.06	0.36	0.48	0.10	0.28	0.35	1.61	0.97	0.38	0.27	0.52	0.36	0.19
SREE	40.21	239.34	11.28	14.63	35.35	76.83	18.71	24.48	35.41	36.41	33.11	30.59	36.28	3.43	33.89	42.52	7.30	67.32	32.68	121.51	94.57	46.80	26.95	51.09	60.40	118.83

Table 2

FI type	Tm CO_2 (°C)	Tm ice (°C)
Lc-w		
Kamoeb (n=66)	-58.3 to -56.8	-5.6 to -2.2
VHMS (n=118)	-59.7 to -57.2	-7.6 to -2.5
Lw-c		
VHMS (n=10)		-7.1 to -2.2

Tm clat (°C)	Th $CO_{2\,(}$°C) (L)	Th (°C)
2.6 to 7.9 1.8 to 8.3	16.3 to 26.0 22.8 to 29.7	220 to 310 237 to 278
1.9 to 8.0		260 to 355

Table 3

	Microthermometry (°C)		
	Tm CO_2	Tm ice	Tm clat
Lc-w			
Kamoeb			
KAME02-11	-57.1	-4.2	7.6
KAME02-12	-57.3	-4.3	3.3
KAME02-13	-57.0	-5.3	2.6
KAME02-14	-58.1	-2.2	4.8
KAME02-16	-57.1	-3.4	7.1
KAME02-18	-57.0	-3.0	7.1
KAME02-110	-57.2	-4.1	6.3
KAME02-111	-57.0	-5.1	7.2
KAME02-114	-57.8	-4.2	4.5
KAME02-23	-57.2	-5.6	7.5
KAME02-25	-57.0	-4.4	5.5
KAME02-26	-56.8	-3.1	7.9
Yonim			
YONM-202-N81	-56.9	-2.5	4.3
YONM-202-N82	-57.2	-4.7	6.4
YONM-202-N83	-57.2	-5.5	5.8
YONM-202-N84	-58.3		4.4
Hassai			
HASD176-081	-57.3	-3.6	4.2
HASD176-084	-56.8		7.7
HASD176-088	-57.3	-2.7	7.6
Lw-c			
Hadal Ouatib			
HDND77-111		-5.1	4.2
HDND77-112		-5.0	8.0
HDND77-113		-5.6	7.6
HDND77-114		-5.1	6.5
HDND77-117		-2.3	4.3
HDND77-118		-7.1	6.3
HDND77-119		-2.2	6.6
Yonim			

YONM 202-N2-1	-56.8	-7.1	
YONM 202-N2-2	-56.6	-3.6	1.9
YONM 202-N2-3	-56.6		1.7

		Raman data (mol.%)			Bulk composit	
Th CO_2 (L)	Th	fvp (%)	ZCO_2	ZN_2	XH_2O	XCO_2
23.2	241.5	75	97.0	3.0	48.8	49.3
20.1	248.3	65	95.0	5.0	56.2	38.5
23.6	234.1	70	98.0	2.0	51.7	44.3
21.8	190*	80	97.0	3.0	39.7	56.8
26.0	240.3	80	98.0	2.0	41.7	54.8
23.6	235.7	90	96.0	4.0	24.7	71.6
22.6	220.5	90	99.0	1.0	23.5	74.9
20.6	241.3	75	95.5	4.5	47.9	48.3
22.2	240.4	65	94.0	6.0	58.0	36.7
19.8	310.1	65	96.0	4.0	58.9	37.8
22.2	287.6	75	95.0	5.0	47.6	47.8
22.1	281.9	70	97.0	3.0	53.6	43.7
25.4	237.1	90	98.0	2.0	23.9	73.5
25.4	230.3	70	96.5	3.5	48.5	47.3
25.4	243.2	75	95.5	4.5	48.5	47.3
23.6	246.2	60	94.0	6.0	62.8	32.0
23.3	239.5	60	98.0	2.0	62.0	34.3
22.8	245.3	90	99.0	1.0	24.0	74.7
29.7	277.7	80	98.0	2.0	41.5	55.4
	285*	30	89.0	11.0	95.2	3.1
	341.9	20	89.5	10.5	94.9	3.6
	260.5	30	86.0	14.0	94.0	4.1
	354.7	30	83.0	17.0	94.6	3.6
	275.7	30	84.5	15.5	96.7	2.7
	278.3	20	80.0	20.0	94.1	3.3
	345.9	20	50.0	50.0	93.7	3.3

250 *	30	65.0	35.0	95.1	2.5
240 *	35	71.5	28.5	94.6	2.6
220*	25	70.5	29.5	96.7	2.1

tion (mol. %)	
X_{N2}	X_{NaCl}
0.5	1.4
2.0	3.3
0.9	3.1
1.7	1.8
1.7	1.8
2.9	0.8
0.7	0.9
2.2	1.6
2.3	3.0
1.5	1.8
2.5	2.1
1.3	1.4
1.5	1.1
2.2	2.0
2.2	2.0
1.9	3.3
0.7	3.0
0.7	0.6
1.1	2.0
0.1	1.6
0.1	1.4
0.3	1.6
0.3	1.5
0.2	0.4
0.3	2.3
1.2	1.8

0.4	2.0
0.3	2.5
0.2	1.0